Kinematic- and Synchrotron-Aging Studies for Young Extragalactic Radio Sources

Hiroshi NAGAI

DOCTOR OF
PHILOSOPHY

Department of Astronomical Science,
School of Physical Science,
The Graduate University for Advanced Studies

2006

Abstract

Compact Symmetric Objects (CSOs) are proved to be young radio sources from both the kinematic- and synchrotron-aging studies.

With Very Long Baseline Array (VLBA) observations for CTD 93 over 8.5 yr, we detected an increase of separation between the hot spot and the counter hot spot. The separation rate along the source axis is $0.34\pm0.11c$, which results in a kinematic age of 2200 ± 700 yr. Assuming that two hot spots are moving apart from the core at equal speeds, we derive an advance velocity of $0.17\pm0.06c$. On the other hand, our multi-frequency observations revealed that radio-lobe spectra show a high-frequency steepening due to synchrotron aging. The spectral break decreases with distance from the hot spot. This tendency is expected from the basic scenario of radio lobe evolution involving particle acceleration at the hot spots, with the radio lobe populated by high-energy electrons that have leaked out from the hot spots. From the spectral fit in the radio lobe of CTD 93 under the minimum-energy assumption, we derive the advance velocity of $0.232\pm0.005c$ and synchrotron age of 1720 ± 40 yr. The kinematic age and synchrotron age show an agreement within a factor of two.

Following the detection of hot-spot motion and spectral break in CTD 93, we examined both kinematic and synchrotron ages of the innermost radio source of 3C 84 using VLBA. Since 3C 84 is one of the nearest powerful CSOs, detailed kinematics and spatial distribution of break frequency are revealed. Measurements of hot spot motion with respect to the core over 4.5 yr resulted in the advance velocity of $0.43\pm0.06c$. The resultant kinematic age is 33 ± 5 yr in 2000. The radio-lobe spectra also show a high-frequency steepening due to synchrotron aging. The break frequency decreases with the distance from the hot spot. The lowest break frequency of 2.3 ± 1.4 GHz is occurred near the core. Assuming the minimum-energy field, we derive the synchrotron age of 24^{+14}_{-5} yr in 1995. The kinematic and synchrotron ages are thus in very good agreement. Also these ages indicate that innermost radio lobe is associated with the 1959 outburst of activity.

We proved that CTD 93 and 3C 84 are young radio sources from both kinematic- and synchrotron-aging studies. This is strong evidence for the hypothesis that CSOs are young radio sources. As well, the agreements between kinematic and synchrotron ages imply a validity of synchrotron-aging analysis under the minimum-energy assumption in CSOs. Assuming that minimum-energy assumption is also applicable to FRII sources, we found that an averaged expansion velocity of FRII sources is $\sim 0.05c$. This is comparable to an averaged CSOs' expansion velocity of $\sim 0.1c$. This implies that expansion velocity of radio lobe does not strongly depend on the linear size of radio source, if we allow that CSOs evolve into FRII sources.

Finally, we examined the physical property of hot spots for a large number of radio galaxies to reveal the relation among CSOs, MSOs, and FRII sources. The hot spot luminosity of CSOs and MSOs are almost equivalent to that of FRII sources, indicating that the jet power of CSOs and MSOs is favorably comparable to that of FRII sources. The hot spot pressure and radius show simple power-law changes as expected from the dynamical evolution model of the hot spot. This is a supporting evidence for evolutional sequence from CSOs to MSOs to FRII sources.

Overall results strongly argue that CSOs are young extragalactic radio sources that are potentially able to evolve into FRII sources through MSOs.

Contents

Chapter 1

Introduction

1.1 Background of Active Galactic Nuclei

Active Galactic Nuclei (AGNs) are one of the most powerful astronomical objects in the universe. They produce a huge amount of energy at the center of galaxies. The emission from AGNs shows broad continuum spectra from radio to γ-ray. Their luminosity ranges from 10^{33} to 10^{41} W, which corresponds to the amount of radiation of up to a thousand of galaxies. The luminosity of AGNs shows significant time variations. Typical time scale of the variation is from days to years, indicating that the emission region of AGNs is quite small. The powering source of AGNs is now considered the gravitational potential of the super massive black hole (SMBH). Some observations show the evidences of the presence of SMBH at the center of galaxies, and they are estimated to have $10^6 - 10^9$ solar mass (e.g., Ford et al. 1994; Harms et al. 1994; Miyoshi et al. 1995; Tanaka et al. 1995; Ghez et al. 2003).

AGNs show various observational properties, and they are classified into a number of categories according to their luminosities, radio loudness, spectral properties, polarization characteristics, variability, and so on. They are usually organized according to their optical spectra, luminosities, and radio loudness (the ratio of radio flux at 5 GHz ($F_{5\mathrm{GHz}}$) to B-band optical flux (F_{B})). The optical spectral properties are generally focused on whether AGN have broad emission lines (Type 1), only narrow emission lines (Type 2), or weak or unusual emission lines (e.g., LINER, Narrow Line Seyfert 1). The absence of broad line emission is basically considered that the region of broad-line- emitting gas, which is called broad line region (BLR), is obscured along the line of sight by a torus of gas and dust outside the accretion disk (Holt et al. 1992; Urry & Padovani 1995). The luminosity is expected to be attributed by the accretion rate of the gas on to the SMBH. This idea is originally modeled by Lynden-Bell (1969), and has been developed by many astronomers (e.g., Shakura & Sunyaev 1973). Contrary to above two things, the origin of radio loudness is an unresolved problem. Although the optical and ultraviolet emission-line spectra and the infrared to soft X-ray continuum of most radio-loud and radio-quiet AGN[1] are quite similar, the ratio of radio luminosity and 1 μm luminosity has a range of 10^5. Some astronomers proposed that the radio loudness may be related to the type of host galaxy (Smith et al. 1986) or to black hole spin (Blandford 1990; Wilson & Colbert 1995). Also the alignment of the relativistic jet with the line of sight can affect the radio loudness due to the Doppler-beaming of radio photons. However, there are so far no striking observational evidences to prove the origin. Therefore the study of radio source property of AGNs is important to understand the origin of radio loudness.

Most of radio-loud AGNs have two-sided radio jets and radio lobes, often called Radio Galaxies[2]. Radio galaxies are divided into two different morphological types: Fanaroff-Riley type I (FRII) radio

[1]Radio-loud AGNs mean that they have ratios $F_{5\mathrm{GHz}}/F_{\mathrm{B}}>10$, others are radio-quiet.

[2]To be precise, Radio Galaxies include two major sub-classes: Narrow-Line Radio Galaxies (NLRG) and Broad-Line Radio Galaxies (BLRG). BLRG often have one-sided jet. They tend to be included in the category of QSO. So hereafter I refer NLRG as radio galaxies in this thesis

galaxies, which have two symmetric radio jets and their intensities decrease with the distance from the core, and Fnaroff-Riley type II (FRII) radio galaxies, which have more highly-collimated jet than that of FRI. Radio jets are the outflow of relativistic particles, and propagate up to Mpc scale (e.g., Hercules A, Fornax A). Especially in case of FRII radio galaxies, this flow forms prominent hot spots at the tip of jets. Hot spots are interpreted as shocks that jets are colliding with ambient medium, converting much of their bulk kinetic energy into relativistic electrons and magnetic fields (Blandford & Rees 1974; Scheuer 1974).

1.2 Formation of FRII Radio Galaxies and Synchrotron Aging Theory

Formation and evolution of radio galaxies are fundamental problems in studying AGNs. While there is no widely-accepted scenario for the evolution of FRI sources, it is commonly believed that the basic evolutional model for FRII sources is as follows (e.g., Blandford & Rees 1974; Scheuer 1974) (Figure 1.1):

1. A pair of beamed jets is emanating from the central core.
2. A beamed jet accelerated super-sonically will forms the forward and reverse shock.
3. Forward shock in the ambient medium will partially randomize the incoming (in the shock frame) bulk energy of the ambient medium.
4. Hot spots, which are identified as the region where the beamed jets are interacting with reverse shock, accelerate relativistic electrons and emit synchrotron radiation.
5. The extended radio lobes are populated by relativistic electrons which are leaked out from the hot spots.
6. The jets drill through the ambient medium, and then the radio lobes evolve self-similarly.

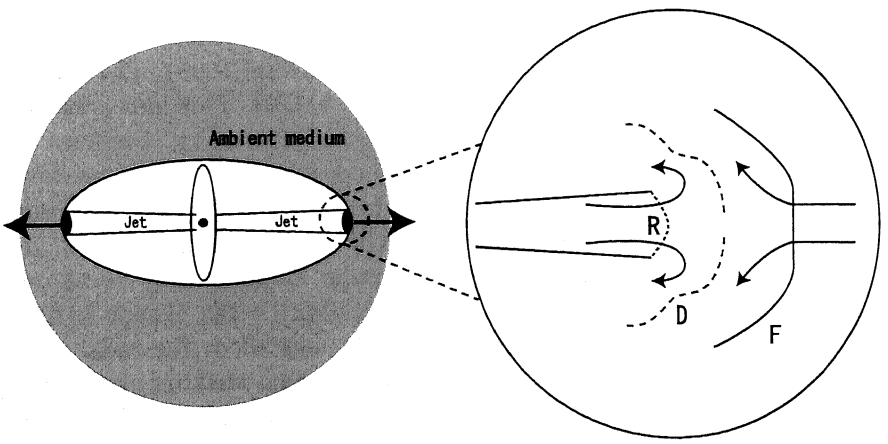

Figure 1.1: Schematic image of basic model of radio lobe formation. The bulk energy of beamed jet is strongly randomized at the reverse shock (R) and it meets the ambient medium, which has passed through forward shock (F) at the contanct discontinuity (D).

One of the methods to test such evolutional scenario is to estimate distribution of spectral break due to electron energy loss by synchrotron radiation. This phenomenon is called radiative aging or synchrotron aging.

The basic theory of the synchrotron aging process in radio sources was developed by Kardashev (1962) and Pacholczyk (1970), often referred to as the KP model, and by Jaffe & Perola (1973), called the JP model. The KP and JP models assume a single impulsive injection to produce the power-law distribution of relativistic electrons. The KP model assumes that all electrons maintain the same pitch angle[3] during their radiative lifetimes. On the other hand, the JP model allows the pitch angle scattering, and the scattering time scale is assumed much shorter than the radiative lifetime.

The relativistic electrons which are accelerated at the hot spots presumably suffered some further acceleration process of stochastic character. Such processes are under the on-going discussions, but simplest process is Fermi mechanism (Fermi 1949; Fermi 1954; Morrison 1954; Wentzel 1963; Wenzel 1964), which forms a power-law distribution, $N(E) = N_0 E^{-\gamma}$ ($\gamma = 2\alpha + 1$ where α is the emission spectrum index, defined in the sense $S \propto \nu^{\alpha}$), where N_0 is the electron density at $t = 0$. For the simplicity, we assume that the distribution of electrons is only affected by synchrotron radiation losses. The energy loss rate due to synchrotron radiation is given by

$$\frac{dE}{dt} = -c_2 B^2 \sin^2\theta E^2, \tag{1.1}$$

where B is the magnetic field strength, and θ is the pitch angle between the electron and magnetic field. The quantity $c_2 = 2e^4/3m^4c^7$ is a constant defined by Pacholczyk (1970), where e is the electron charge, m is the electron mass, and c is the light velocity. Since the energy loss rate is proportional to E^2, higher energy electrons lose their energy faster than lower ones. The distribution of electrons at some later time t is given by

$$N(E,\theta,t) = N_0 E^{-\gamma}(1 - c_2 B^2 \sin^2\theta E t)^{\gamma-2}. \tag{1.2}$$

In the KP model, it is assumed that the pitch angle distribution of electrons is isotropic, and the electron density and magnetic field are homogeneous along the source depth s. Then the radiation spectrum in an optically thin medium is given by

$$\begin{aligned} S_\nu(t) &= s\int_{4\pi} c_3 B\sin\theta \int_0^{\infty} F(x)N(E,\theta,t)dEd\Omega \\ &= s\int_{4\pi} c_3 B\sin\theta \int_0^{E_H} F(x)N_0E^{-\gamma}(1 - c_2B^2\sin^2\theta Et)^{\gamma-2}dEd\Omega, \end{aligned} \tag{1.3}$$

where s is the source thickness, $F(x) = x\int_x^{\infty} K_{5/3}(z)dz$, and x is the frequency normalized by the critical frequency ν_c (Pacholczyk 1970). Because the higher energy electrons deplete their energy faster (see equation (1)), a cutoff energy appears in the spectrum. There are no electrons above the cutoff energy of $E_H = 1/c_2B^2\sin^2\theta t$. Thus above equation is replaced by the following equation,

$$\begin{aligned} S_\nu(t) &= 2\pi s c_3 c_1^{\frac{\gamma-1}{2}} N_0 H^{\frac{\gamma+1}{2}} \nu^{\frac{1-\gamma}{2}} \int_0^{\frac{\pi}{2}} d\theta \int_{\frac{\nu}{\nu_b}\sin^3\theta}^{\infty} \sin^{\frac{3\gamma+1}{2}}\theta F(x) x^{-\frac{1}{2}} \left(x^{\frac{1}{2}} - \left(\frac{\nu}{\nu_b}\sin^3\theta\right)^{1/2}\right)^{\gamma-2} dx \\ &= S_0 \nu^{\frac{1-\gamma}{2}} \int_0^{\frac{\pi}{2}} d\theta \int_{\frac{\nu}{\nu_b}\sin^3\theta}^{\infty} \sin^{\frac{3\gamma+1}{2}}\theta F(x) x^{-\frac{1}{2}} \left(x^{\frac{1}{2}} - \left(\frac{\nu}{\nu_b}\sin^3\theta\right)^{1/2}\right)^{\gamma-2} dx, \end{aligned} \tag{1.4}$$

where S_0 is a constant factor, $\nu_b = c_1/c_2^2B^3t^2$, $F(x) = x\int_x^{\infty} K_{5/3}(z)dz$, and x is the frequency normalized by the critical frequency (Pacholczyk 1970). The parameters $c_1 = 3e/4\pi m^3c^5$ and $c_3 =$

[3]the angle between the direction of the electron velocity and that of the magnetic field

$\sqrt{3}e^3/4\pi mc^2$ are constant factors defined by Pacholczyk (1970). A quantity ν_b corresponds to a critical frequency of electrons that have an energy of E_H, and is often called break frequency. The resultant spectrum is steeper above the break frequency ν_b than the initial injection spectrum (see dotted line in Figure 1.2). The break frequency can be expressed in a more convenient way as

$$\frac{\nu_b}{[\mathrm{GHz}]} = 1.12 \times 10^9 \left(\frac{B}{[\mathrm{mG}]}\right)^{-3} \left(\frac{t}{[\mathrm{yr}]}\right)^{-2}. \tag{1.5}$$

In case of the JP model, the terms of $c_2 B^2 \sin^2\theta$ should be replaced by $c_2 B^2 < \sin^2\theta >$, where $<>$ represents the ensemble average. Thus the radiation spectrum is given by

$$S_\nu = S_0 \nu^{\frac{1-\gamma}{2}} \int_0^{\frac{\pi}{2}} d\theta \int_{\frac{\nu}{\nu_b \sin\theta}}^{\infty} \sin^{\frac{\gamma+3}{2}}\theta F(x) x^{-\frac{1}{2}} \left(x^{\frac{1}{2}} - \left(\frac{\nu}{\nu_b \sin\theta}\right)^{1/2} \right)^{\gamma-2} dx, \tag{1.6}$$

and the break frequency is given by

$$\begin{aligned} \nu_b &= \frac{9}{4}\frac{c_1}{c_2^2}\frac{1}{B^3 t^2} \\ \frac{\nu_b}{[\mathrm{GHz}]} &= 2.52 \times 10^9 \left(\frac{B}{[\mathrm{mG}]}\right)^{-3} \left(\frac{t}{[\mathrm{yr}]}\right)^{-2}. \end{aligned} \tag{1.7}$$

This results in a spectrum that falls exponentially above the break frequency (see dashed line in Figure 1.2).

Both KP and JP cases, the break frequency is related to the elapsed time since electrons have accelerated.

In the simplified bream-jet model (Blandford & Rees 1974; Scheuer 1974) for radio lobe evolution, electrons, which are accelerated at the hot spots, are leaked out and left behind by the advancing hot spots. Therefore, the electrons at the center of the source are " older " than those closer to the hot spots. Since such " older " electrons show lower break frequency than " younger " electrons, break frequency decreases with the distance from the hot spots.

Burch (1977a and 1977b), one of the earliest studies to test synchrotron aging theory, measured spectral variation across radio galaxies 3C 31 and 3C 452, and confirmed that spectrum becomes steeper with distance from the hot spot towards the core. This study supports the basic model of radio lobe evolution. Winter et al. (1980) also confirmed similar results for Cygnus A, and yielded the synchrotron age of 6 Myr. Alexander et al. (1987) and Leahy et al. (1989) measured the spectral variation of radio lobes for a large number of radio galaxies, and derived synchrotron age of $\sim 10^6$-10^8 yr.

Most difficult issue of synchrotron-aging studies in radio lobes is that the synchrotron break occurs over a very wide range in frequency, requiring sufficient angular resolution to resolve radio source and sensitive observation over an observing range in frequency. Carilli et al. (1991) measured spectral variation in the radio lobes of Cygnus A over a very broad range in frequency, from 300 MHz to 15 GHz, and revealed detailed distribution of break frequency across the radio lobes (Figure 1.3). The spectra at the hot spots show the power-law, and break frequency decreases with the distance from the hot spots toward the core. They found the lowest break frequencies of 750 MHz is found near the core. Assuming the equipartition magnetic field (see Appendix A), they derived 6 Myr of source age.

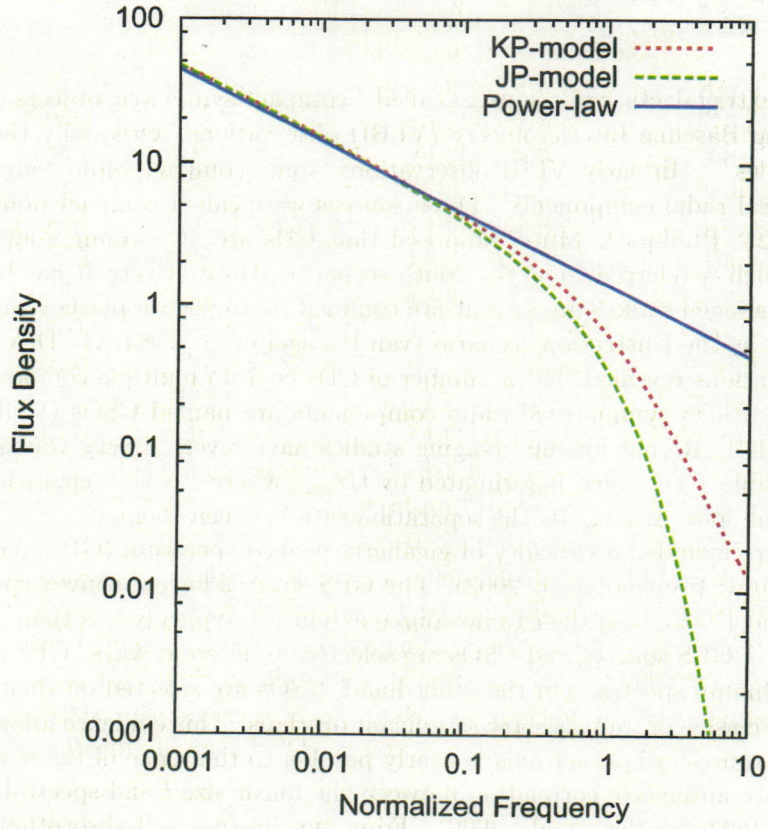

Figure 1.2: Example spectrum of KP and JP models. Solid, dotted, and dashed lines are power-law, KP model, and JP model, respectively. Horizontal axis is normalized by ν_B.

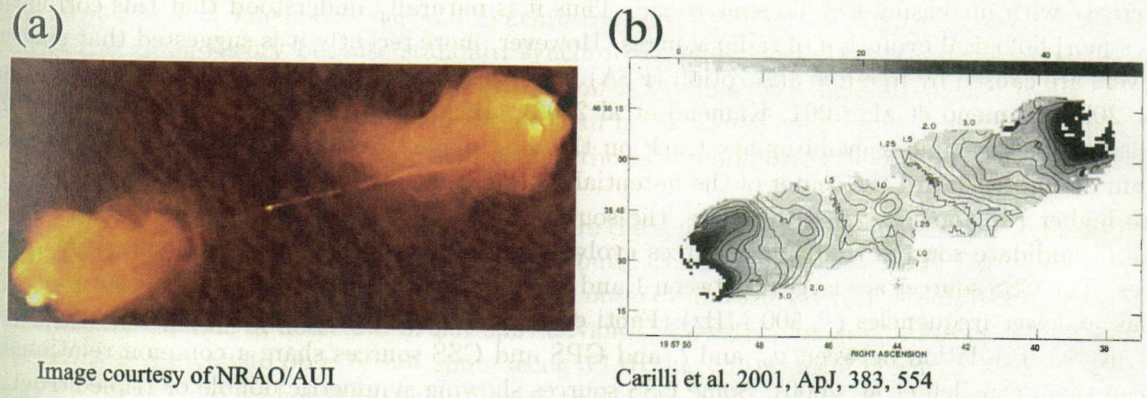

Figure 1.3: (a) Radio image of Cygnus A. (b) Image of break frequency distribution across the lobes of Cygnus A. The gray scale ranges from 0 GHz (white) to 50 GHz (black).

1.3 Compact Symmetric Objects and Evolution Scheme of Radio Source

A new sub-class in extragalactic radio sources called " compact symmetric objects (CSOs) " has found by recent Very Long Baseline Interferometry (VLBI) observations. Originally they have recognized as " compact doubles " . In early VLBI observations, some compact radio sources were proved to have two symmetrical radio components. These sources were called compact doubles (CDs; Phillips & Mutel 1980, 1982). Phiilips & Mutel proposed that CDs are at a young stage of their evolution to FRII sources, which is referred to as the youth scenario. Alternatively, it has been suggested that CDs could be normal-aged radio sources that are confined by the dense plasma and unable to escape, which is referred to as the frustration scenario (van Breugel et al. 1984; O ' Dea et al. 1991). More recent VLBI observations revealed that a number of CDs contain multiple components. Such sources with a core and two-sided symmetrical radio components are named CSOs (Wilkinson et al. 1994; Readhead et al. 1996). Recent kinematic-aging studies have revealed very young, the source age of $\sim 10^2 - 10^3$ yrs (Table 1.1), which is estimated by l/v_{sep}, where l is the separation between the hot spot and counter hot spot, and v_{sep} is the separation rate between them.

Most of CSOs are included a category of gigahertz-peaked spectrum (GPS) sources (Taylor et al. 1996; Marr et al. 2001; Kameno et al. 2003). The GPS sources have a convex spectrum that have a spectral peak around 1 GHz, and their radio-source extent are typically less than $\sim$ 1 kpc (O ' Dea et al. 1991). Samples of GPS sources and CSOs are selected in different ways. GPS sources are selected on their radio continuum spectra. On the other hand, CSOs are selected on their radio morphology. However, these two classes of sources show significant overlaps. This evidence allows us to expect that CSOs are the GPS sources whose jet-axis is nearly parallel to the plane of the sky.

GPS sources have an inverse correlation between the linear size l and spectral peak frequency ν_m (O ' Dea & Baum 1997; Snellen et al. 2000). From synchrotron self-absorption (SSA) theory, the angular size of a radio source (θ) has a relation:

$$\theta \propto B^{1/4} S_{\nu_m}^{1/2} (1+z)^{1/4} \nu_m^{-5/4} \tag{1.8}$$

where B is the magnetic field strength, S_{ν_m} is the flux density at frequency of ν_m, and z is the redshift (see Appendix B). If the SSA is the origin of spectral turnover, a spectral peak is expected to decrease with increasing a radio source size. Thus it is naturally understood that this correlation implies morphological evolution of radio sources. However, more recently it is suggested that spectral turnovers are caused by free-free absorption (FFA) by ionized gas surrounding the radio source (Marr et al. 2001; Kameno et al. 2001; Kameno et al 2003). Bicknell et al. (1997) show that the FFA can also reproduce similar evolutionary track on the ν_m-l plane. Because radial density of ambient medium increases toward the center of the potential of SMBH, smaller sources tend to have higher ν_m due to higher FFA opacity. In either case, the sources having higher ν_m are expected to be smaller in size. Candidate sources that GPS sources evolve slightly are the compact steep spectrum (CSS) sources. The CSS sources are larger (between 1 and 20 kpc in size), and have convex spectra that tend to peak at lower frequencies ($<$ 500 MHz) (Fanti et al. 1990; O ' Dea 1998). The CSS sources also show inverse correlation between ν_m and l, and GPS and CSS sources share a common relationship between them (Snellen et al. 2000). Some CSS sources showing symmetric double or triple structure are known as medium symmetric objects (MSOs). By analogy with the relation between the GPS and CSS sources, MSOs are expected to be evolved from CSOs. The radio morphologies of CSOs and MSOs are strikingly like those of FRII sources suggestive the evolutionally sequence from CSOs to MSOs to FRII sources.

Table 1.1: Kinematic Ages of CSOs

Kinematic ages where redshift is avilable					
Source	z	Size (pc)	Separation rate (c)	Age (yr)	References
B 0035+227	0.096	28.3	0.162±0.078	570±280	(1)
B 0108+388	0.669	21.0	0.164±0.009	420±20	(2)
B 0710+439	0.518	87.7	0.307±0.02	930±60	(3), (4)
B 1031+567	0.4597	113.5	0.198±0.073	1870±690	(5)
B 1245+676	0.1071	12.3	0.212±0.013	190±12	(6)
B 1843+356	0.763	20.3	0.368±0.036	180±18	(1)
B 1943+456	0.263	124.6	0.311±0.047	1300±200	(1)
B 2021+614	0.227	19.2	0.17±0.024	370±50	(7)
B 2352+495	0.238	138.6	0.151±0.035	3000±750	(1)
OQ 208	0.077	9.2	0.134±0.039	220±65	(8)
Kinematic ages where redshift is not avilable					
Source	z	Size (mas)	Separation rate (mas/yr)	Age (yr)	References
J 0204+0903		18.27	0.07±0.011	240±36	(9)
J 0427+4133[(a)]		1.33	0.06±0.013	20±4	(9)
J 1826+1831		41.87	0.013±0.006	3000±1490	(9)

Note.— (1)Polatidis & Conway. 2003, (2)Owsianik et al. 1998, (3)Owsianik & Conway 1998, (4)Owsianik et al. 1999, (5)Taylor et al. 2000, (6)Marecki et al. 2003, (7)Tschager et al. 2002, (8)Stanghellini et al. 2002, (9)Gugliucci et al. 2005 (a) Slightly resolved source. It is not obvious whether this source is categorized into CSOs or not.

1.4 Aim of this thesis

There is increasing evidence of the hypothesis that CSOs are young radio galaxies. However, the ages of FRII sources and CSOs have been estimated by different methods with each other: synchrotron-aging technique for FRII sources, kinematic aging technique for CSOs. In order to confirm the youth scenario for CSOs, it is important to measure not only kinematic age but also synchrotron age. As well, comparison of kinematic age and synchrotron age for identical sources is crucial for testing synchrotron aging theory because standard synchrotron aging theory has a number of assumptions. Primary uncertainty of synchrotron age estimation is the magnetic field strength. Synchrotron age strongly depends on the magnetic field rather than break frequency ($t \propto B^{-1.5}\nu_b^{-0.5}$). Although the minimum-energy assumption is highly uncertain, the minimum-energy field is usually adopted due to lack of better estimation.

Our primary objective of this thesis is to measure the source age by both kinematic- and synchrotron-aging studies for identical CSOs to confirm the youth scenario, and also clarify the relation between kinematic and synchrotron ages. High-resolution observation using VLBI is only the technique that is potentially capable of detection of hot spot advance. However, for large sources (MSOs and FRII sources), it is difficult to observe hot spots using VLBI due to technical problems such as sensitivity enough to detect diffuse hot spot, field of view, and so on. Therefore, CSOs are excellent laboratory for attempting both kinematic- and synchrotron-aging studies.

In chapter 2, we will report the measurements of kinematic and synchrotron ages for a compact radio source CTD 93. This is the first study that confirmed the youth scenario by both kinematic- and synchrotron-aging studies for an identical source (Nagai et al. 2006). In chapter 3, we will report the measurements of kinematic and synchrotron ages for the innermost radio source of 3C 84. Since 3C 84 is one of the nearest powerful radio sources in the universe, it allows us to study kinematics and synchrotron break distribution in detail. In chapter 4, we will expand the results from chapter 2

and 3 into MSOs and FRII sources, and give implications to radio lobe evolution. In chapter 5, we summarize the conclusion of this thesis and mention future works.

Throughout this thesis, we assumes Hubble constant $H_0 = 72$ km s^{-1} Mpc^{-1} and deceleration parameter $q_0 = 0.5$.

Chapter 2

Kinematic and Synchrotron Ages of the Compact Symmetric Object CTD 93

Abstract

We present a study of the kinematic and synchrotron ages of the Gigahertz-Peaked Spectrum (GPS) source CTD 93. Measurements of the hot spot separation over 8.5 yr show evidence of an increase. The separation rate along the source axis is $0.34\pm0.11c$, which results in a kinematic age of 2200 ± 700 yr. Assuming that two hot spots are moving apart at equal speeds, we derive an advance speed of $0.17\pm0.06c$. The radio lobe spectra show a high frequency steepening, as expected if energetic electrons lose energy by synchrotron radiation. The spectral break decreases with the distance from the hot spot in the northern component of CTD 93. This tendency is expected from the basic scenario of radio lobe evolution involving particle acceleration at the hot spots, with the radio lobes populated by high energy electrons which have leaked from the hot spots. Although a core-jet morphology for CTD 93 has previously been proposed, these results indicate that the morphology is similar to that of Compact Symmetric Object (CSO). From the spectral fits in the northern component we derive the advance speed of $0.232\pm0.005c$. The resultant synchrotron age is 1720 ± 40 yr, which shows an agreement with the kinematic age within a factor of two. Our results strongly support the hypothesis that CSOs are young radio sources.

2.1 Introduction

The luminous radio source CTD 93 (B 1607+268, J 1609+2641) is one of the earliest radio sources known to be a GPS source (Kraus et al. 1968). Its radio morphology is originally classified as CD (Phillips & Mutel 1980), and it has a spectral peak around 1 GHz (Stanghellini et al. 1998). The radio luminosity is $3 \times 10^{27} h^{-2}$W Hz^{-1} at 1.6 GHz (Shaffer et al. 1999). CTD 93 is optically identified with a galaxy of 20.3 magnitude and has a measured red-shift of 0.473 (Phillips & Shaffer 1983; O'Dea et al. 1991)[1]. This source has a quite symmetric double-lobe–like structure separating ~250 pc, and so is a candidate CSO. However, high dynamic range observations by Shaffer et al. (1999) did not find any feature between the two dominant radio components that might correspond to the core. They claimed that the northern component consists of the core and jet, while the southern component is the reappearance of the jet. Alternatively, the absence of the core candidate could be explained by synchrotron self-absorption (SSA) and/or Free-Free absorption (FFA). Another possible explanation is that the activity of the central component has stopped.

In this chapter we derive the kinematic and synchrotron ages of CTD 93. Because CTD 93 has two predominant radio components, it is possible to estimate the kinematic age by measuring separation

[1] 1 mas=4.825 pc where $H_0 = 72$ km/s·Mpc and $q_0 = 0.5$.

rate between two components. Also it is suitable to illustrate break frequency distribution since radio lobes of CTD 93 are relatively large in angular size among CSOs.

2.2 Observation and Data Analysis

The observation was carried out using ten VLBA stations at 2.244, 2.364 (13 cm), 4.99 (6 cm), 8.413 (4 cm) and 15.285 GHz (2 cm) on 2003 October 25. In addition, a single VLA antenna was used at 4.99, 8.413, and 15.285 GHz to add sensitivity to any extended structure. Figure 2.1 shows the visibilities in the (u, v) plane. We performed a number of snap shots over a wide range hour angle in order to obtain good (u, v) coverage at all frequency bands. Scans of 7 minutes were used at each frequency band except for 15.285 GHz, where 11-minutes scans were used. The total integration time consists of 11 scans at all frequency bands. Four base band converters (BBCs) were used at 4.99, 8.415, and 15.285 GHz, while two BBCs were used at 2.244 and 2.364 GHz.

We performed the data reduction using the Astronomical Image Processing System (AIPS) software package developed by the National Radio Astronomy Observatory (NRAO). Amplitude calibration for each antenna was derived using measurements of the system temperatures during the observation. Fringe fitting was performed with the AIPS task FRING. The fringe solutions of the baselines including Mauna Kea and St. Croix antennas were not determined at some time ranges at 15.285 GHz. After delay and rate solutions had been applied, the data were averaged over frequency with bandwidths of 16 MHz at 2.244 and 2.364 GHz, and 32 MHz at other frequency bands. Imaging was performed using CLEAN and self-calibration in the Difmap software package (Pearson, Shepherd, & Taylor 1994).

In the spectral aging analysis, we need to carefully consider resolution effects. The lack of short baselines could cause the missing flux for extended structures. In multi-frequency observations with an identical array configuration, the missing flux is more serious at higher frequencies. Such observations could show a steeper spectrum at higher frequencies, mimicking the effects of synchrotron losses. The Pie Town antenna and VLA antenna provide the shortest baseline length in the (u, v) coverage in our observation. At 15.285 GHz, the minimum (u, v) radius $\sqrt{u^2 + v^2}$ is about 1.2 Mλ wavelengths. This baseline length results in a missing flux of only a few percent for an extended structure of ~20 mas. Thus it is not necessary to consider the effect of missing flux as long as we are discussing the spectral aging within 20 mas.

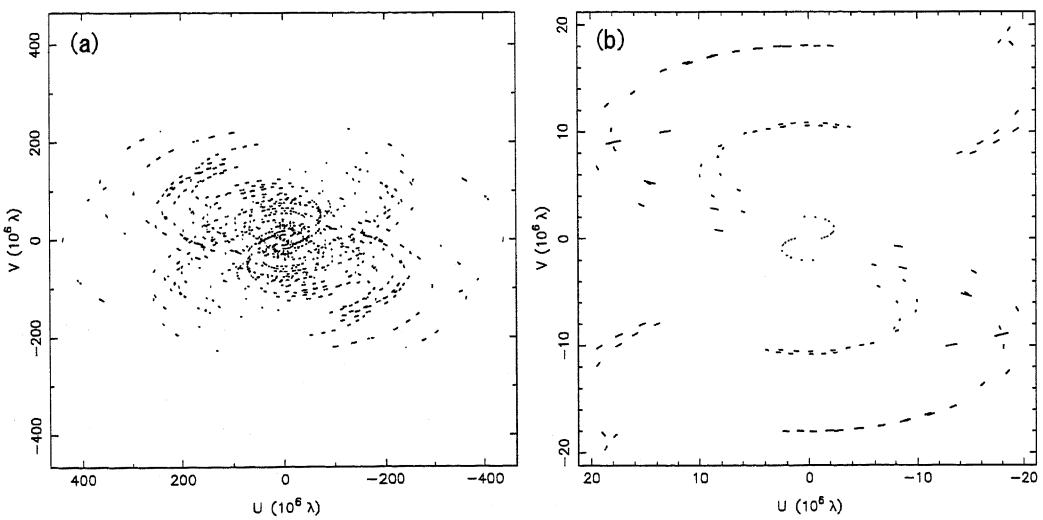

Figure 2.1: (a)The (u, v) coverage at 15.285 GHz. (b)The (u, v) coverage of the inner 20 Mλ wavelength at 15.285 GHz.

We also obtained the data sets of two archival 2 cm observations, coded BS025 (Shaffer et al. 1999) and BR077. BS025 was performed on 1995 July 23 at 15.285 GHz, and BR077 on 2002 May 5 at 15.335 GHz, both using 10 VLBA stations. The process of data reduction is the same as described above. Detailed observational parameters of BS025 are provided in Shaffer et al. (1999). The data of BR077 contains eight 8-MHz basebands with a total integration time of 13 minutes.

2.2.1 Spectral Model Fitting

The two spectral aging models, KP and JP, were fitted to the five frequency data. The fitting parameters of both models are the initial injection index γ ($\gamma = 2\alpha + 1$ where α is the emission spectrum index, defined in the sense $S \propto \nu^{\alpha}$), the break frequency ν_b, and the intensity scaling S_0. Although both models have three free parameters, we fixed the value of γ. This assumption implies no time variation of the injection rate. The injection index is related to the shock compression ratio in the Fermi acceleration process. In the case of a strong non-relativistic shock, $\gamma = 2.0$ (Bell 1978; Blandford & Ostriker 1978). However, it has been reported that γ depends on the shock conditions (Heavens & Drury 1988; Ballard & Heavens 1991). Also it is not clear what is the most plausible model for acceleration in the hot spots. A few examples which hint at the injection index for hot spots have been reported by Carilli et al. (1991) and Meisenheimer et al. (1989), who found that the hot spots in Cygnus A and three other radio galaxies have $\gamma = 2.0$. This suggests that hot spots are not far from the condition of a strong non-relativistic shock. Thus we have generally restricted our analysis to $\gamma = 2.0$, but will mention the injection index dependence of the fitting in section 2.4.4.

In the fitting process, we first performed the fitting to the ratio of intensities at two adjacent frequencies to minimize the value of $\chi^2 = \sum_{i=1,j=2}^{5}(S^{num}_{\nu_j}/S^{num}_{\nu_i} - S^{obs}_{\nu_j}/S^{obs}_{\nu_i})^2$ at each pixel in the map, where $S^{num}_{\nu_i}$ is the numerically computed flux density value, $S^{obs}_{\nu_i}$ is the observed flux density, and $\nu_{i=1,2,3,4,5}$ =2.224, 2.364, 4.99, 8.415, and 15.285 GHz, respectively. This routine provides ν_b independent of S_0. The $S^{num}_{\nu_j}/S^{num}_{\nu_i}$ was calculated in increments of 0.1 GHz for $1.5 \leq \nu_b \leq 35$ GHz. Then we searched for the S_0 which minimized the value of χ^2.

2.3 Results

2.3.1 Total Intensity & Model Fits

Total intensity images at 2.244, 4.99, 8.415, and 15.285 GHz are shown in Figures 2.2. Image performance at each frequency is listed in Table 2.1.

Table 2.1: Image performances of VLBA observations

Frequency (GHz)	θ_{maj} [a]	θ_{min} [b]	p.a. (deg) [c]	image noise r.m.s. (mJy/beam)
2.244	5.33	3.33	-18	1.03
2.364	5.06	3.1	-16.3	0.81
4.99	2.96	1.88	-14	1.3
8.415	1.81	1.17	-13.7	0.26
15.285	1.34	0.747	-18.9	0.25

Note.— [a] FWHM along major axis of beam. [b] FWHM along minor axis of beam. [c] Position angle of beam.

All images show two symmetric structures along a position angle of ~25 degrees. Total CLEANed flux of north and south component is listed in Table 2.2. The brightness peaks of the two components are separated by about 50 mas, which corresponds to 240 pc. Both components show a tail of emission

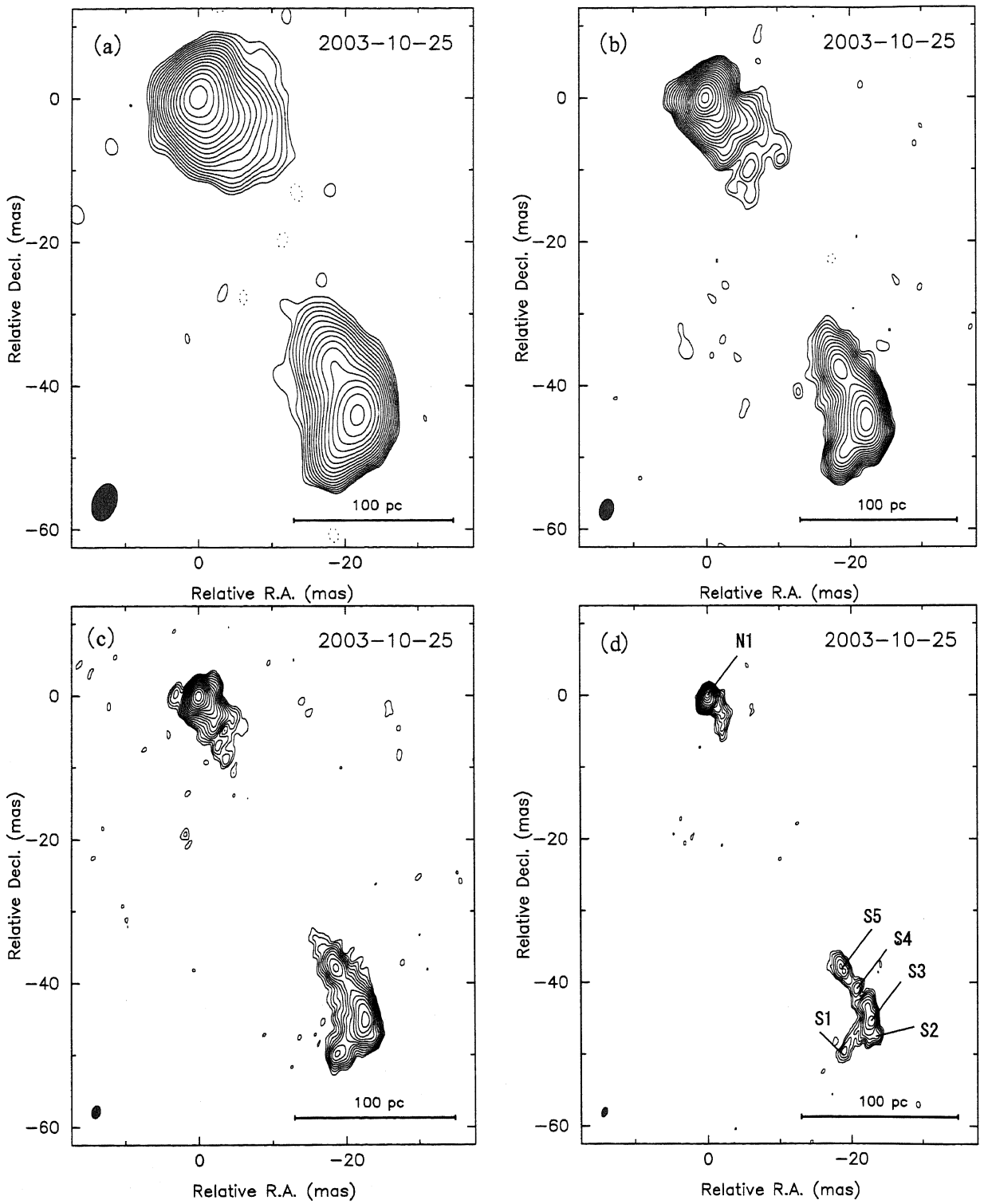

Figure 2.2: The total intensity images at (a) 2.244 GHz, (b) 4.99 GHz, (c) 8.415 GHz, and (d) 15.285 GHz. The contours are $\sqrt{2}n(n$ =-1, 1, 2, 4, ..., 512) × 3.1 mJy, 0.69 mJy, 0.717 mJy, and 0.75 mJy which are 3-times the image noise r.m.s. at the respective frequencies. The beam FWHM of each image is 5.33 × 3.3 mas at −18°, 2.96 × 1.88 mas at −14°, 1.81 × 1.17 mas at −13.7°, and 1.34 × 0.747 mas at −18.9°, respectively.

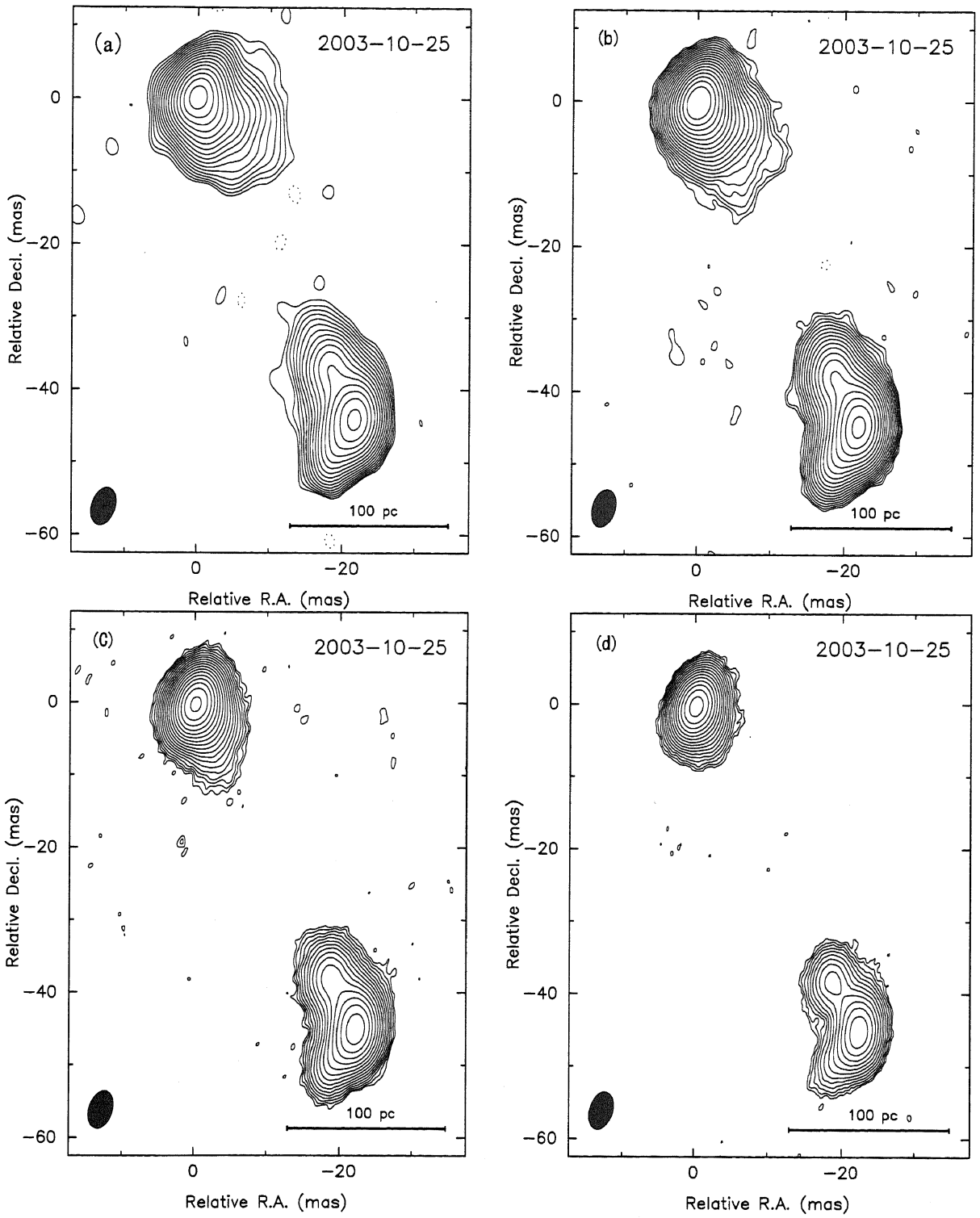

Figure 2.3: The total intensity images at (a) 2.244 GHz, (b) 4.99 GHz, (c) 8.415 GHz, and (d) 15.285 GHz. All images are restored to have the same resolution at 2.244 GHz. Contour levels are same as for Fig. 2.2

extended toward the center of the source. In the 2-cm image, the southern lobe is seen as a collimated jet and is resolved into several knotty structures (see Figure 2.2(d)). In Figure 2.3, images with the same spatial resolution at 2.244 GHz are shown.

We are interested in the relative kinematics of the components of the source. To measure the position change of components as a function of time, we compared the position of our 2-cm image with those of the previous observations BS025 and BR077. The fully calibrated images of these data sets are shown in Figure 2.4 and image performances are listed in Table 2.3. They are tapered to the same resolution of our 2-cm image.

We identified the position of each component using Gaussian model fits in the AIPS task JMFIT. We labeled the components as shown in Figure 2.2(d). Table 2.4 and Figure 2.5 show the position of each component relative to component N1 at the three epochs. The apparent separation speed of each component is summarized in Table 2.5, and the direction of motion is indicated in Figure 2.6. We detected a separation change at a significance level of about 3σ in component S3 and 1.3σ in component S5. In contrast, the separation change of component S2 is marginal, and no significant separation change is observed in other components.

2.3.2 Break Frequency Distribution

Figures 2.7 and Figure 2.8 show the distribution of the break frequency derived from the spectral fitting for the KP model. In the fitting process, we restored all images with the beam size at 2.244 GHz to match resolutions. Then the model fitting was performed as described in section 2.2.1. Since the absolute position of the map is lost to self-calibration, we identified the position of intensity peak in the northern component as a reference position between different frequencies. The inserts in the Figures 2.7 and 2.8 show the best-fit spectrum to the observed flux densities at example points together with the break frequency and reduced χ^2 of the fits. Figure 2.9 shows the sliced profile of the break frequency along the lines indicated by the arrows in Figures 2.7 and 2.8.

2.4 Discussions

2.4.1 Kinematic Age

The most significant detection of motion is seen in between the component N1 and southern hot spot (component S3), which shows a separation rate of $0.36\pm0.12c$. This separation rate is comparable to that of the hot spots in other several CSOs (e.g., Conway 2002; Gugliucci et al. 2005). The separation speed of this component projected to the source axis is $0.34 \pm 0.11c$. Assuming the components N1 and S3 are moving apart at equal speeds, we derive an advance velocity of $0.17\pm0.06c$. The resultant kinematic age is 2200 ± 700 yr. We also find a separation rate between the components N1 and S5 of $0.50\pm0.35c$ (advance speed is $0.25\pm0.18c$). The kinematic age derived from N1-S5 separation rate is 1300 ± 900 yr. These kinematic-aging studies support the youth scenario. Shaffer et al. (1999) attempted to measure the separation rate, but they could not detect significant motion over a period of nearly 20 yr at 18 cm, probably due to the lower resolution. Our result is the first detection of the motion in CTD 93.

2.4.2 Morphological Interpretation of CTD 93

2.4.2-1 CDs or CSOs?

Shaffer et al. (1999) pointed out that their observations at 2, 3.6, and 6 cm showed characteristics of a core-jet structure with the nucleus located near the northern end of the north component. They considered that the northern component is the core rather than one of the lobes for the following reasons:

Table 2.2: Total flux of north and south component

Frequency [GHz]	I_{tot} [Jy] [a]	I_N [Jy] [b]	I_S [Jy] [c]
2.244	3.19	1.746	1.444
2.364	2.971	1.627	1.344
4.99	1.437	0.811	0.626
8.415	0.692	0.415	0.277
15.285	0.311	0.21	0.1

Note.— [a] Total flux at each frequency. [b] Sum of CLEANed flux of north component. [c] Sum of CLEANed flux of south component.

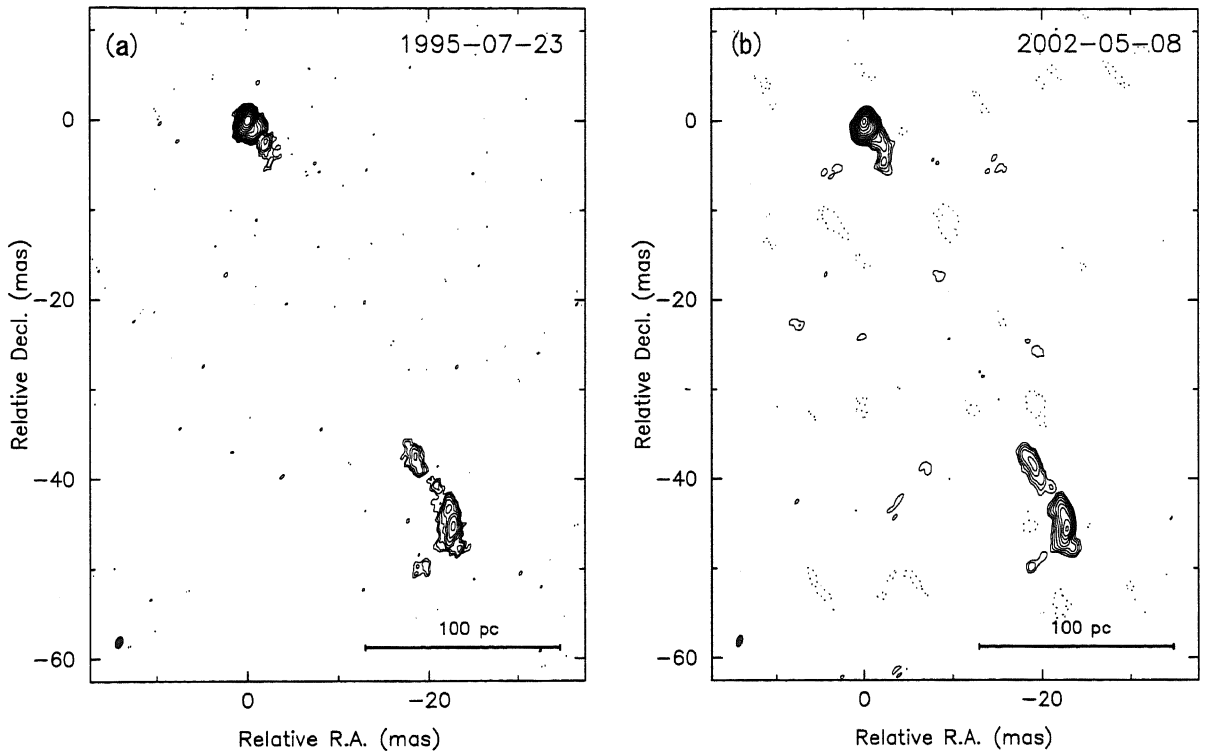

Figure 2.4: (a) VLBA contour maps of BS025 at 15 GHz and (b) BR077 at 15 GHz. Both images are tapered to same resolution of our 2-cm image. The contour levels start with 1.1 and 0.93 mJy/beam and increase from there by factors of $\sqrt{2}$.

Table 2.3: Image performances of BR077 and BS025

Obs. code	Frequency (GHz)	θ_{maj} (mas) [a]	θ_{min} (mas) [b]	p.a. (deg)	image noise r.m.s. (mJy)
BS025	15.285	1.09	0.48	-42.2	0.36
BR077	15.335	1.382	0.56	-40.4	0.31

Note.— [a,b] Beam size of original images. Note that Fig. 2.4 (a) and (b) are tapered to the same resolution of 2-cm image of 2003Oct data.

Table 2.4: The separation of each component relative to the position of component N1.

Component	Epoch	I (mJy)	x (mas)	y (mas)	r (mas)
S1	1995Jul23	7.7 ± 1.6	19.37 ± 0.22	−49.74 ± 0.17	53.38 ± 0.27
	2002May08	9.8 ± 2.6	19.14 ± 0.28	−49.25 ± 0.26	52.84 ± 0.38
	2003Oct25	10.5 ± 1.2	19.02 ± 0.07	−49.5 ± 0.1	53.03 ± 0.12
S2	1995Jul23	7.7 ± 1.0	23.23 ± 0.06	−47.5 ± 0.07	52.88 ± 0.09
	2002May08	10.5 ± 1.3	23.25 ± 0.08	−47.36 ± 0.09	52.76 ± 0.12
	2003Oct25	13.3 ± 1.0	23.32 ± 0.04	−47.27 ± 0.05	52.71 ± 0.07
S3	1995Jul23	58.2 ± 1.8	22.63 ± 0.01	−45.19 ± 0.04	50.53 ± 0.04
	2002May08	54.2 ± 1.5	22.7 ± 0.01	−45.26 ± 0.03	50.63 ± 0.03
	2003Oct25	59.8 ± 1.5	22.64 ± 0.02	−45.33 ± 0.03	50.67 ± 0.03
S4	1995Jul23	6.6 ± 1.2	20.73 ± 0.08	−40.58 ± 0.1	45.57 ± 0.13
	2002May08	6.8 ± 1.8	20.88 ± 0.21	−40.72 ± 0.23	45.76 ± 0.31
	2003Oct25	10.3 ± 1.1	20.69 ± 0.05	−40.74 ± 0.08	45.69 ± 0.10
S5	1995Jul23	18.9 ± 1.7	18.53 ± 0.06	−37.8 ± 0.1	42.1 ± 0.11
	2002May08	25.5 ± 2.2	18.73 ± 0.08	−38.0 ± 0.12	42.37 ± 0.14
	2003Oct25	26.5 ± 1.5	18.61 ± 0.04	−38.0 ± 0.06	42.31 ± 0.07

Note.— The flux density of the components is I; the separation in right ascension is x; the separation in declination is y; $r = \sqrt{x^2 + y^2}$.

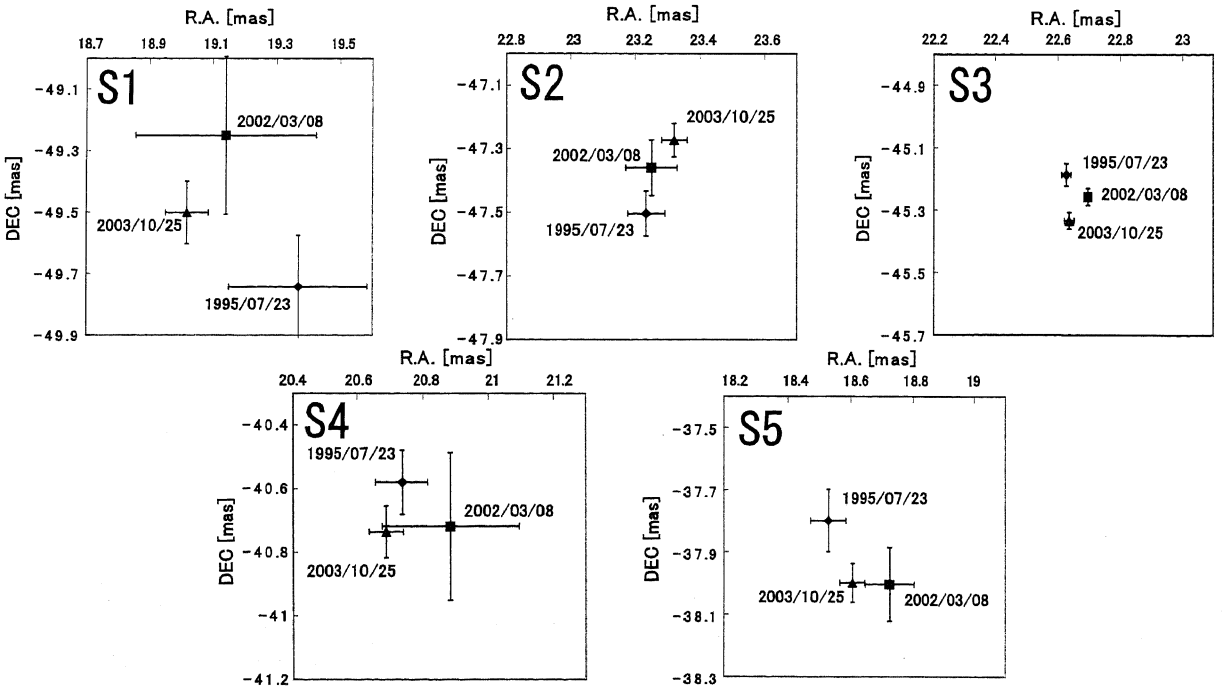

Figure 2.5: The separation of each component relative to the position of component N1 at 3 epochs. The error bars are 1 σ of Gaussian fits. The filled diamonds, filled squares, and filled triangles are the results on July 23 in 1995, on March 8 in 2000, and on October 15 in 2003, respectively.

Table 2.5: The apparent separation velocity from component N1 between our data and BS025.

Component	Separation velocity (μas/yr)	Separation velocity (v/c)
S1	-45.1 ± 98.0	-0.71 ± 1.54
S2	-27.9 ± 26.1	-0.44 ± 0.41
S3	23.0 ± 7.7	0.36 ± 0.12
S4	23.4 ± 28.1	0.37 ± 0.44
S5	31.7 ± 22.0	0.50 ± 0.35

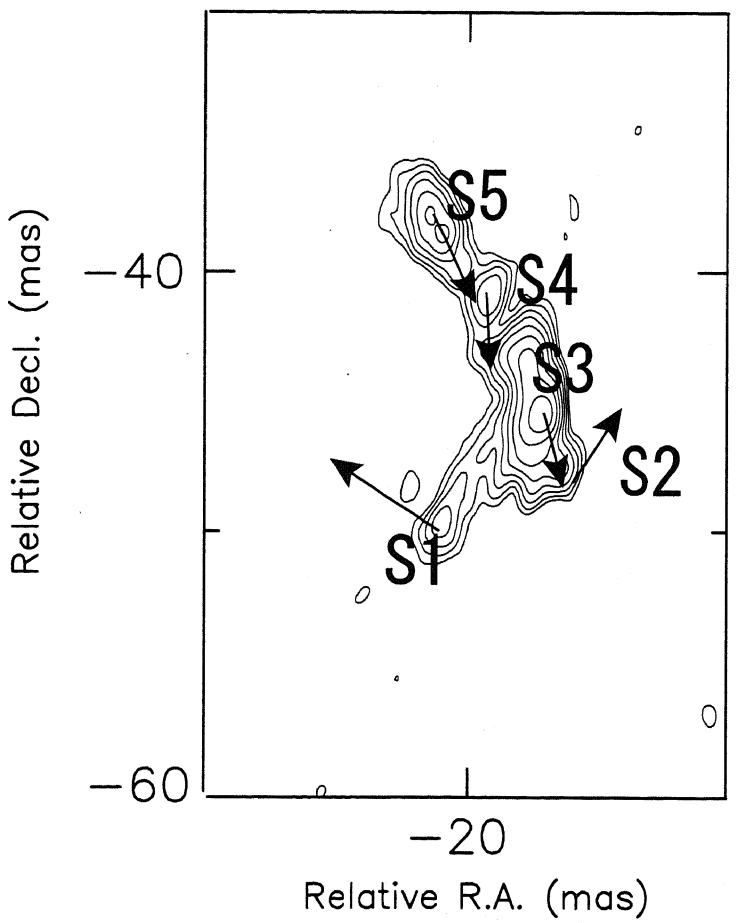

Figure 2.6: The southern lobe of CTD 93 at 15 GHz. Arrows indicate the direction of motion. The length of arrow is proportional to the velocity.

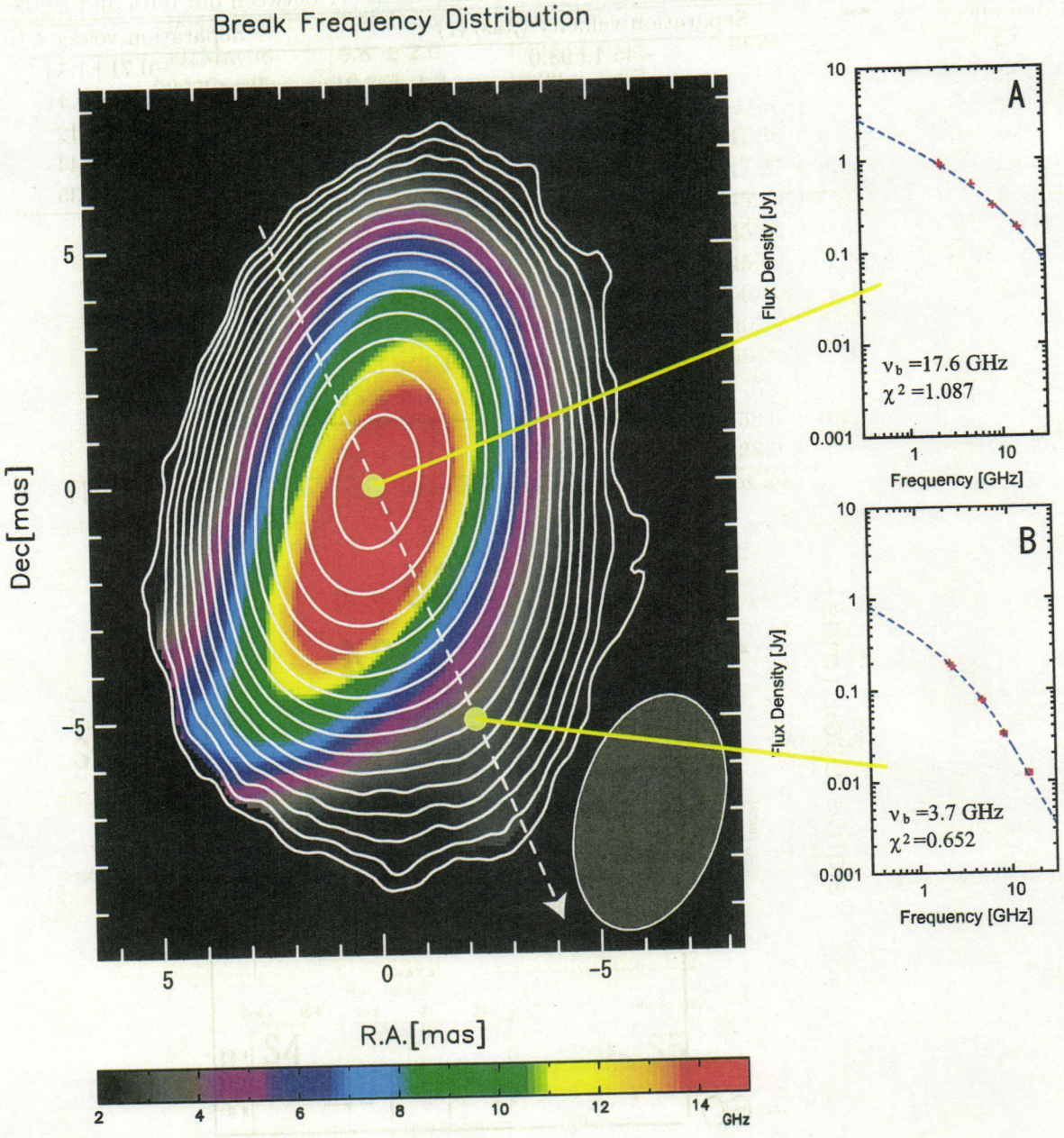

Figure 2.7: The break frequency distribution of the northern component. The contours show the total intensity at 15.285 GHz, which is tapered to the same resolution at the 2.244 GHz image. The color shows the break frequency distribution. The arrow shown in the map is the direction of the profile represented in Figure 2.9.

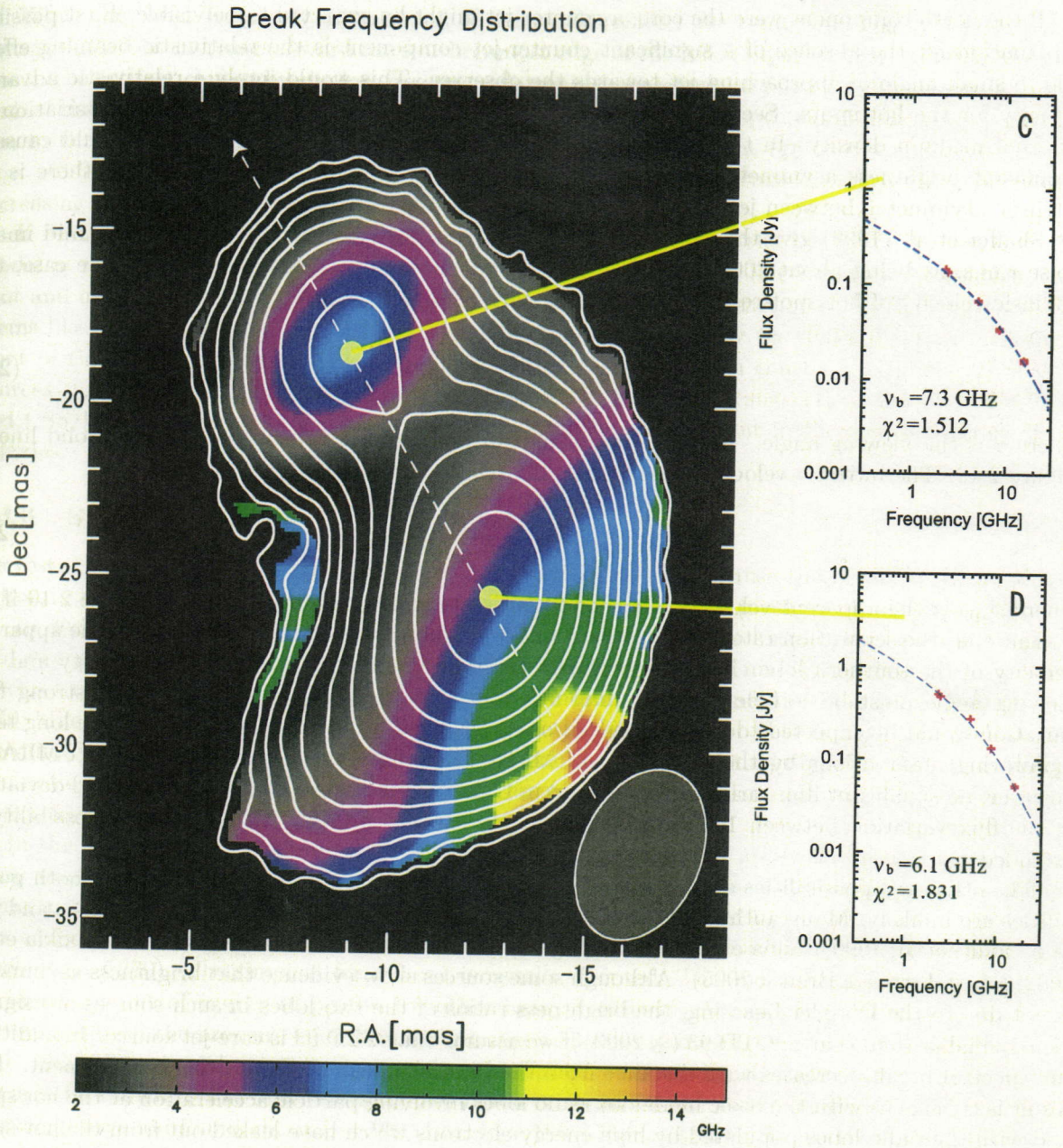

Figure 2.8: The beak frequency distribution of southern component. The contours show the total intensity at 15.285 GHz, which is tapered to the same resolution at the 2.244 GHz image. The color shows the break frequency distribution. The arrow shown in the map is the direction of the profile represented in Figure 2.9.

1. The wide opening angle of the northern component pointing toward the southwest.
2. Faint emission extending to the north of the northern component.
3. The prominence of the intensity peak of the northern component at 2 cm.
4. The lack of any feature between two dominant components.

If the north component were the core, a counter-jet might be expected to be visible. First possible explanation for the absence of a significant counter-jet component is the relativistic beaming effect due to small angle of approaching jet towards the observer. This would imply a relativistic advance velocity for the hot spots. Second possibility is a brightness asymmetry, caused by the variation of external medium density. In the dentist drill model (Scheuer 1974), such a variation could cause a significant brightness asymmetry between the two hot spots. Third possibility is that there is an intrinsic asymmetry between jet and counter-jet powers.

Shaffer et al. (1999) give the ratio between the peak intensity of southern component and image noise r.m.s. as being about 2000 at 5 GHz. If the first possibility considered above is the case, the intrinsic velocity of hot spot requires the condition

$$\left(\frac{1+\beta\cos\theta}{1-\beta\cos\theta}\right)^{2.5} > 2000, \tag{2.1}$$

where θ is the viewing angle. Thus the lower limit of the intrinsic velocity is given the solid line in Figure 2.10. The intrinsic velocity also requires the relation

$$\beta_{app} = \frac{\beta\sin\theta}{1-\beta\cos\theta}, \tag{2.2}$$

where β_{app} is the apparent velocity. This condition is shown by the dashed line in Figure 2.10 if we assume that the separation rate of the component S3 which we derived in section 2.4.1 is the apparent velocity of the southern lobe. In order to satisfy these two conditions, the intrinsic velocity and the viewing angle must be $\sim 0.9c$ and less than a few degrees, respectively. In this case, strong flux variation would be expected to be observed, as often observed in blazars. According to the long term monitoring observations by the University of Michigan Radio Astronomy Observatory (UMRAO), however, no significant flux variation is observed in CTD 93 (see Figure 2.11). The standard deviation of the flux variation between 1979 and 1999 is about 10% at 8 GHz. Thus, the first possibility is excluded.

The other two possibilities are not entirely excluded from our results, but we feel that both possibilities are unlikely. Many authors have considered the brightness asymmetries of radio lobes and jets (e.g., Fanti et al. 1990; Saikia et al. 1995; Laing et al. 1999; Ishwara-Chandra et al. 2001; Saikia et al. 2002; Pérez-Torres & Breuck 2005). Although some sources show evidence that brightness asymmetry is not due to the Doppler beaming, the brightness ratios of the two lobes in such sources are significantly smaller than that in CTD 93 (≥ 2000) if we assume that CTD 93 is core-jet source. In addition, the spectral break decreases with distance from the intensity peak of the northern component. This result is consistent with the basic model for radio lobes involving particle acceleration at the hot spots and with the radio lobes populated by high energy electrons which have leaked out from the hot spots (Blandford & Rees 1974). Thus the northern component should be interpreted as one of the radio lobes of a CSO rather than the core of the source. In following sections, we refer to the northern component as the northern lobe.

2.4.2-2 Souhtern Lobe

In the southern lobe, the spectral break, similar to the break frequency distribution in the northern lobe, moderately decreases within 5 mas from the hot spot (Figure 2.9). Then a bump of spectral break appears toward northern direction at around 8 mas from the hot spot. The tendency is opposite to that expected from the basic scenario of radio lobe evolution. In 2-cm image, the southern component

is seen as collimated jet and resolved into knots. This is probably due to the presence of underlying jet. The location of the bump of spectral break overlaps that of the knot S5 (Figure 2.9(b)). The knots could be produced by the shock in the jet (Blandford & Konigl 1979) which is causing electron acceleration. This could be why the break frequency is higher at the knot than at the hot spot.

While the break frequency distribution of the northern lobe peaked around the hot spot, that of the southern lobe increases toward the southernmost edge of the lobe (Figure 2.9(b)). This is probably due to the artifact caused by the low-frequency flattening. As shown in Figure 2.12, the southernmost limb of the southern lobe has a flat spectrum with $\alpha > -0.5$. The flat spectrum implies the absorption due to the FFA or/and SSA. Because our spectral fitting assumes the optically thin spectrum with $\alpha = -0.5$, this low-frequency flattening ($\alpha > -0.5$) affects the calculation of the spectral fitting, increasing the break frequency toward the southern edge.

If FFA is the case, dense external medium is expected in front of the hot spot. We feel that this model is reasonable. The component S1 is clearly not on the same line between the southern hot spot and northern hot spot. This southeast extension from the southern hot spot (the component S3) seems like a post-deflection flow as if the incoming jet is deflected by the dense external medium in front of the hot spot (Figure 2.13). Similar distorted structure often can be seen in the CSS/MSO sources (e.g., Mantovani et al. 2002). These distortions lead to the suggestion that the GPS/CSO and CSS/MSO are interacting with dense inhomogeneous environment in the central regions of the galaxies.

2.4.3 Synchrotron Age

We restrict the synchrotron age calculation in the northern lobe because the break frequency distribution in southern lobe shows complex behavior probably due to the presence of underlying jet.

To derive the synchrotron age, the magnetic field strength must be known. We take the magnetic field strength to minimize the total energy in relativistic electrons and magnetic field emitting a given synchrotron luminosity, so called minimum-energy condition or equipartition condition (Pacholoczyk 1970; Miley 1980; see also Appendix). We emphasize that one of our objectives in this thesis is to test the validity of synchrotron-aging study under the minimum-energy assumption. The minimum-energy assumption is uncertain, but the validity of this assumption is not discussed here. We will comment on this issue in Chapter 4.

In the calculation of minimum-energy field, k, f, ν_{max}, and ν_{min} are generally unknown parameters, where k is the total energy ratio of heavy particles to electrons, f is the filling factor of high energy particle and magnetic field, ν_{max} is the high-energy cutoff, and ν_{min} is the low-energy cutoff. The energy ratio k depends on the electron-acceleration mechanism and is ranging from 1 to 2000 (Pachloczyk 1970). The simplest form $k = 1$ is usually adopted. This means that the electron carries the same amount of energy of proton (or other heavy particles). Various authors have alerted this assumption from the pressure equilibrium argument between radio source and external gas (Krongerg et al. 1986; Feretti et al. 1990; Feretti et al. 1992; Fabian et al. 2002). However, direct measurement of k is so far difficult. The only relevant observation is the fact that measurements of cosmic ray in the solar neighborhood found about $k = 100$ (Burbidge 1959; Moffet 1975; Scheuer 1984). We tentatively calculated the minimum-energy field of northern lobe of CTD 93 and corresponding Lorentz factor of electron (γ_{min} and γ_{max}) in the condition of $k = 1$ and $k = 100$ (see Table 2.6). We assumed $f = 1$ and $\nu_{min} = 10$ MHz. The value of ν_{max} is estimated from the spectral fitting of KP model to the observed total flux spectrum, and we obtained 8.2 GHz. If we assume that electron-proton is the primary content of radio source and proton is not relativistically accelerated, $k = 1$ requires a typical electron-Lorentz factor of ~ 2000. However, γ_{max} listed in Table 2.6 is significantly smaller than 2000. So $k = 1$ is not compatible to observed ν_{max}. On the other hand, typical Lorentz factor of 20, which is expected from the condition of $k = 100$, is in the range of γ_{min} and γ_{max} listed in Table 2.6. It seems that $k = 100$ is reasonable. However, we note that $k = 1$ is still possible if the electron-positron is the

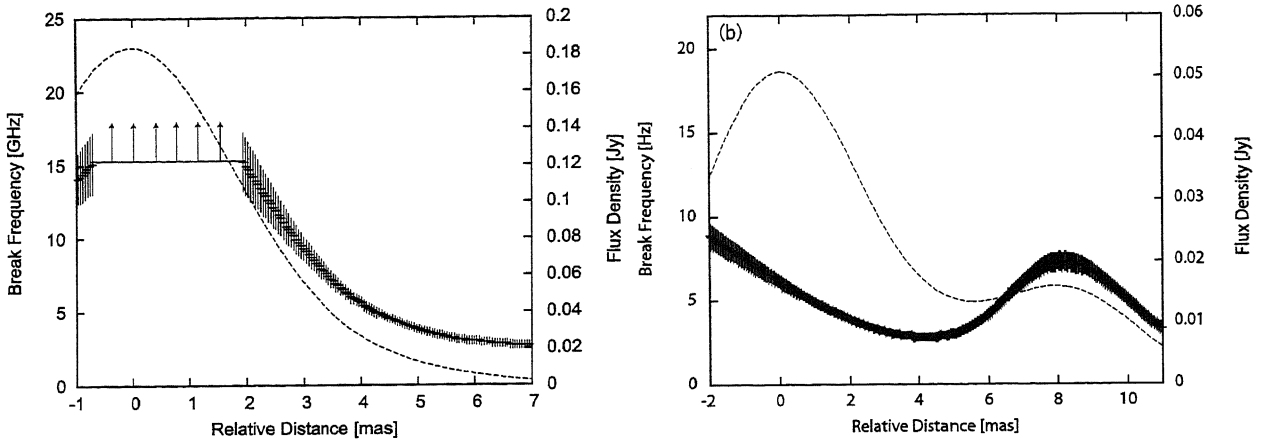

Figure 2.9: The profile of the break frequency (a) in the northern component and (b) the southern component with respect to the relative distance from the hot spot. The curved lines including error bars show the profile of the break frequency. The dashed lines show profile of total intensity. The arrows indicate lower limits.

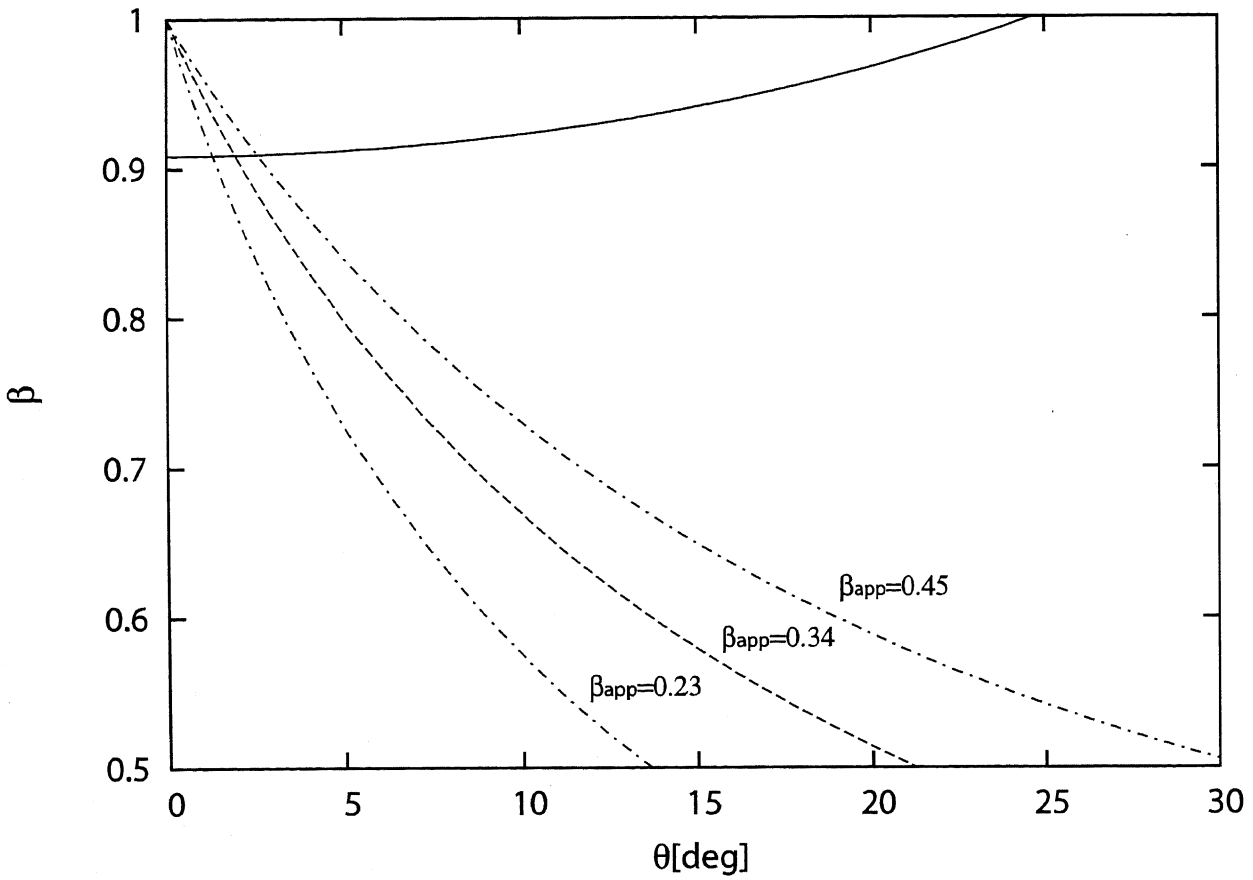

Figure 2.10: The relation between the intrinsic velocity of the hot spot and the viewing angle. The solid line is $((1+\beta\cos\theta)/(1-\beta\cos\theta))^{2.5} = 2000$, and the dashed line is $\beta\sin\theta/(1-\beta\cos\theta) = 0.34$. The dot-dashed lines indicate the 1 σ error ranges of the apparent velocity.

primary content of the radio source. In the following calculation we take $k = 100$, but discussion of k is still open.

Figure 2.14 shows synchrotron age as a function of relative distance from the hot spot along the line indicated by the arrow in Figure 2.7. The error bars reflect the errors in the fitting results for ν_b. The oldest electrons in the source are expected to reside near the core. In order to estimate the synchrotron age of oldest electrons in the source, we performed a linear fit to the synchrotron age distribution and extrapolate the age at the center of the source. Figure 2.14 shows the synchrotron age distribution calculated from the observed break frequency distribution, together with a linear fit. The synchrotron age show a linear growth with distance from the hot spot for the first ~ 6 mas, and then gradually flattening. This flattening might be artificial because observed break frequency is unreliable due to low surface brightness at the lobe edge. The linear fit in Figure 2.14(a) implies an advance velocity of $0.35 \pm 0.02c$. Extrapolating to the age at the center of the source, the age is 1230 ± 80 yr. On the other hand, extrapolating to the age at zero distance, the age does not show zero age. The zero-age offset is ~ 80 yr. This is inconsistent with the hypothesis that particle acceleration occurs at the hot spot. To reduce this contradiction, next, the fitting was performed under the condition that linear line passes through the origin and only using the data with high signal-to-noise ratio (SNR) (from 2 mas to 6 mas). The resultant linear fit in Figure 2.14(b) is an advance velocity of $0.232 \pm 0.005c$. Again, extrapolating to the age at the center of the source, the age is 1720 ± 40 yr. This age agrees with the kinematic age derived from the components N1 and S3 within a factor of two.

One could think that the separation velocity measured by synchrotron aging analysis is the sum of the advance velocity of hot spot and velocity of back-flowing material. As discussed by Carilli et al. (1991), a large back flow requires a large radio plume to hold the back-flowing material, or substantial compression of the flow near the center of the source: In the case of CTD 93, there is no evident plume and compression was observed in the center of the source by low-frequency observation by Shaffer et al. (1999). Also there is no corresponding feature in low-frequency surface brightness in other CSOs. Therefore, we neglect the effect of back-flow.

2.4.4 Injection Index Dependence of Fittings

As we mentioned in section 2.2.1, we adopted $\gamma = 2.0$ for the spectral fittings. In this section, we argue how the fitting results are sensitive to the adopted value for the injection index. To examine the injection index dependence, we fitted with three different γ. Figure 2.15 shows the sliced profile of the break frequency for γ of 2.0, 2.1, and 2.2. The break frequency increases with increasing γ. For example, break frequencies at position B in Figure 2.7 are 3.7, 4.4, and 5.1 GHz for γ of 2.0, 2.1, and 2.2, respectively. The resultant synchrotron ages are $\sim$300, 270, 255 yr for γ of 2.0, 2.1, and 2.2, respectively. Although the synchrotron age varies with the injection index, there is a clear trend for decreasing break frequency with distance from the hot spots in any injection index.

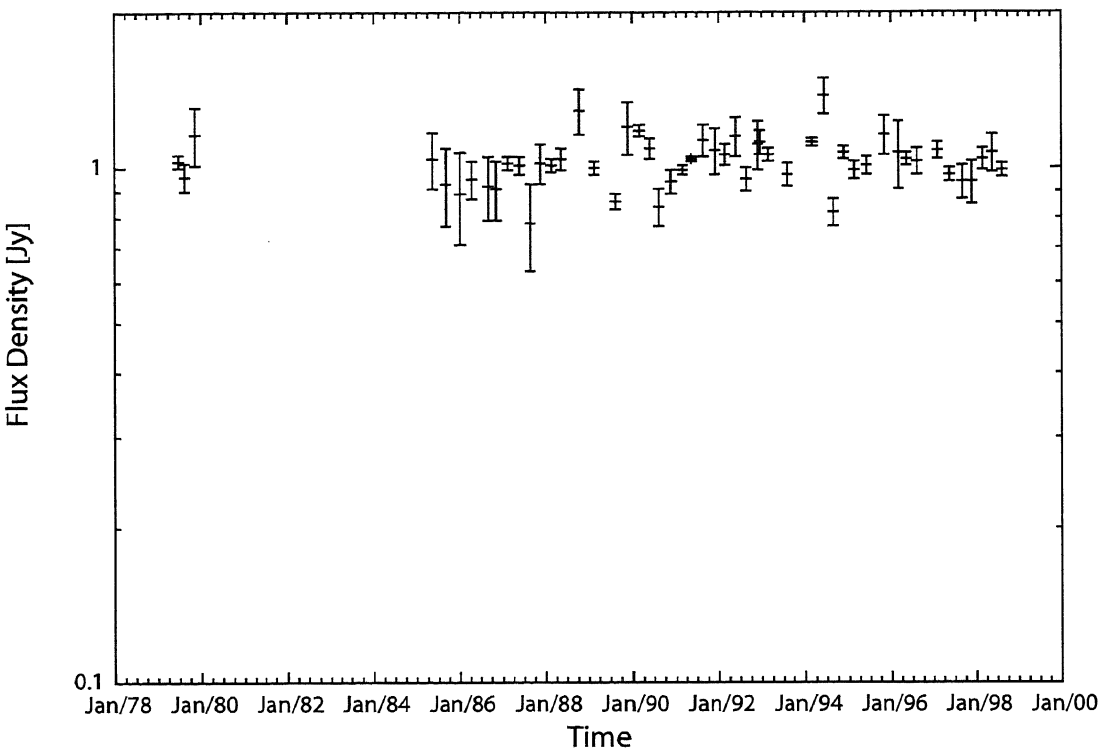

Figure 2.11: UMRAO flux monitoring from 1979 to 1999.

Table 2.6: Minimum-energy field of CTD 93.

k	B_{min} [mG]	ν_{min} [GHz]	ν_{max} [GHz]	E_{min} [erg]	E_{max} [erg]	γ_{min}	γ_{max}
1	4.7	0.01	8.2	7.2×10^{12}	2.06×10^{14}	22.5	645
100	14.3	0.01	8.2	4.1×10^{12}	1.18×10^{14}	12.9	369

Note: In the calculation, we assumed an ellipsoidal structure of 15×6 mas for the northern lobe at 6 cm. We adopted an usual assumption $\nu_{min} = 10$ MHz. The high-energy cutoff ν_{max} (break frequency) is estimated from the spectral fitting to the observed total spectrum of the northern lobe.

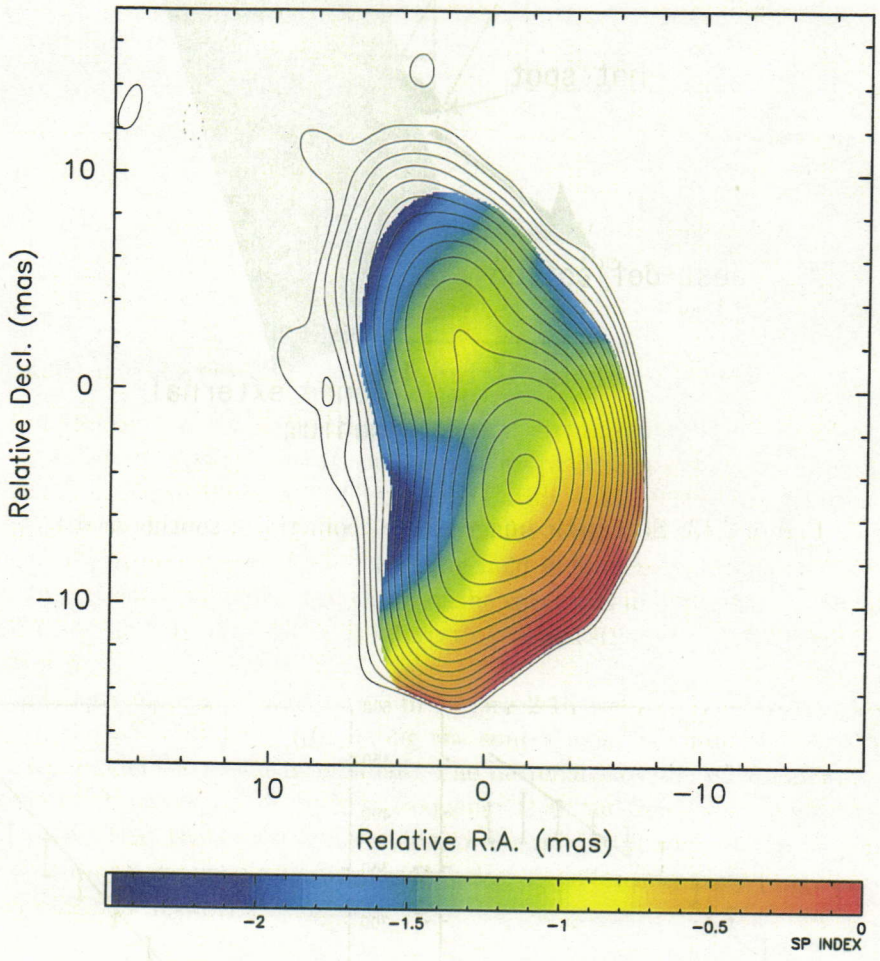

Figure 2.12: Spectral index between 2.244 and 4.995 GHz, superposed on the total intensity image at 2.244 GHz plotted by the contour.

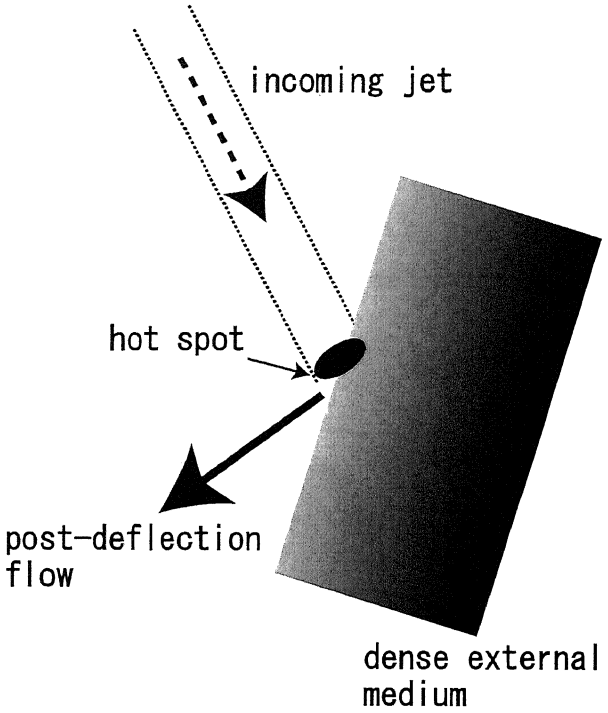

Figure 2.13: Schematic image of the geometry of southern lobe.

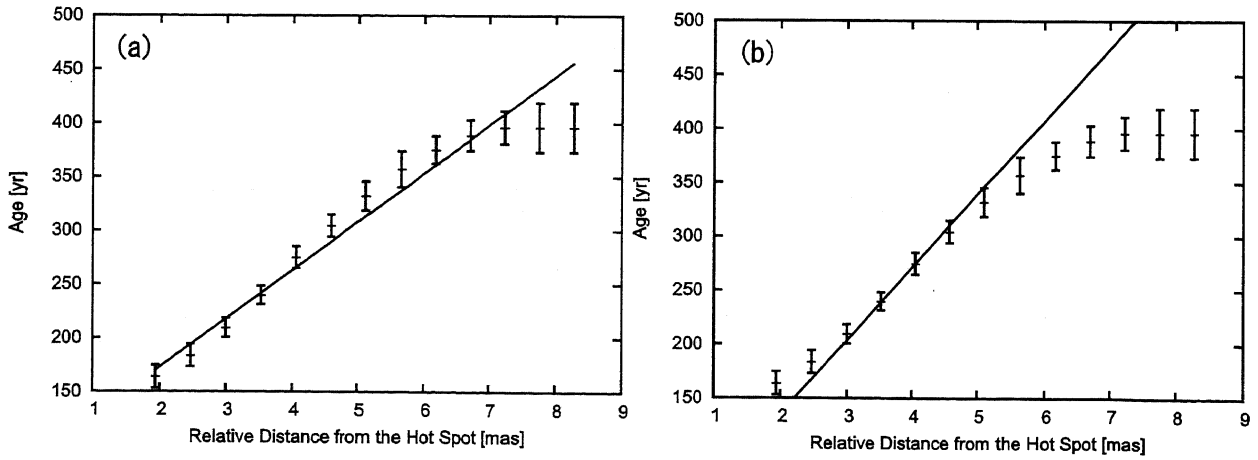

Figure 2.14: Plot of synchrotron age with respect to the distance along a line running down the center of the northern lobe. (a) The solid line indicates the linear fit to the data. (b) Same data as (a), but the linear fit was performed under the condition that linear line passes though the origin and only using high-SNR data (see text).

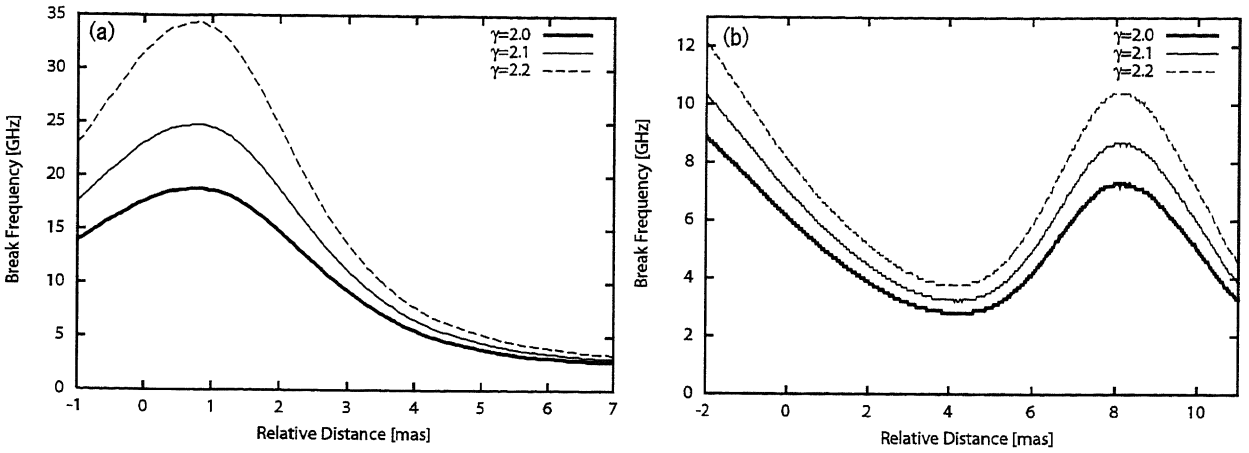

Figure 2.15: The sliced profile of the break frequency in (a) the northern component and (b) southern component. The thick, thin, and dashed lines indicate the results with $\gamma = 2.0$, 2.1, and 2.2, respectively.

2.4.5 Comparison between KP model and JP model

As we reviewed in section 1.2, the spectral aging theory is mainly modeled by two methods, the KP model and JP model. Even though the JP model is more physically reasonable, the KP model fitted the observed spectrum well in the case of Cygnus A (Carilli et al. 1991). On the other hand, Murgia (2003) reported that the JP model provides a better fit for some CSS sources. Tribble (1993) claimed that the JP spectrum in a strong random magnetic field is flattened compared to the standard JP spectrum. Thus the absence of exponential cutoff of the spectrum might not be a conclusive indication of no pitch angle scattering. In any case, it is interesting to investigate which of the KP and JP models provides the better fit.

We have fitted both models to our data. In Figure 2.16 we show the χ^2 distribution (see section 2.2.1) of both the KP and JP models along the source axis. In most regions of the source, the χ^2 values of the KP model show relatively small. The better fits by the KP model are due to a more gradual steepening of observed spectra at high frequency than the exponential cutoff of the JP model. However, we are aware that this result is not evidence for the KP model. It can be simply due to the lack of the dynamic range at our observation frequencies. A wider frequency range observation would be required to distinguish between the models.

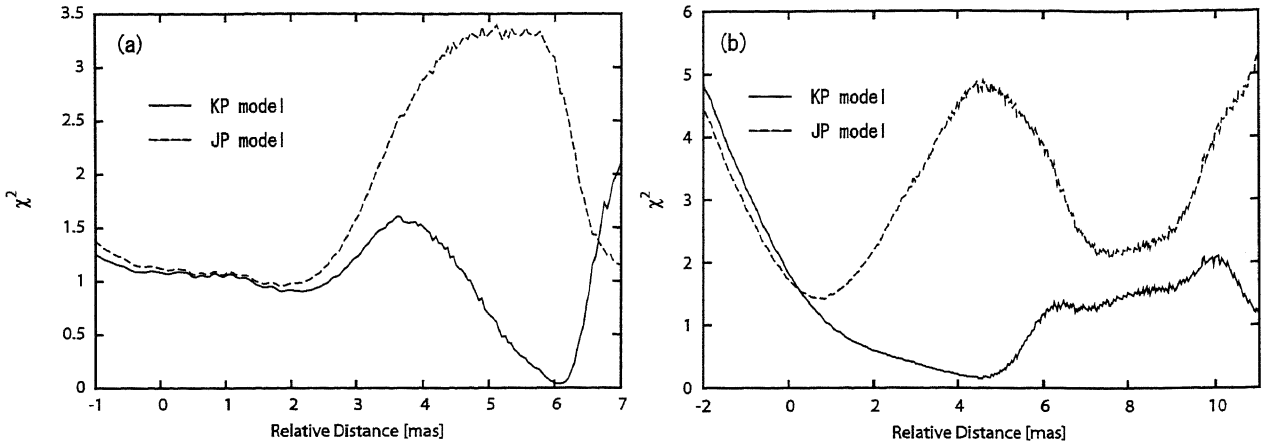

Figure 2.16: Comparison of reduced χ^2 between the KP model and JP model in (a) the northern component and (b) the southern component. Solid lines show the sliced profile of reduced χ^2 for the KP model, and dashed lines show that for the JP model.

2.5 Conclusion

By combining our VLBA observations with archival VLBA data, we revealed the source expansion of compact radio source CTD 93. The separation rate between two hot spots along the source axis is $0.34\pm0.11c$ (advance velocity is $0.17c$), and the corresponding kinematic age is 2200 ± 700 yr. The component S5, which is probably a knot in the jet, also shows the separation rate of $0.50\pm0.35c$. This yields the kinematic age of 1300 ± 900 yr.

Our multi-frequency spectrum measurement of the radio lobes shows high frequency steepening due to synchrotron aging, which is well fitted by the KP model. Although the KP model shows slightly better fits than the JP model, a wider frequency range observation will be needed to distinguish the KP or JP conclusively. In the northern lobe, the spectral break decreases with distance from the hot spot. This is consistent with the basic scenario of radio lobe evolution. The hot spot advance speed of $0.232\pm0.005c$, which is derived from the linear fit to the synchrotron-age distribution in equipartition condition, agree with the advance speed derived from the direct measurement of separation rate within a factor of two. Extrapolating to the age of center of the source, resultant age is 1720 ± 40 yr

Overall, the results show the northern component is a radio lobe rather than the core/jet as proposed by Shaffer et al. (1999). Thus we favor classification of CTD 93 as a CSO, following Wilkinson et al. (1994) and Readhead et al. (1996).

Our measurements of the kinematic age span a much shorter time than the source age. In that sense, the hot spot advance we have measured is in fact the instantaneous rate of the separation. Several mechanisms can cause instantaneous hot spot advance (Owsianik & Conway 1998), so that the kinematic aging analysis on its own is not strong proof to judge whether the source is youth or frustrated. On the other hand, the spectral break behavior along the northern component confirms that the source has indeed expanded. The combination of the kinematic and spectral aging analysis strongly supports the hypothesis that CSOs are young sources.

Chapter 3

The Kinematic and Synchrotron Ages of the Innermost Radio Lobe of 3C 84

Abstract

The kinematic- and synchrotron-aging analyses for the innermost radio lobe of 3C 84 are reported in this chapter. Multiepoch VLBA observations revealed the hot spot advance of 0.43±0.06c, which results in a kinematic age of 33±5 yr in 2000. This is consistent with the scenario that innermost radio lobe is associated with the 1959 outburst of activity. The spectral break, which is due to the electron-energy depleting by the synchrotron radiation, decreases with the distance from the hot spot. The lowest break frequency in the source is 2.3±1.4 GHz, yielding the synchrotron age of 24^{+14}_{-5} yr in 1995 assuming minimum-energy field. The kinematic and synchrotron ages agree well with each other.

3.1 Introduction

The bright radio source 3C 84 is associated with the giant elliptical galaxy NGC 1275 (z=0.0176; Strauss et al. 1992)[1], which is the cD galaxy of Perseus cluster (Optical image of NGC 1275 is indicated in Figure 3.2(a)). The radio flux began to increase significantly from 1959 (Figure 3.1). It attained ~60 Jy at 8 GHz in 1983, and has been decaying and currently below 20 Jy at centimeter wavelengths. The radio structure of 3C 84 is complex. In inner 10 pc scale, the bright radio source extends to about 15 mas. It is clearly related to the jet emanating from the core, and radio lobe. The counter-jet component about 8 mas south of the core was found by high-dynamic range VLBI observation (Walker et al. 2000, hereafter W2000 in this thesis). Recent high resolution observations with VLBI Space Observatory Programme (VSOP) confirmed that the bright southern lobe is expanding (Asada et al. 2006). The apparent expansion velocity relative to the core is about 0.5c. This yields the kinematic age of about 46 yr in 2001, which is consistent with that this feature is formed from the 1959 outburst. Beyond the bright southern lobe, extended emission centered at ~75 mas south of the core is confirmed by low-frequency VLBI observation (Silver, Taylor & Vermeulen 1998, hereafter STV). This is probably the remnants of earlier activity. STV also found a radio "millihalo" on ~ 250 mas scale at 330 MHz. Several knot-like components, which are probably related to a jet, surrounded by very diffuse halo were found on arc-minutes scale, but their morphology is somewhat like the radio lobe (Pedlar et al. 1990). All these radio features may indicate intermittent activity of jet ejection from the central engine.

Recent X-ray observations show that the arc-minutes scale radio lobes of 3C 84 clearly interact with the X-ray emitting intercluster medium (ICM). This leads to X-ray holes in the ICM (Bohringer

[1] 1 mas=0.345 pc where H_0=72 km s^{-1} Mpc^{-1} and $q_0 = 0.5$.

et al. 1993; Churazov et al. 2000; Fabian et al. 2000). Furthermore, deep Chandra observations have revealed the presence of " ripples " in the ICM that are suggestive of sound wave emanating from 3C 84 (Fabian et al. 2003; Figure 3.2(b)). They calculated the radio source lifetime and time-scale of propagation of ripples, and attributed that an intermittent radio source is producing the observed ripples (Figure 3.2(c)). 3C 84 might provide sufficient energy to heat ICM against cooling flow, as predicted by other clusters (Churazov et al. 2001; Croston, Hardcastle, & Birkinshaw 2005; McNamara et al. 2005). To estimate the cycle of activity of radio source is crucial to prove the relation between radio source and ICM heating. Thus it is important to study radio source age on multi-scale.

In inner 10 pc, the northern and southern features show symmetric structure at the frequency higher than 15 GHz (W2000). Its morphology is quite similar to CSOs. Also the expanding velocity of southern lobe is comparable to those of other CSOs (Asada et al. 2006). Although 3C 84 is not categorized into GPS sources, the spectral property of inner 10 pc feature is similar to GPS sources. W2000 studied the FFA opacity distribution. The core and counter-jet components are strongly absorbed, and they claimed that the morphology is consistent with absorption by ionized gas associated with an accretion disk. Combination of VLBA and VSOP observation also revealed similar absorption feature (Asada et al. 2000; hereafter A2000). Such absorption feature is observed in other GPS sources (Kameno et al. 2003). Especially in NGC 1052, detailed spatial distribution of FFA opacity is revealed (Kameno et al. 2001). They proposed that a dense plasma torus in the central $\sim$ 1 pc caused by FFA. Overall results manifest that the nature of inner 10 pc feature of 3C 84 is similar to that of other CSOs and GPS sources.

In this chapter we present the results of VLBA observation towards inner 10 pc feature of 3C 84 to study the radio lobe expansion and distribution of synchrotron break. Inner 10 pc feature is probably the youngest radio source. Therefore it is the best source to investigate the radio lobe evolution. Besides, 3C 84 is the nearest CSO in the universe. The large number of resolution elements across the radio lobe allows us to study detailed kinematics and spatial distribution of synchrotron break.

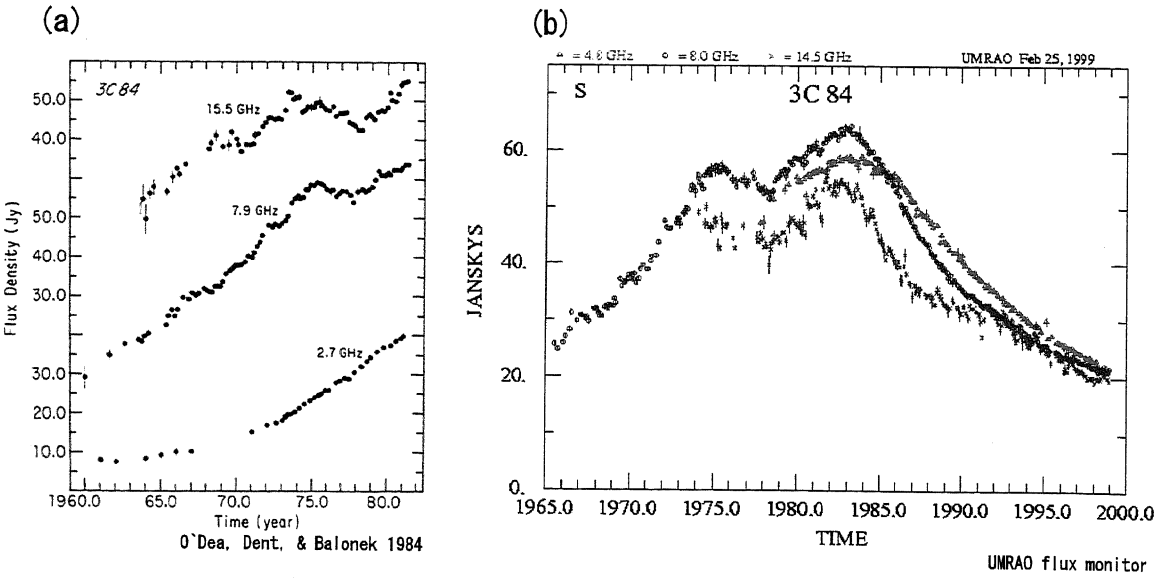

Figure 3.1: (a)The flux density of 3C 84 at 2.7, 7.9, and 15.5 GHz as a function of time. O'Deal, Dent, & Balonek 1984. (b) Flux monitoring by University of Michigan Radio Astronomy Observatory.

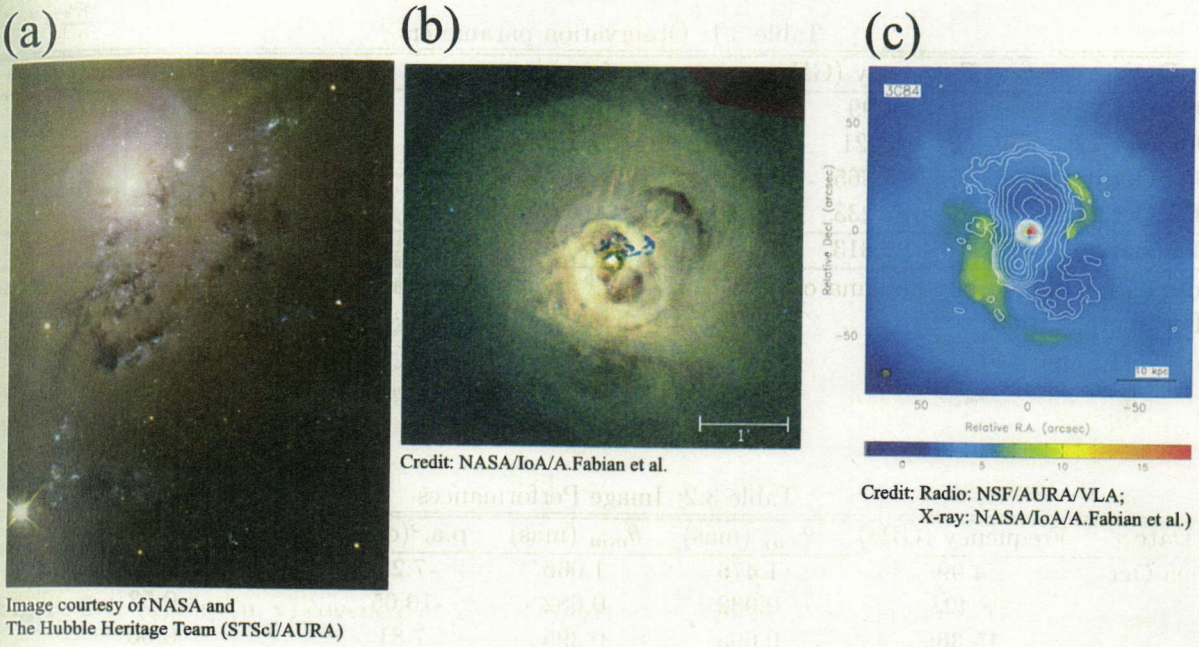

Figure 3.2: (a) Optical image of NGC 1275. (b) X-ray image of NGC 1275. The dark cavities ("ripples") are thought to be buoyant magnetized bubbles of energetic particles produced by energy released from the vicinity of the black hole. (c) X-ray image overlaid on the contour of radio image of NGC 1275. X-ray cavities coincide with the radio source, indicating interaction of radio source and ICM.

3.2 Observations & Data Analysis

The observation was carried out ten VLBA stations together with a single VLA antenna at 4.99 (6 cm), 8.421 (4 cm), 15.365 (2 cm), and 22.233 GHz (1.3 cm) in October 1995, and ten VLBA stations together with a single VLA antenna and the Efferesberg station (EB) at 21.813 GHz in January 2000. Detailed observation parameters are listed in Table 3.1. Figures 3.3 and 3.4 show the visibilities in the (u, v) plane. Observations consisted of a number of scans over a wide range hour angle to obtain good (u, v) coverage. The shortest baseline between Pie Town and VLA avoids missing flux over the extent of inner 10 pc feature. However, due to a problem with the system temperature measurement, we did not get usable data from Hancock antenna in January 2000. We used 2 channels of 8 MHz bandwidth at each frequency.

We performed the data calibration using NRAO AIPS. The *a-priori* calibration was derived using the measurements of system temperature during the observation. The fringe-fittings were performed using AIPS task FRING. All baselines successfully detected significant delay and delay-rate solutions during the observations. After applying delay and delay-rate solutions, we examined band pass characteristics of complex visibilities and flatten the characteristics over pass-band using AIPS task BPASS. Then the data were averaged across bandwidth of 16 MHz at all frequencies. Imaging was performed using CLEAN and self-calibration in Difmap software package. Fully calibrated image performances are listed in Table 3.2.

Table 3.1: Observation parameters

Date	Frequency (GHz)	Antennas	Total integration time (min)
1995 Oct 22	4.99	VLBA	248
1995 Oct 22	8.421	VLBA	246
1995 Oct 09	15.365	VLBA, VLA[a]	315
1995 Oct 21	22.233	VLBA, VLA[a]	325
2000 Jan 26	21.813	VLBA, VLA, EB[b]	285

Note.— [a] Included one antenna only of the VLA. [b] Included one antenna only of the VLA and the Efferesberg station

Table 3.2: Image Performances

Date	Frequency (GHz)	θ_{maj} (mas)	θ_{min} (mas)	p.a. (deg)	image noise r.m.s. (mJy)
1995 Oct	4.99	1.476	1.066	-7.25	0.88
	8.421	0.932	0.682	-10.05	0.53
	15.365	0.605	0.395	-7.81	0.86
	22.233	0.411	0.344	37.94	1.11
2000 Jan	21.813	0.367	0.195	-18.9	0.88

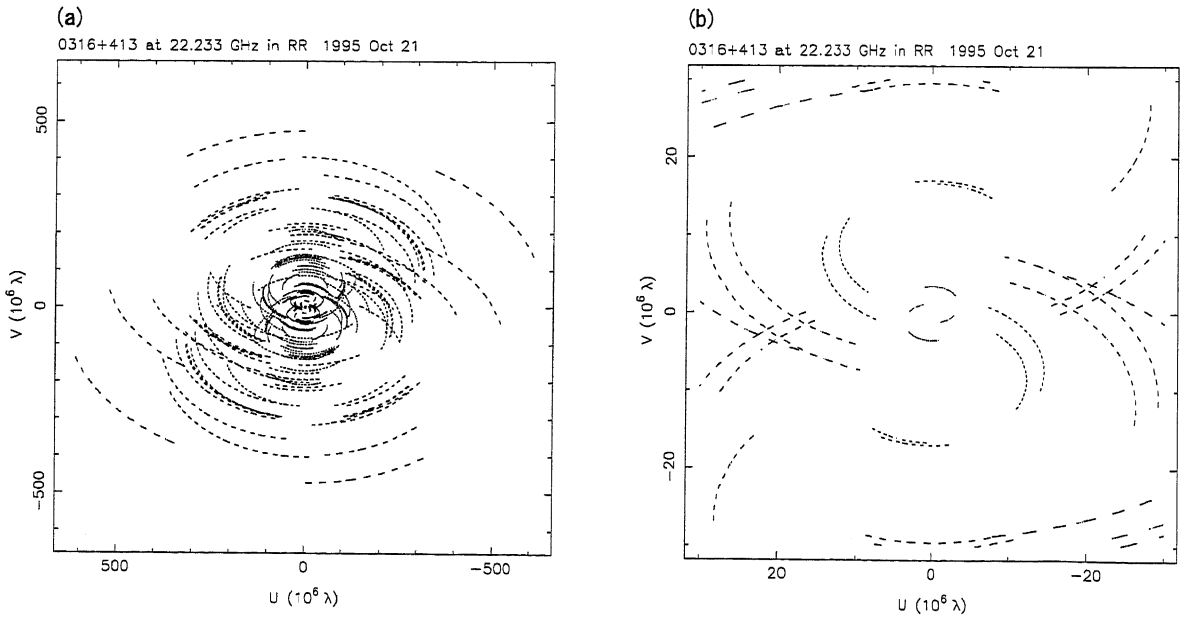

Figure 3.3: (a)The (u, v) coverage at 22 GHz on 1995 Oct 21. (b)Inner 30 Mλ of the (u, v) coverage.

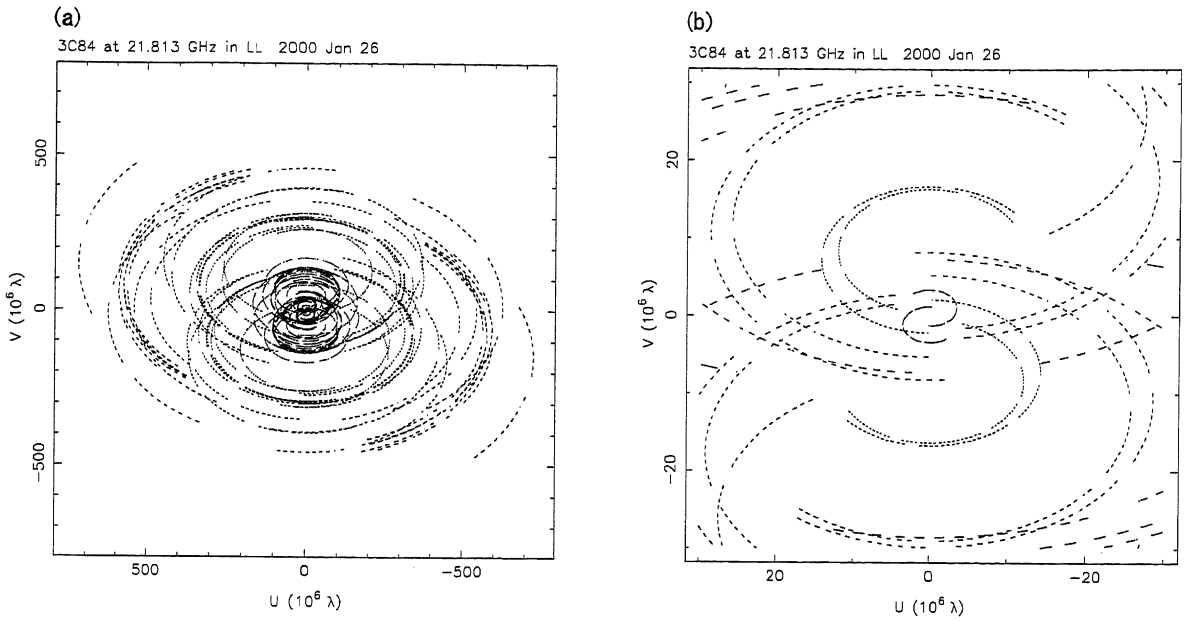

Figure 3.4: (a)The (u, v) coverage at 22 GHz on 2000 Jan 26. (b)Inner 30 Mλ of the (u, v) coverage.

3.3 Results

3.3.1 Total Intensity and Model Fittings

Contour plots of observation in 1995 are shown in Figures 3.5 and 3.6. A thin jet feeding the southern lobe is clearly seen. The southern lobe has a sharp edge on its surface brightness towards south, and forms bow structure. Northernmost counter feature, which also shows a sharp edge on its surface brightness, is seen at all 4 frequencies. A counter jet components leading to northernmost feature from the core becomes brighter with increasing frequency, as seen in W2000 and A2000.

A total intensity image from 2000 observation is shown in Figure 3.7. Efferesberg station constituting the longest baseline provides better resolution than observation in 1995. The core is resolved into multiple components, which show a wiggle structure of the jet feeding the southern lobe.

We identified components in the core region by gaussian model fitting for some of the analysis below. Figure 3.8 and Table 3.3 show model fitting results using AIPS task JMFIT. Four components were obtained from the fitting in 1995 observation. These components are labeled C11, C12, C13, and C14. On the other hand, three components, labeled C21, C22, and C23, were obtained from 2000 observation. The component C20 is barely resolved, obtained by gaussian model fitting for the super-resolution image. We also identified components in the southern lobe and the northern counter-lobe (Figures 3.9 and 3.10). Their physical parameters are listed in Tables 3.4 and 3.5.

3.4 Discussion

3.4.1 Kinematics

In this section, we discuss the kinematics of both southern and northern lobes. Since the absolute position of the images is lost to self-calibration, a reference position between two epochs must be determined. By making use of FFA opacity distribution by W2000 and A2000, the geometry of 3C 84 can be illustrated as shown in Figure 3.11. Thus the northernmost component in the bright core region (C11 and C20) is presumably the central core. However, as discussed by Dhawan et al. (1998), the component C11 could be a counter-jet component. For convenience, we will generally consider

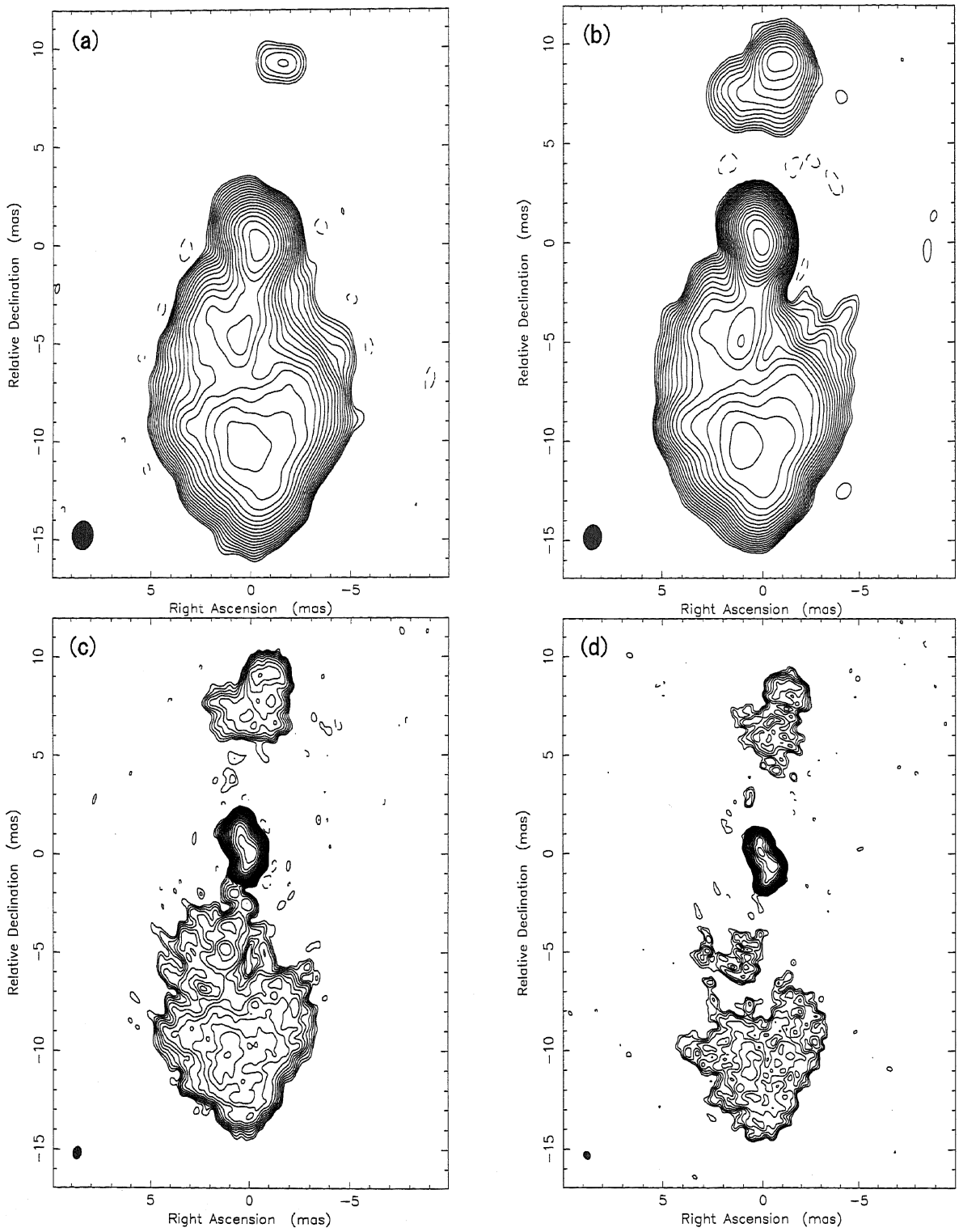

Figure 3.5: Total intensity images in 1995 at (a) 4.99 GHz, (b) 8.421 GHz, (c) 15.365 GHz, and (d) 22.233 GHz. Contours are 3 times image noise r.m.s. (see Table 3.2) increasing from there by factors of $\sqrt{2}$.

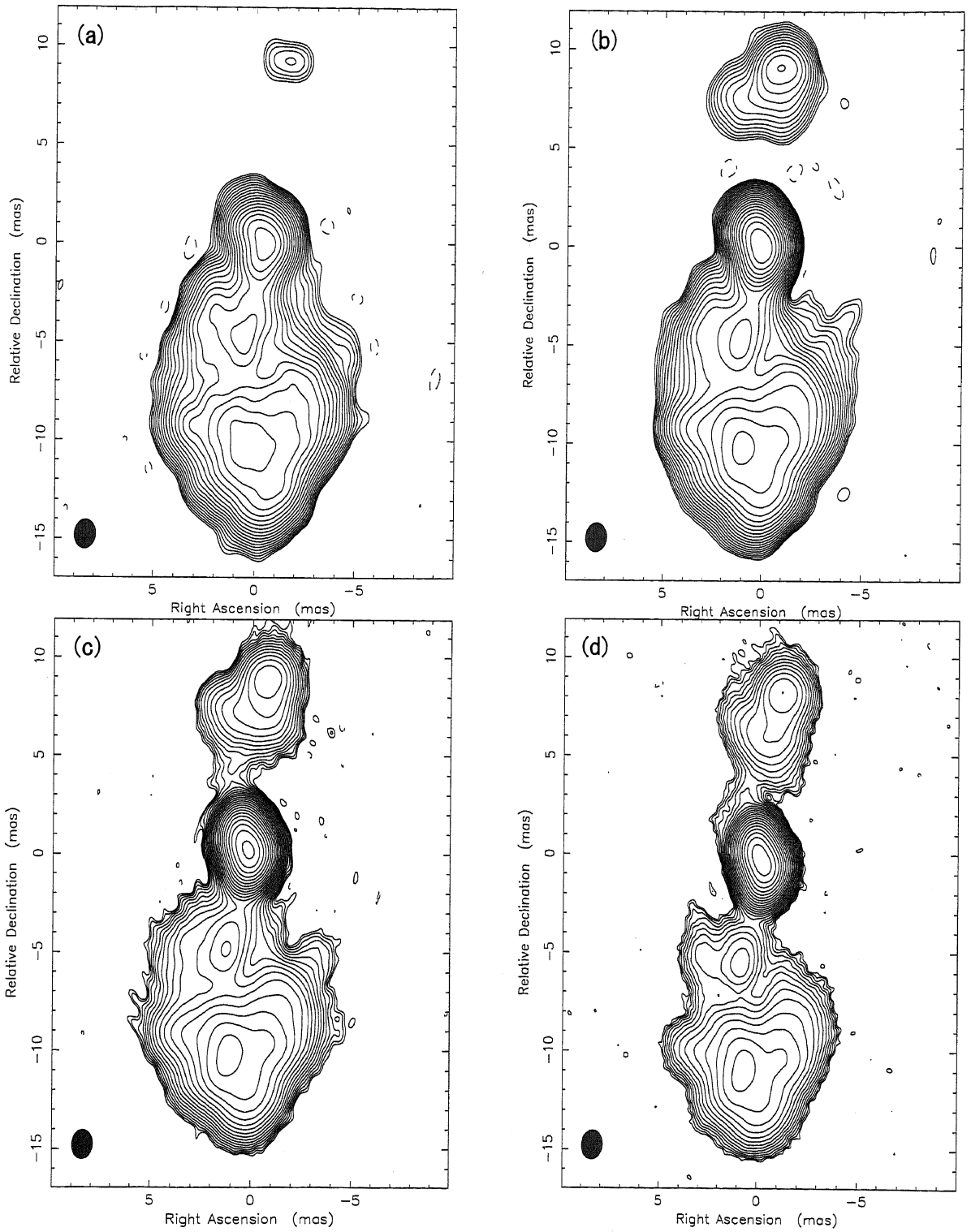

Figure 3.6: Same as Fig. 3.5, but all images are are restored to the same resolution at 4.99 GHz.

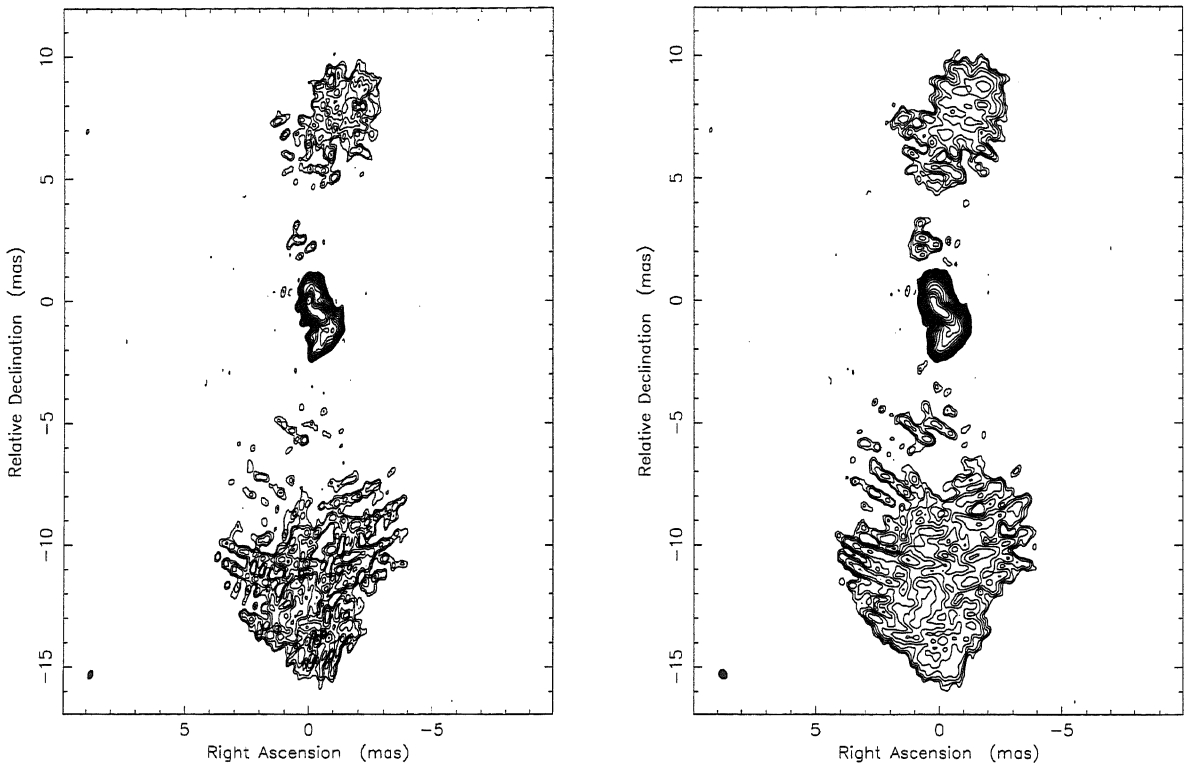

Figure 3.7: (a) Contour plots of observation in 2000. Contours are a 3 times image noise r.m.s. (see Table 3.2) increasing from there by factors of $\sqrt{2}$. (b) Same as (a), but restored to the same resolution at 22 GHz in 1995 (Fig. 3.5(d)).

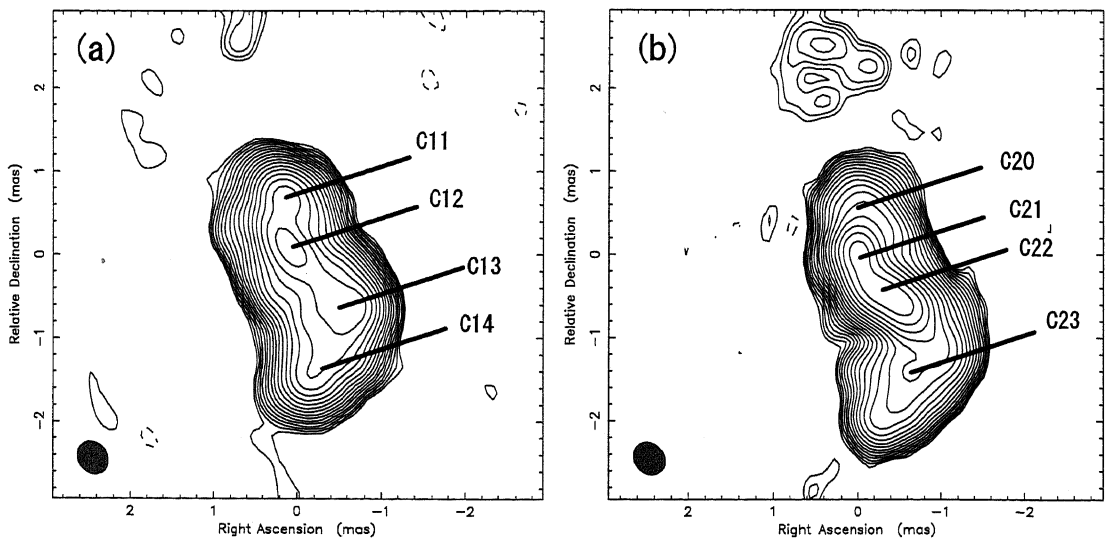

Figure 3.8: Core region in (a) 1995 and (b) 2000. Both images are restored to the same resolution at 22 GHz in 1995. Contour levels of (a) and (b) are same as for Figures 3.5(d) and 3.7(b), respectively. The components labeled C11~C14 and C20~C23 are obtained by gaussian model fittings (Table 3.3).

Table 3.3: Gaussian model fitting results at 22 GHz in the core region.

Component	I_{peak} (Jy)	I_{tot} (Jy)	x (mas)	y (mas)	θ_{maj} (mas)	θ_{min} (mas)	p.a. (deg)
			1995 October				
C11	0.788	2.024	−0.147	0.687	0.675	0.554	1.33
C12	1.023	4.154	−0.08	0.144	1.095	0.540	28.09
C13	0.771	4.868	0.518	−0.507	1.17	0.784	83.18
C14	0.444	1.445	0.25	−1.252	0.844	0.562	133.92
			2000 January				
C20	0.04	0.271	−0.11	0.676	0.424	0.16	32.77
C21	1.164	3.793	−0.043	0.004	1.016	0.457	16.96
C22	1.305	4.458	0.34	−0.396	1.038	0.469	54.86
C23	0.255	1.19	0.654	−1.379	0.972	0.684	134.37

Note.— I_{peak}:Peak intensity of the component. I_{tot}:Integrated intensity of the component. x:Component position along the R.A. relative to the center of the map. y:Component position along the DEC relative to the center of the map. θ_{maj}: Major axis of the component. θ_{min}: Minor axis of the component. p.a.: Position angle of the component.

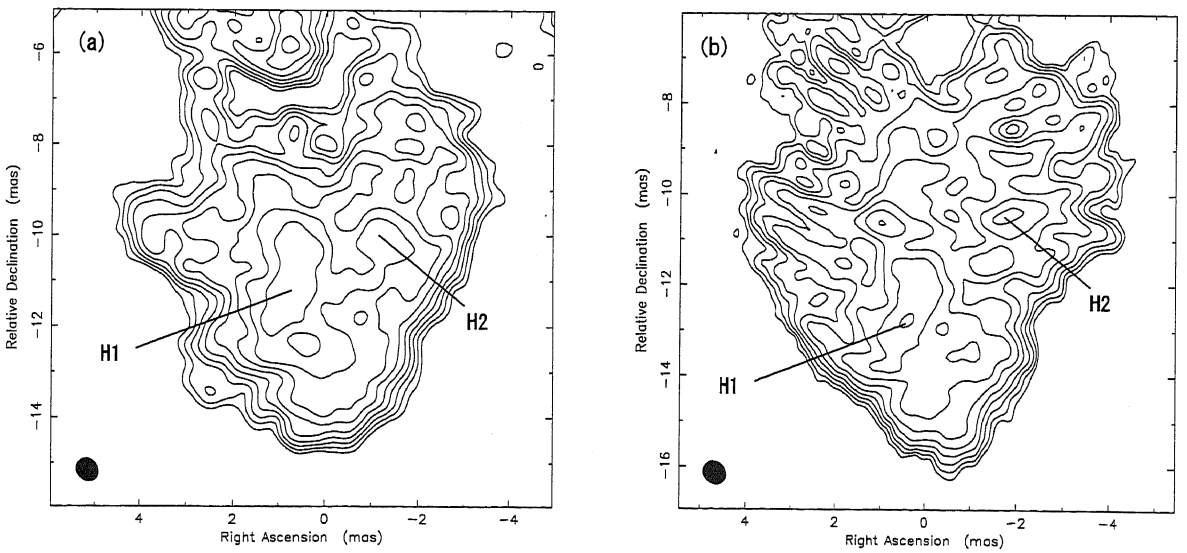

Figure 3.9: The southern lobe at 22 GHz in (a) 1995 and (b) 2000. Both images are restored to the beam of 0.533×0.458 at position angle of 40°, which is the beam size of naturally-weighted resolution at 22 GHz in 1995, to enhance the components. Contour levels of (a) and (b) are same as for Figures 3.5(d) and 3.7(b), respectively.

Table 3.4: Gaussian model fitting results at 22 GHz in the southern lobe.

Component	I_{peak} (Jy)	I_{tot} (Jy)	x (mas)	y (mas)	θ_{maj} (mas)	θ_{min} (mas)	p.a. (deg)
			1995 October				
H1	0.0747	0.7579	−0.7	−11.09	1.79	1.39	138.64
H2	0.0464	0.8562	0.89	−11.38	2.34	1.92	163.46
			2000 January				
H1	0.026	0.3837	−0.41	−12.69	2.21	0.95	140.41
H2	0.0285	0.2926	1.17	−11.99	1.881	1.33	110.11

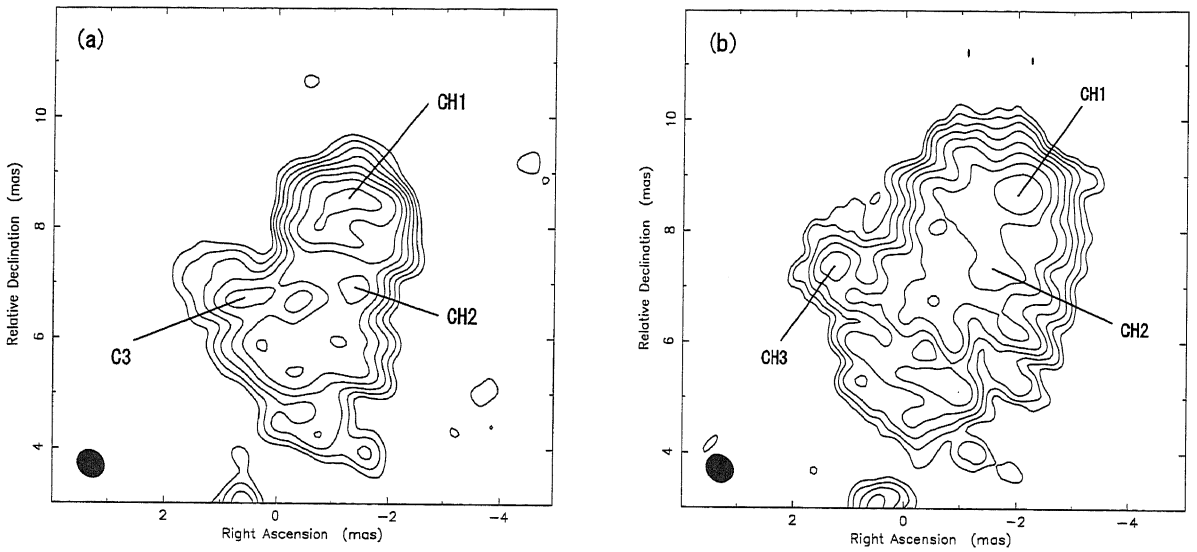

Figure 3.10: Contour plots in (a) 1995 and (b) 2000 in the northern counter-lobe. Both images are restored to the beam of 0.533 × 0.458 at position angle of 40°, which is the beam size of naturally-weighted resolution of 1995 data, to enhance the components.

Table 3.5: Gaussian model fitting results at 22 GHz in the northern counter-lobe.

Component	I_{peak} (Jy)	I_{tot} (Jy)	x (mas)	y (mas)	θ_{maj} (mas)	θ_{min} (mas)	p.a. (deg)
			1995 October				
CH1	0.031	0.6057	1.18	8.34	2.12	1.34	90.01
CH2	0.028	0.1424	1.35	6.99	1.17	1.06	154.87
CH3	0.0249	0.2479	-0.42	6.77	1.76	1.38	100.74
			2000 January				
CH1	0.0211	0.4294	1.94	8.74	2.61	1.11	99.23
CH2	0.0249	0.2479	1.57	7.4	1.76	1.38	100.74
CH3	0.0115	0.0513	-1.17	7.32	1.27	0.85	24.34

the component C11 (C20) as a stationary component. But, we will show the corresponding results assuming that the component C12 (C21) is stationary, as well.

As well as the hot spots, we also identified other significant components in the northern and southern lobes. This implies that the lobe contains multiple hot spots, or they are the knots of underlying jets. The apparent velocities of the components in the southern lobe and northern counter-lobe are listed in Table 3.6, and motion vectors are indicated in Figure 3.12. The errors of apparent velocity of each component are estimated to sum of gaussian fitting error and systematic error of reference position between two epochs[2]. The apparent velocity of the southern hot spot (H1) is $0.43\pm0.06c$, which is consistent with $0.34 \pm 0.09c$ that is previously estimated by Asada et al. (2006). Our measured apparent velocity of the southern hot spot yields a kinematic age of 33 ± 5 yr in 2000. This implies that the inner 10-pc-scale feature of 3C 84 is associated with the 1959 outburst. We also detected a previously undetected motion of the hot spot in the northern counter-lobe (CH1). The motion vector of the components CH1, CH2, and CH3 is not along the line between each component and the component C11 (C20). This leads to expect that the hot spot advance is not simple linear motion. Averaged advance velocity of the three components is $0.13 \pm 0.06c$ along the north direction, yielding the kinematic age of 70 ± 30 yr. This age is somewhat higher than the kinematic age derived from the southern hot spot. It might indicate that "true core" is located to the north of the component C11 (C20). There is room for arguments in this point, but, in the followings, we refer to the kinematic age derived from the advance velocity of the southern hot spot.

To emphasize that the apparent motion of both the southern and northern hot spots is not artificial, we discuss a possible registration error. Observed "radio core" is probably a jet component, and "true core" cannot be seen due to the absorption (e.g., Sudou et al. 2000). Thus a nominal reference position could have an offset between two epochs. If this is the case, positions of each component also would have a systematic offset between two epochs. However, our measured motions of the components in the southern and northern lobes are opposite direction with each other. Therefore the motion indicates actual hot spot advance, even if nominal reference position has a systematic offset between two epochs.

More clear evidence for the source expansion can be seen in Figure 3.13. This shows the surface brightness ratio between two epochs. Flux decreases in most of region of the both southern and northern lobes. As we discuss in section 3.4.5, flux decrease can be explained by synchrotron radiation loss. Also the energy loss due to the adiabatic expansion of lobe can affect the decrease of flux (Asada et al. 2006). On the other hand, the flux shows increase at the southern edge of the southern lobe and the northern edge of the northern lobe. These increases in flux are also evident in the sliced profile between two epochs (Figures 3.14 and 3.15).

3.4.2 Physical Properties in the Hot Spot and External Medium Density

We now consider the physical property of the southern hot spot of 3C 84 and the ambient medium. As we reviewed in Chapter 1, it is considered that the hot spot is generated by the impact of the jet to the ambient medium. Under the ram pressure equilibrium between the hot spot and external medium, pressure of the hot spot P_h is related to the external medium by

$$P_h = \rho_{ext} v_h^2, \tag{3.1}$$

where ρ_{ext} is the density of the external medium, v_h is the velocity of the hot spot. Assuming the minimum-energy condition in the southern hot spot of 3C 84, we obtain $P_h = 3 \times 10^{-4}$ dyn cm^{-2}.

[2]High resolution observation at 43 GHz (Dhawan et al. 1998) shows that innermost component moves with an apparent velocity of 0.055c, assuming the reference position between two epochs is C11 and C20 (The component 1 in their paper). On the other hand, our observation shows that the innermost component C12 (C22) moves 0.1c if we assume the reference position is C11 and C20. This offset of apparent velocity between our study and Dhawan et al. could be attributed to a systematic offset of the reference position between two epochs. Thus we consider 0.05c ($0.1c - 0.055c \approx 0.05c$) as the systematic error.

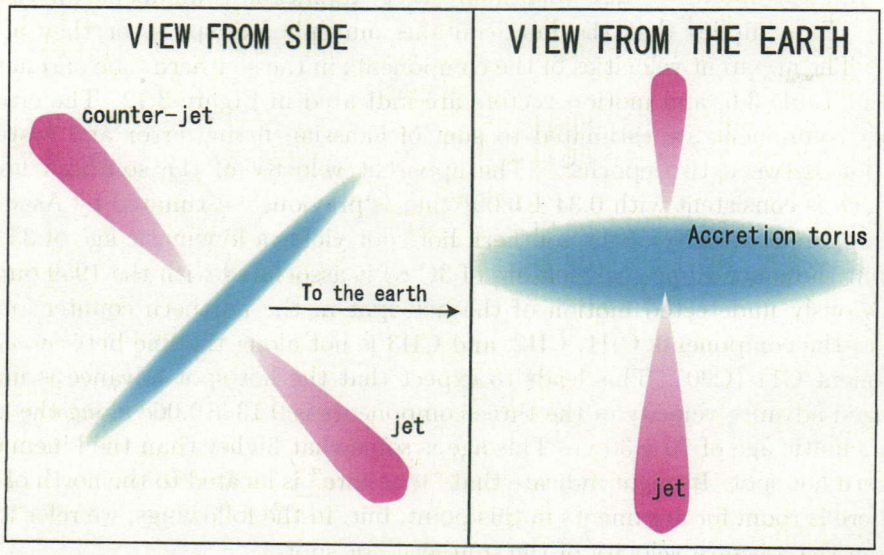

Figure 3.11: Schematic image of the geometry of 3C 84. The southern jet is approaching to the earth, and the northern one is receding. A thick accretion torus is surrounding the central engine.

Table 3.6: The apparent velocity of each component

Component	δ_x (μas)	δ_y (μas)	δ_r (μas)	v (μas/yr)	v/c
The apparent velocity relative to the component C11 (C20)					
H1	33.7±18.9	−1586.8±23.3	1587.1±30	371.8±7	0.43±0.06
H2	−444.4±28.3	−128.2±28.0	462.5±39.8	108.3±9.3	0.13±0.06
CH1	506.7±37.5	424.8±21.6	661.2±43.3	154.9 ±10.1	0.18±0.06
CH2	−30.7±33.9	420.7±36.6	421.8±49.9	98.8±11.7	0.12±0.06
CH3	−748.0±64.3	557.4±45.5	932.9±78.8	218.5±18.5	0.25±0.07
The apparent velocity relative to the component C12					
H1	168.3±19.8	−1457.8±21.5	1467.5±29.2	343.8±6.8	0.4±0.06
H2	−579.0±26.9	0.0±26.2	579.0±37.5	135.6±8.8	0.16±0.06
CH1	641.3±36.1	553.8±19.9	847.3±41.2	198.5±9.7	0.23±0.06
CH2	103.9±31.7	549.6±29.9	559.4±43.6	131.0±10.2	0.15±0.06
CH3	−870.9±62.9	686.4±43.8	1108.8±76.7	259.8±18.0	0.3±0.07

Note.— δ_x: Position difference along the R.A. between two epochs. δ_y: Position difference along the Dec. between two epochs. $\delta_r = \sqrt{\delta_x^2 + \delta_x^2}$. v: Apparent separation velocity.

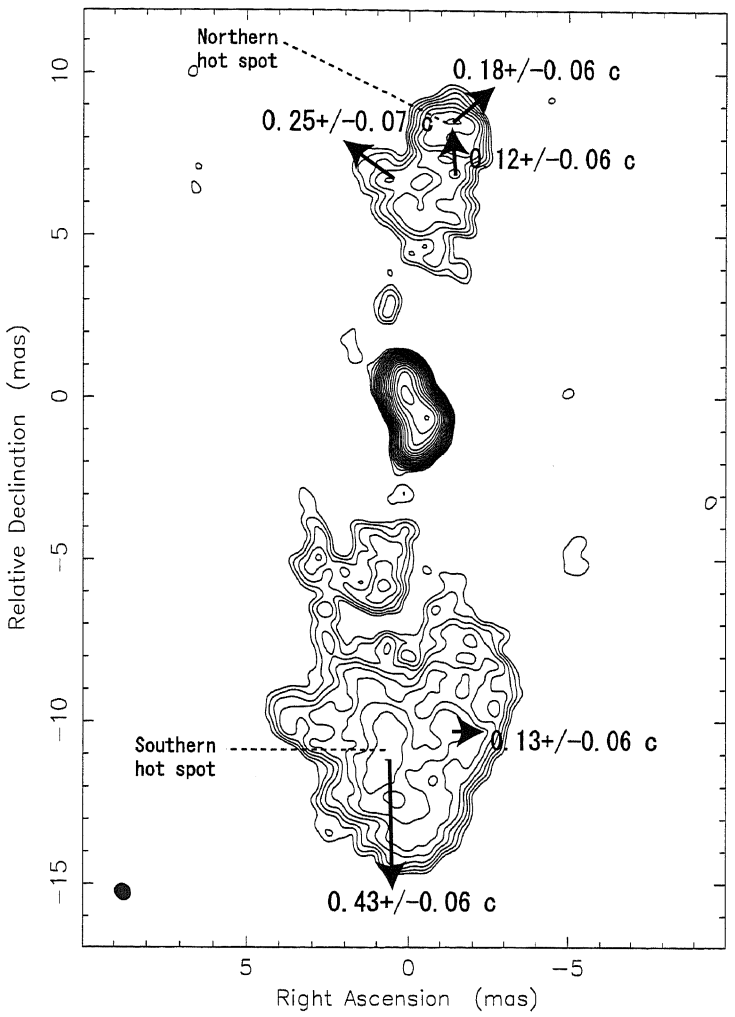

Figure 3.12: Contour plot of the 1995 observation at 22 GHz with the motion vector. Image is restored to the resolution of naturally-weighted image for the purpose of enhancement of components. The length of vector is proportional to the apparent velocity. Errors are estimated sum of the gaussian fitting error and 0.05c, which is a possible systematic error due to the misidentification of the core.

Applying the advance speed of $0.43c$ to the equation 3.1, $\rho_{ext} = 1.8 \times 10^{-24}$ g, which corresponds to the density $n = 1$ cm^{-3}. This is consistent with the average density of $n = 0.3$ cm^{-3} over the inner 2 kpc estimated by deep Chandra observations (Taylor et al. 2006).

External density is an important probe of the nature of CSOs. From the numerical simulation by de Young (1993), CSOs can be confined by external medium and unable to escape (frustration scenario) if the ratio of L_j/n is less than 10^{43} erg cm^3 s^{-1}, where L_j is total kinetic power of the jet. Total power of the hot spot must be the cumulative energy injected from the jet over the typical time scale (t) that the hot spot is formed, thus the total kinetic power of the jet is written as $L_j = P_h V_h / t^3$, where V_h is the volume of hot spot. Assuming t is the light-crossing time of the hot spot, we have $L_j \sim 10^{44}$ erg s^{-1}. Finally we obtain $L_j/n \sim 10^{44}$ erg cm^3 s^{-1}. Therefore, our measured hot-spot motion and ram pressure assumption for 3C 84 are consistent with the condition of non-frustrated source.

3.4.3 Synchrotron Break Distribution and Synchrotron Age

As reported in W2000 and A2000, the spectrum suffers from FFA in the core and the northern lobe at centimeter wavelengths. Figure 3.16 shows spectral index map between 5 GHz and 8 GHz. Spectral index is inverted in the core and northern lobe, indicating being optically thick due to FFA. In the followings, we neglect the effect of FFA in the fittings. By way of justification of this neglect, we perform the fittings only in the southern lobe.

In Figure 3.17, we show the synchrotron break frequency distribution which is obtained by the spectral fitting to observed four frequencies data. It is clearly seen that the break frequency moves to lower frequency towards the core. This tendency is consistent with the behavior of break frequency distribution of CTD 93, but more detailed spatial distribution across the lobe is revealed. The break frequency around the hot spot is very high, leaving a simple power law over the observed frequency range. High surface brightness region on the image of break frequency around the hot spot shows asymmetric feature. This will be discussed in section 3.4.4. Northernmost region in the lobe probably suffers FFA at lower frequencies, yielding apparent high-break frequency.

Figure 3.18 shows the sliced profile of the break frequency and total intensity at 22 GHz going from the hot spot to the core. The flux decreases steeply with increasing the distance from the hot spot within first 4 mas. The flux density at ~ 3 mas from the hot spot is about one order of magnitude smaller than that at hot spot. With this decrease in flux, the break frequency also shows a sharp drop with increasing the distance from the hot spot. On the other hand, the break frequency decreases much gradually in the lobe area. This might indicate that the expansion loss is significant in the vicinity of the hot spot, as discussed in section 3.19.

The lowest break frequency in the lobe is 2.3±1.4 GHz. It occurs at the northernmost area of the east edge in the lobe. This break frequency gives an age as a function of the magnetic field strength B, $t = 2.31 \times 10^4 B^{-3/2}$. Similar to Chapter 2, we consider the magnetic field strength in minimum-energy condition (see Appendix A). To estimate typical magnetic field strength in the lobe, we chose the components A, B, and C (see Figure 3.17). Minimum-energy field and other physical parameters of these three components are listed in Table 3.9. Averaged magnetic field of the three components is 95.5 mG, and resultant synchrotron age is 24^{+14}_{-5} yr in 1995. The synchrotron age shows good agreement with the kinematic age estimated in section 3.4.1. Also our estimated synchrotron age indicates that the lobe of inner 10-pc scale is formed by the 1959 outburst.

As discussed in Chapter 2, the synchrotron age estimated above could be underestimated than actual source age if there is a large back flow. However, multiepoch VSOP observation found no significant back-flowing component (Asada et al. 2006). Therefore we feel reasonable about the neglect of the effect of back flow.

[3]We assumed that the contribution to the kinetic power from the thermal particles is negligible comparing to the non-thermal ones.

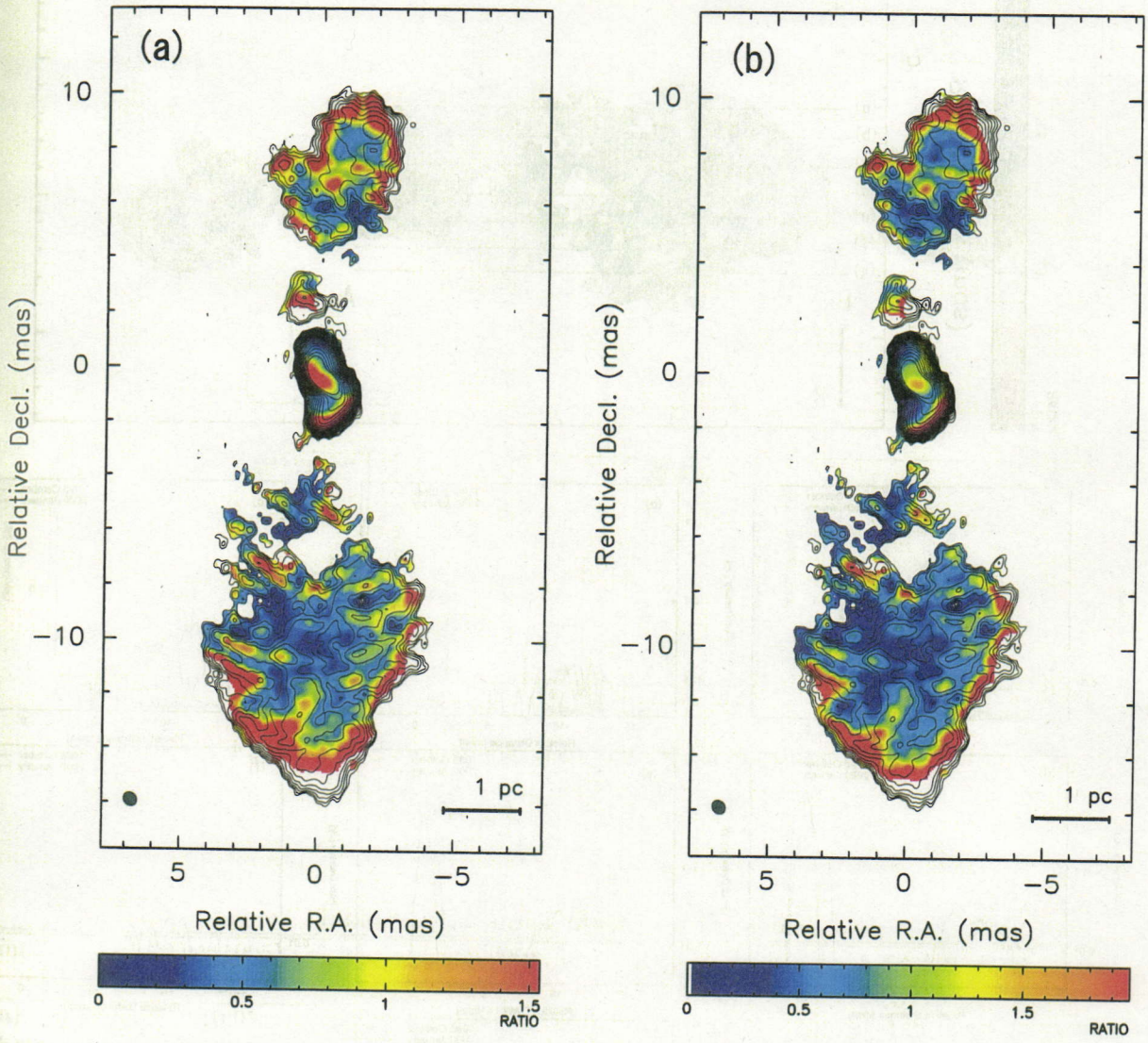

Figure 3.13: The brightness ratio between the first and second epochs, superposed on the contour of total intensity in 2000. The contours are restored to the beam size of 0.533×0.458 at the position angle of 40°. The reference position between two epochs is settled C11 (C20) for (a) and C12 (C21) for (b). Contour shows the total intensity of 2000 observatoin, color shows the brightness ratio between 1995 and 2000 observations. The brightness ratio is shown where the flux density is greater than 3.33 mJy which is a 3 times image noise r.m.s. of the first epoch image.

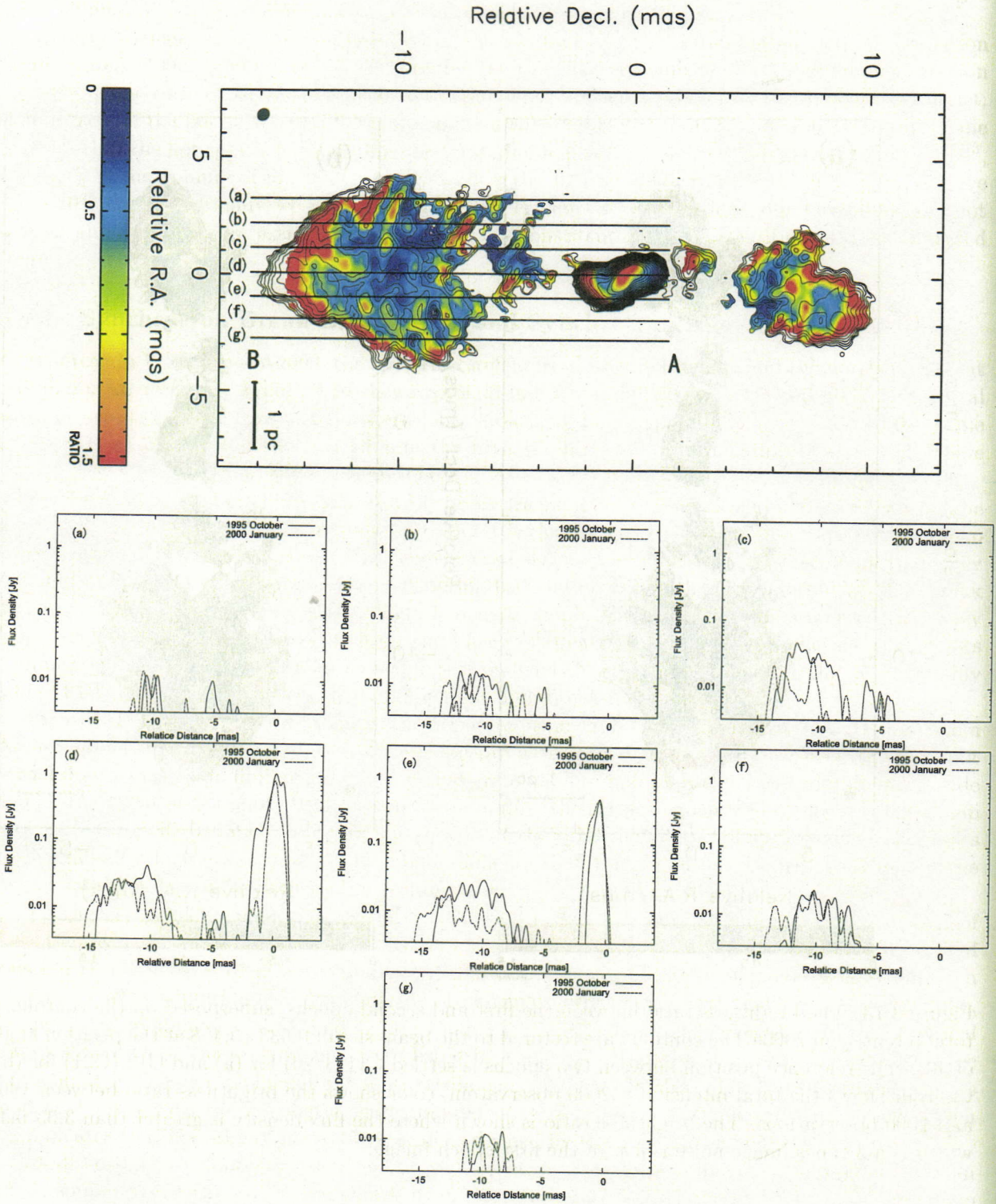

Figure 3.14: The intensity profiles sliced across the several areas of the southern lobe as shown in the top image, which is the same as Fig 3.13(a).

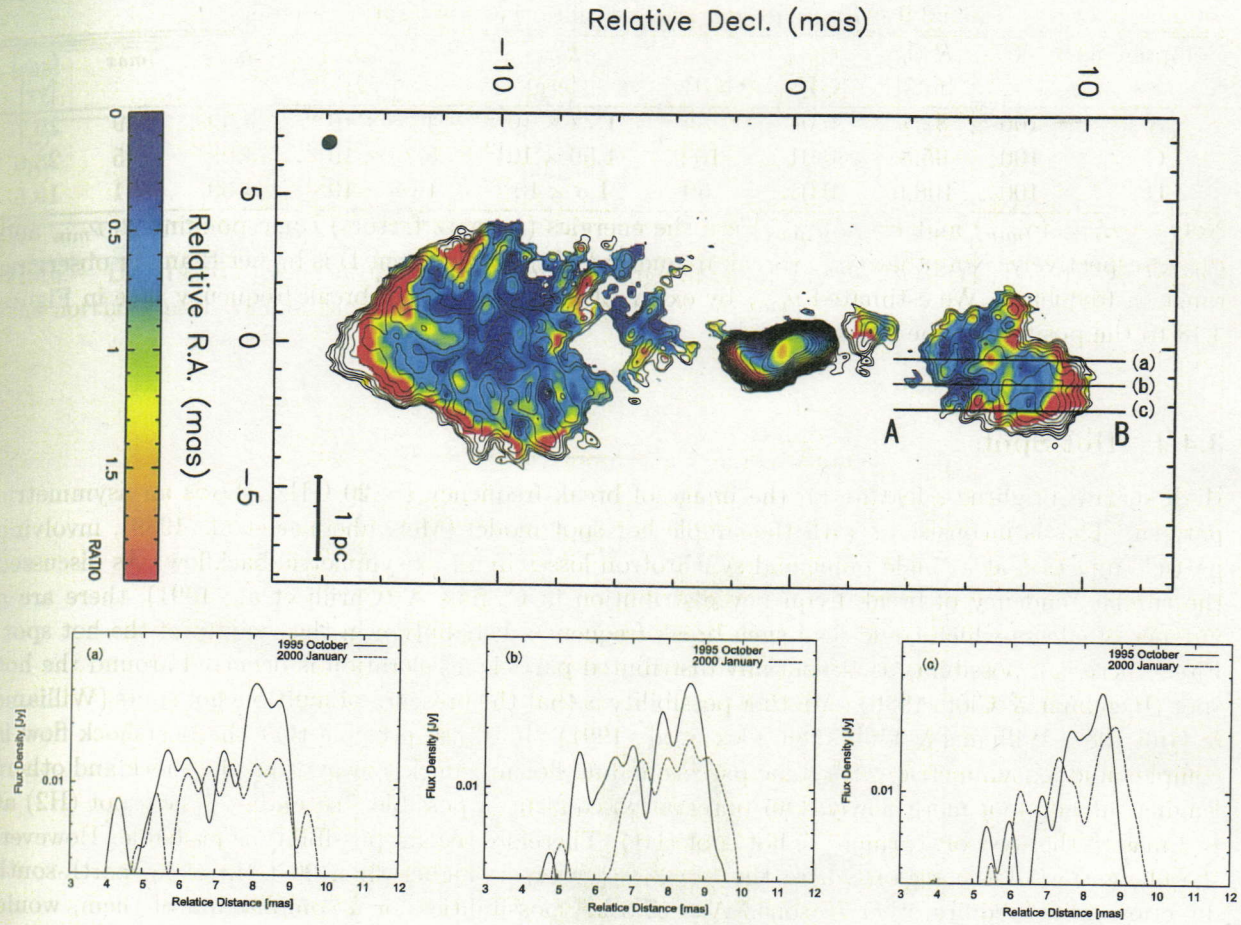

Figure 3.15: Same as Fig. 3.14, but for the northern lobe.

Table 3.7: Expansion of the southern lobe

Line	Dec(1995) (mas)	Dec(2000) (mas)	δ (mas)	δ (lyr)	v/c
(a)	-10.95	-12.06	-1.11	-1.29	-0.3
(b)	-12.95	-13.75	-0.79	-0.92	-0.22
(c)	-13.82	-14.34	-0.52	-0.60	-0.14
(d)	-14.47	-15.44	-0.97	-1.12	-0.26
(e)	-14.06	-15.61	-1.55	-1.81	-0.42
(f)	-12.92	-14.2	-1.28	-1.49	-0.35
(g)	-10.75	-11.47	-0.73	-0.84	-0.2
	average		-1.63	-1.89	-0.27

Note.— Dec(1995): Position of the southernmost edge of radio lobe in 1995. Dec(2000): Position of the southernmost edge of radio lobe in 2000. δ: Position difference between columns 2 and 3. v/c: Expansion rate.

Table 3.9: Minimum-energy field and other physical parameters.

Component	k	B_{min} [mG]	ν_{min} [GHz]	ν_{max} [GHz]	E_{min} [erg]	E_{max} [erg]	γ_{min}	γ_{max}	t_{syn} [yr]
A	100	82.1	0.01	7.7	1.72×10^{12}	4.78×10^{13}	5.39	149	29.7
C	100	95.8	0.01	10.9	1.59×10^{12}	5.26×10^{13}	4.99	165	23.6
D	100	108.6	0.01	50	1.5×10^{12}	1.06×10^{14}	4.69	331	19.5

Note.— E_{min} (γ_{min}) and E_{max} (γ_{max}) are the energies (Lorentz factors) corresponding to ν_{min} and ν_{max}, respectively. Note that ν_{max} (break frequency) of the component D is higher than our observing range in frequency. We estimated ν_{max} by extrapolating the slope of break-frequency slice in Figure 3.18 to the position of the hot spot.

3.4.4 Hot Spots

High surface brightness feature on the image of break frequency (> 20 GHz) shows an asymmetric pattern. This is inconsistent with the simple hot spot model (Meisenheimer et al. 1989), involving particle injection at a single point and synchrotron losses in an axisymmetric backflow. As discussed the similar tendency of break frequency distribution in Cygnus A (Carilli et al. 1991), there are a number of effects which could lead such break frequency distribution in the vicinity of the hot spot. First, there is a possibility that spatially distributed particle acceleration is occurred around the hot spot (Begelman & Cioffi 1989). Another possibility is that the presence of multiple hot spots (Williams & Gull 1984; Williams & Gull 1985; Cox et al. 1991). It is also possible that the postshock flow is complex and axisymmetric, with some parcels of fluid flowing quickly away from the shock and others leaving the hot spot more slowly. Our observation confirms a possible "secondary" hot spot (H2) at $\sim$ 3 mas to the west of "primary" hot spot (H1). Therefore second possibility is probable. However, the elongation of the region where the break frequency is higher than 20 GHz along north-south direction would require other reasons. Any of other possibilities, or a combination of them, would result in observed break frequency distribution around the hot spot. In any cases, simple axisymmetric backflow from the hot spot may be too simple in the hot spot vicinity.

3.4.5 Expansion Loss

As shown in Figure 3.18, the break frequency shows a drop, which coincides with a steep decrease of brightness, going from the hot spot to the north direction. Figure 3.19 shows spectral shape at 5 positions in the southern lobe. The solid lines are the simple connection of the data between adjacent frequencies. The spectrum labeled 1 corresponds to the hot spot spectrum, and the spectra labeled 2-5 correspond to the spectra where the position along the line between the hot spot and the core, with each position separated by 30 pixels (1 pixel=0.07 mas). The positions 1-5 are shown in Figure 3.18(a).

A large drop in the flux density at all four frequencies is seen between position 1 and position 2. The drops in the flux density almost equally at all frequencies, and simple scaling can be applied between two spectra. This simple scaling law implies that the dominant factor of electron energy losses is the expansion loss. On the other hand, going from the position 2 to the position 5, the flux density at 5 GHz does not show large variation but differs only at frequencies higher than 8 GHz. Such spectral change implies that the synchrotron radiation loss is dominant. These changes of spectrum indicate that the expansion loss is effective only in the vicinity of the hot spot and the synchrotron aging become dominant in the radio lobe.

Table 3.8: Expansion of the northern lobe

Line	Dec(1995) (mas)	Dec(2000) (mas)	δ (mas)	δ (lyr)	v/c
(a)	9.19	9.81	0.62	0.73	0.17
(b)	9.59	9.95	0.37	0.43	0.10
(c)	9.24	9.78	0.53	0.62	0.15
	average		0.36	0.42	0.14

Note.— Dec(1995): Position of the northernmost edge of radio lobe in 1995. Dec(2000): Position of the northernmost edge of radio lobe in 2000.

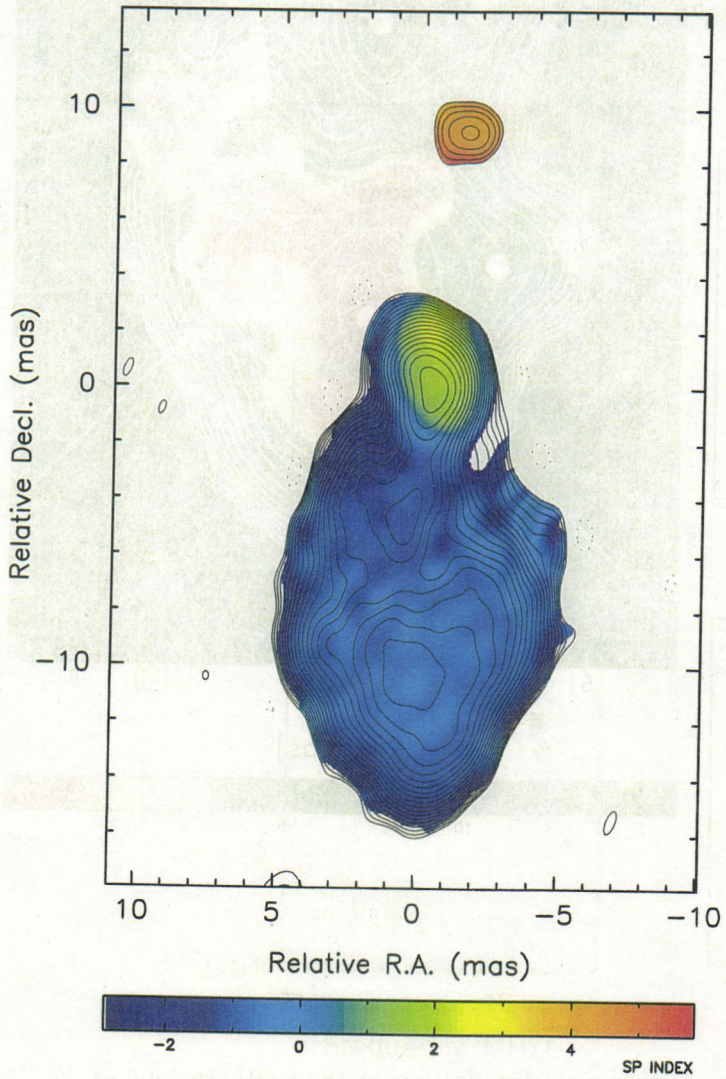

Figure 3.16: Spectral index map between 4.99 and 8.421 GHz, superimposed on the total intensity at 4.99 GHz. The core and northern lobe shows inverted spectrum, indicating strong absorption.

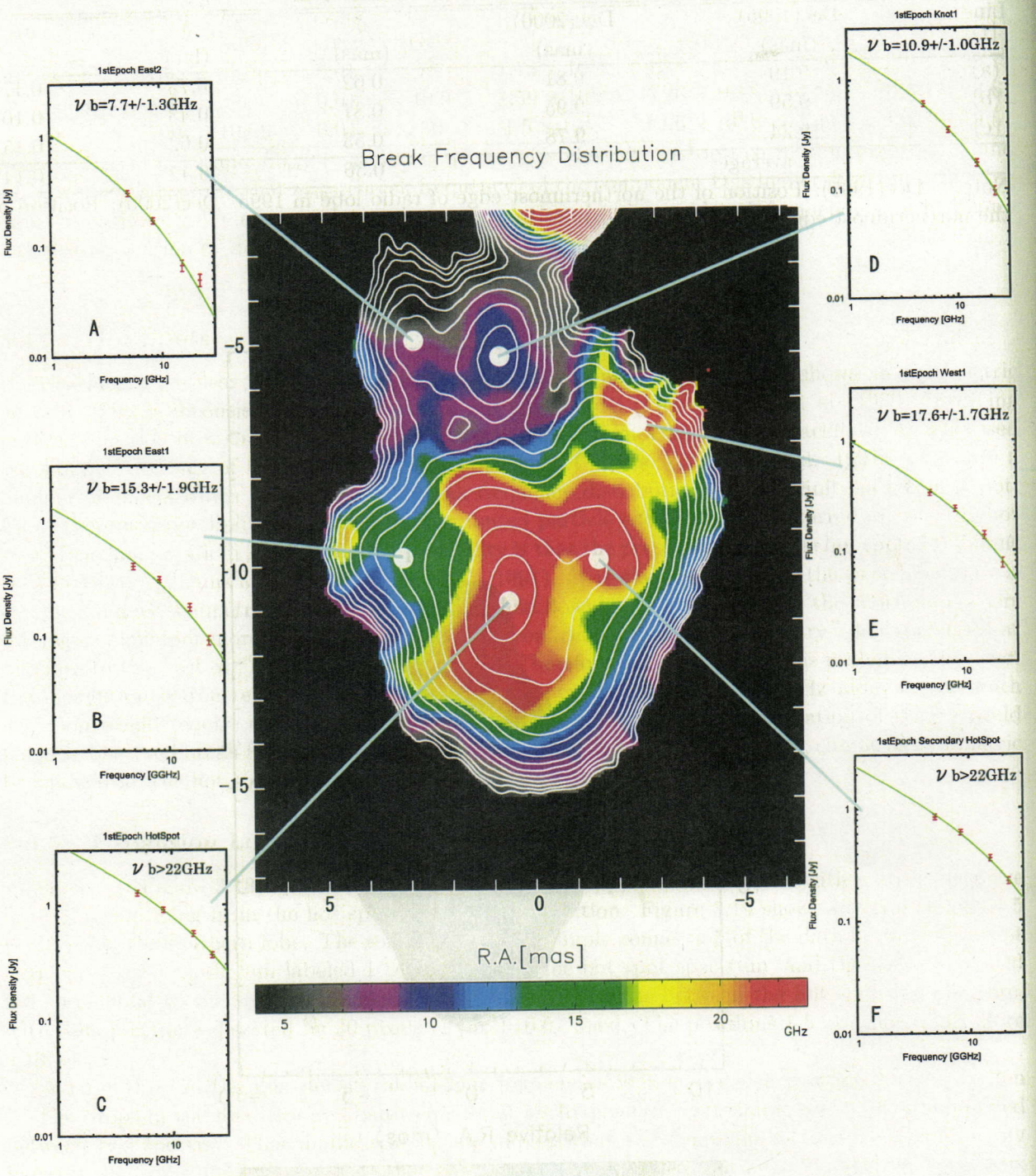

Figure 3.17: The break frequency distribution in the southern lobe of 3C 84. Inserted graphs are observed flux densities and best fit spectra at each example point indicated by the white small circle.

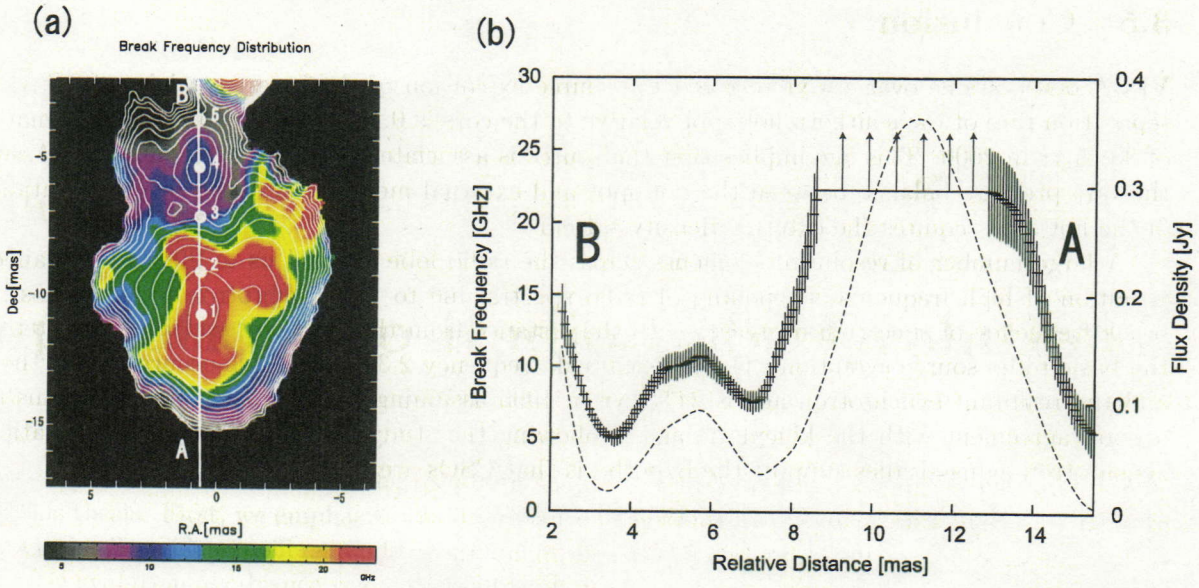

Figure 3.18: (a) Same image as Fig. 3.17. (b) Sliced profile of the break frequency of the southern lobe from north to south direction, which is indicated by a white line in (a). The solid line shows the break frequency distribution. The dashed line shows the total intensity at 22 GHz. The arrows indicate lower limits.

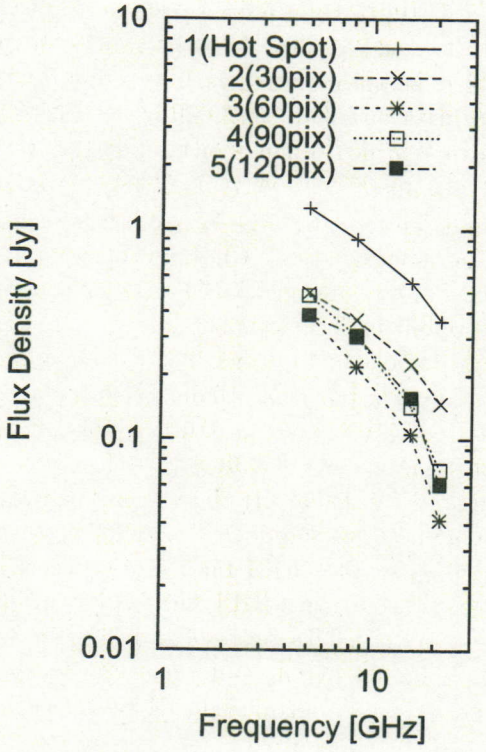

Figure 3.19: Spectral data at five positions along the south-north line indicated in Figure 3.18(a). The solid lines are linear connection of the data between adjacent frequencies.

3.5 Conclusion

VLBA observations over 4.5 yr revealed the source expansion of the innermost lobe of 3C 84. The separation rate of the southern hot spot relative to the core is $0.43\pm0.06c$, yielding the kinematic age of 33 ± 5 yr in 2000. This age implies that the source is associated with the 1959 outburst. Assuming the ram pressure balance between the hot spot and external medium, our measured separation rate of the hot spot requires the external density ≈ 1 cm^{-3}.

A large number of resolution elements across the radio lobe allowed us to illustrate detailed distribution of high frequency steepening of radio spectra due to the synchrotron radiation loss. The break frequency of spectrum decreases with the distance from the hot spot, which is consistent with the basic radio source evolution. The lowest break frequency 2.3 ± 1.4 GHz is occurred near the core, and the resultant synchrotron age is 24^{+14}_{-5} yr in 1995 assuming minimum-energy field. This shows a good agreement with the kinematic age. Following the study for CTD 93, both kinematic- and synchrotron-aging studies support the hypothesis that CSOs are young radio sources.

Chapter 4

Implications to Radio Lobe Evolution

In this chapter we will summarize the results in chapter 2 and 3, and give comprehensive discussions about this thesis. First, we emphasize the importance of agreements of synchrotron age and kinematic age in CSOs. Second, we will expand the argument into MSOs and FRII sources, and give an implication to the evolution of advance velocity of hot spot. Finally, we will present physical quantities of hot spot versus the hot spot distance from the core for a large number of sources, and discuss indications for the evolutional sequence from CSOs to MSOs to FRII sources.

4.1 Agreement of Synchrotron Age and Kinematic Age

Over decades, spectral variation across the radio lobes for radio galaxies has been studied (Burch 1979; Winter et al. 1980; Alexander & Leahy 1987; Carilli et al. 1991; Liu et al. 1992; Klein et al. 1995; Mack et al. 1998; Parma et al. 1999; Jamrozy et al. 2005). These studies yielded synchrotron ages of $\sim 10^6$-10^8 yr. However, we should notice that synchrotron-aging study contains larger uncertainties than kinematic-aging study. One of the difficulties with the estimation of synchrotron age is the estimation of magnetic field strength. Since the synchrotron age strongly depends on the magnetic field strength rather than break frequency ($t \propto B^{-3/2}\nu_B^{-1/2}$), uncertainty of magnetic field makes it difficult to estimate accurate source age. Most of synchrotron-aging studies have assumed minimum-energy field for lack of better estimation, though it is not clear whether the minimum-energy condition is appropriate. Thus the comparison between kinematic age and synchrotron age for identical sources is crucial test for synchrotron aging theory. CSOs are excellent laboratory for testing the synchrotron aging theory because they are only sources that hot spot motions have been detected.

Our study showed the agreements of kinematic age and synchrotron age within a factor of two. This agreements requires $0.6B_{min} \lesssim B \lesssim 1.6B_{min}$, where B_{min} is the minimum-energy field. We proved that the magnetic field of radio lobe of CSOs is not so far from the minimum-energy field for at least two sources. It is now open to question: Is the synchrotron aging theory under the minimum-energy assumption valid for all radio galaxies? Comparison of kinematic age and synchrotron age not only for other CSOs but also for MSOs, and FRII sources is required to answer this question. However, kinematic-aging study for MSOs and FRII sources is technically challenging. There have not been many results that the hot spot of MSOs and FRII sources is detected by VLBI observation. This is probably due to lack of sensitivity enough to detect diffuse hot spot, field of view, and so on. Recent phase referencing technique for VLBI observation can make it possible to measure hot spot motion for MSOs and FRII sources.

Finally, we again emphasize that our study is the first attempt to prove the agreement of kinematic age and synchrotron age. At the same time, this indicates that the minimum-energy condition is applicable to CSOs.

4.2 Expansion Rate of Radio Lobes

As we addressed previous section, agreements of kinematic age and synchrotron age in two CSOs indicate the validity of synchrotron aging theory under the minimum-energy assumption. Here we expand this argument to MSOs and FRII sources, and will discuss the expansion rate of radio lobes.

First of all, we assume that synchrotron age of FRII sources corresponds to the exact source age and allows hypothesis that CSOs evolve into FRII sources through MSOs. Former assumption requires that the minimum-energy field is adequate in the radio lobes of MSOs and FRII sources. There is room for further investigation on this point, but supporting evidence is reported by Kataoka & Stawarz (2005). They examined radio and X-ray spectra for more than 40 radio galaxies. The X-ray spectra of radio lobes and hot spots in most of radio galaxies are well-fitted by synchrotron-self Compton or external Compton on cosmic microwave background photons under the minimum-energy field. On the other hand, Isobe et al. (2005), similar to the study by Kataoka & Stawarz (2005), reported that magnetic field is typically $B \simeq 0.5 B_{\rm min}$. If this is the case, synchrotron age estimated under the minimum-energy field becomes about three times older than the exact source age. Either case, however, does not lead significant difference in the following discussions.

Figure 4.1 shows the radio source age (t) with respect to the size of radio source (l). The source size is defined by the extent between the hot spot and the counter hot spot. The relationship between age and size constraints the separation velocity between the hot spot and the counter hot spot [1]. The solid line in Figure 4.1 indicates a simple linear fit on the log-log plane. We obtained a best-fit linear line

$$\log\left(\frac{t}{[\rm yr]}\right) = (1.08 \pm 0.05) \log\left(\frac{l}{[\rm pc]}\right) + (1.45 \pm 0.23), \tag{4.1}$$

or $t = 10^{(1.45\pm0.23)} l^{(1.08\pm0.05)}$. We note that the relationship between the size and age is almost linear, and the slope of the linear fit implies the separation velocity of $0.12c$. Assuming the equal speed between hot spot and the counter hot spot, the advance velocity of the hot spot relative to the core is $0.06c$.

Note, however, that it is possible that the age of FRII sources is underestimated due to lack of sensitivity and frequency range not enough to detect the "lowest" break frequency in the lobe. To avoid such bias, we estimated advance velocity of hot spot by the linear fit to observed synchrotron age distribution across the lobe, which is the same method that we obtained the advance velocity of CTD 93 (see Chapter 2). The resultant advance velocity of FRII sources is listed in Table 4.1 and also indicated in Figure 4.2, together with the advance velocity of CSOs. Both CSOs and FRII sources distributes within $0.2c$ except 3C 84, and the averaged velocities of CSOs and FRII sources are $0.1c$ and $0.05c$, respectively. There are no CSOs whose velocity is less than $0.05c$.

In Figure 4.3 we show the apparent velocity of hot spot to see the detection limit of hot spot motion. Apparent velocity of less than ~ 10 μas/yr has not been detected. This is probably due to lack of the angular resolution. Apparent velocity of 10 μas/yr corresponds to $\sim 0.05c$ in $z > 0.1$. Thus apparent absence of low velocity ($< 0.05c$) CSOs is due to biases introduced by the detection limits.

In order to compare the velocities between CSOs and FRII sources statistically, we performed the Kolomogorov-Smirnov test (KS-test; see Appendix). The resultant probability for KS-test statistics D to exceed the observed value is 30%. As noted above, the velocity distribution of CSOs is biased toward higher velocity. If the detection limit of advance velocity would be better, the probability for KS-test statistics is expected to be higher. It is so far possible to conclude that the advance velocity of hot spot of all radio galaxies is not significantly different between CSOs and FRII sources.

[1] Concerning hot spot, radio observations for radio galaxies show us that hot spots always reside at the tip of jets. It is therefore naturally interpreted that the separation velocity between hot spots is the expansion velocity of radio source, so hereafter we use the separation velocity of hot spots as a synonym for the expansion velocity of radio source.

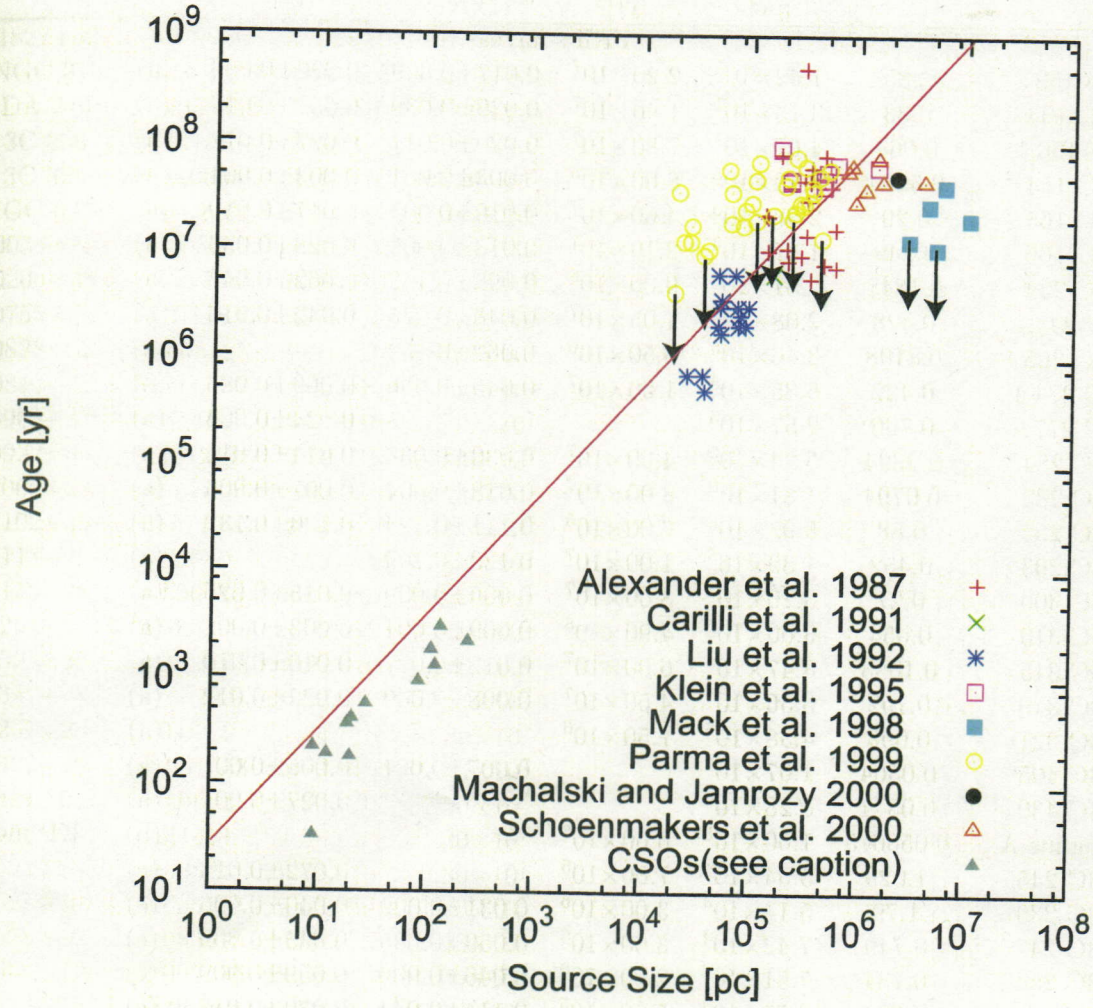

Figure 4.1: Age-Size relation of radio sources. Age of FRII sources is estimated by synchrotron aging while that of CSOs is estimated by kinematic aging. The reference of each source is tabulated in the bottom right corner of the figure. The data points with arrows indicate upper limit. Note that the synchrotron age of FRII sources is estimated from the lowest break frequency in the observing frequency range. Since observing range in frequency of each source are not same, observations with higher frequency range could result higher "lowest break frequency." Such observations could bias the estimated synchrotron age to lower value than exact age. Spectral-fitting method, KP model or JP model, differs by authors (see Table 4.1). This difference slightly affects the age estimation. The sample of CSOs is obtained from Polatidis & Conway 2003, Owsianik et al. 1998, Owsianik & Conway 1998, Taylor et al. 2000, Marecki et al. 2003, Stanghellini et al. 2002, Tschager et al. 2000, and this thesis. The solid line indicates the best-fit linear line on the log-log plane.

Table 4.1: Source size, age, and advance velocity of FRII and CSOs.

Source	redshift	Size[1] [pc]	Age[2] [yr]	Va[3] [v/c]	Vb[3] [v/c]	ref.[4]	note[5]
			FRII sources				
3C 52	0.2854	1.32×10^5	2.20×10^7	0.017±0.009	0.020±0.006	(a)	
3C 103	0.33	3.13×10^5	1.40×10^7	0.039±0.039	0.052±0.017	(a)	
3C 136.1	0.064	4.67×10^5	7.80×10^7	0.020±0.011	0.027±0.011	(a)	
3C 154	0.5804	2.13×10^5	8.00×10^6	0.003±0.001	0.003±0.001	(a)	
3C 165	0.29	2.98×10^5	4.60×10^7	0.010±0.004	0.017±0.010	(a)	
3C 166	0.249	1.37×10^5	2.10×10^7	0.013±0.005	0.029±0.006	(a)	
2C 234	0.1848	2.81×10^5	9.00×10^6	0.092±0.122	0.062±0.043	(a)	
3C 244.1	0.428	2.08×10^5	1.05×10^7	0.048±0.026	0.042±0.016	(a)	
3C 265	0.8108	3.46×10^5	5.50×10^6	0.062±0.132		(a)	
3C 274.1	0.422	5.85×10^5	1.60×10^7	0.045±0.006	0.069±0.085	(a)	
3C 277.2	0.766	2.57×10^5			0.024±0.008	(a)	
3C 284	0.2394	5.24×10^5	4.00×10^7	0.030±0.035	0.014±0.015	(a)	
3C 285	0.0794	1.81×10^5	8.00×10^7	0.018±0.004	0.007±0.005	(a)	
2C 292	0.88	5.92×10^5	7.00×10^6	0.111±0.124	0.120±0.132	(a)	
3C 293	0.452	1.39×10^5	1.00×10^7	0.123±0.209		(a)	
3C 300	0.27	3.20×10^5	3.00×10^7	0.006±0.009	0.015±0.026	(a)	
3C 310	0.054	3.00×10^5	4.90×10^8	0.009±0.001	0.003±0.001	(a)	
3C 315	0.1083	3.47×10^5	6.00×10^7	0.012±0.027	0.010±0.010	(a)	
3C 319	0.192	3.36×10^5	4.50×10^7	0.008±0.009	0.022±0.012	(a)	
3C 321	0.096	4.58×10^5	7.50×10^6			(a)	
3C 405	0.0564	1.07×10^5		0.007±0.001	0.006±0.001	(a)	
3C 430	0.0541	8.28×10^4			0.027±0.007	(a)	
Cygnus A	0.056075	1.60×10^5	6.00×10^6			(b)	KP model
3C 245	1.029	3.54×10^4	7.00×10^5		0.072±0.016	(c)	
3C 239	1.79	5.14×10^4	3.00×10^6	0.031±0.009	0.040±0.006	(c)	
3C 247	0.749	7.42×10^4	3.00×10^6	0.059±0.005	0.045±0.009	(c)	
3C 254	0.734	7.51×10^4	2.00×10^6	0.046±0.009	0.059±0.009	(c)	
3C 263.1	0.824	3.72×10^4	5.00×10^5	0.114±0.044	0.079±0.018	(c)	
3C 266	1.275	2.53×10^4	7.00×10^5	0.059±0.015	0.073±0.015	(c)	
3C 268.4	1.4	4.89×10^4	2.00×10^6	0.084±0.014	0.053±0.011	(c)	
3C 270.1	1.519	5.21×10^4	1.70×10^6	0.061±0.010	0.051±0.010	(c)	
3C 275.1	0.557	9.36×10^4	3.00×10^6	0.050±0.010	0.054±0.015	(c)	
3C 280	0.996	7.86×10^4	2.50×10^6	0.049±0.008	0.053±0.008	(c)	
3C 288	0.246	7.06×10^4	6.00×10^6	0.029±0.006	0.035±0.012	(c)	
3C 289	0.967	5.28×10^4	3.50×10^6	0.041±0.008	0.037±0.008	(c)	
3C 294	1.779	8.78×10^4	2.00×10^6	0.044±0.009	0.056±0.009	(c)	
3C 299	0.367	4.93×10^4	6.00×10^6	0.115±0.027	0.016±0.005	(c)	
0136+39	0.2107	1.46×10^6	6.20×10^7			(d)	KP model
0204+29	0.109	4.56×10^5	4.10×10^7			(d)	KP model
0326+39	0.0243	2.24×10^5	4.50×10^7	0.012		(d)	KP model
0836+29	0.079	6.09×10^5	6.50×10^7	0.005		(d)	KP model
1243+26	0.0891	4.82×10^5	5.50×10^7			(d)	KP model
1321+31	0.0161	2.23×10^5	4.70×10^7			(d)	KP model
1615+35	0.0296	1.82×10^5	9.00×10^7	0.001		(d)	KP model

Table 4.1: Source size, age, and advance velocity of FRII and CSOs.

Source	redshift	Size[1] [pc]	Age[2] [yr]	Va[3] [v/c]	Vb[3] [v/c]	ref.[4]	note[5]
1827+32	0.0659	4.52×10^5	4.70×10^7			(d)	KP model
NGC 315	0.014093	2.90×10^6	1.25×10^7			(e)	upper limit
DA 240	0.035661	5.26×10^6	1.06×10^7			(e)	upper limit
3C 236	0.1005	1.05×10^7	2.03×10^7			(e)	
3C 326	0.0895	4.38×10^6	2.70×10^7			(e)	
NGC 6251	0.02471	6.17×10^6	4.10×10^7			(e)	
0034+25	0.03294	1.13×10^5	6.70×10^7			(f)	
0206+35	0.03737	6.35×10^4	3.50×10^7			(f)	
0755+37	0.042836	1.06×10^5	1.90×10^7			(f)	upper limit
0828+32	0.05125	2.94×10^5	2.70×10^7			(f)	upper limit
0844+31	0.06737	3.52×10^5	4.00×10^7			(f)	
0908+37	0.104	8.51×10^4	2.40×10^7			(f)	
0922+36	0.112118	3.59×10^5	3.60×10^7			(f)	
1005+28	0.147869	5.04×10^5	5.80×10^7			(f)	
1102+30	0.071662	2.11×10^5	4.90×10^7			(f)	
1113+29	0.049	8.17×10^4	1.70×10^7			(f)	
1116+28	0.06718	3.03×10^5	6.20×10^7			(f)	
1254+27	0.021558	2.05×10^4	3.50×10^7			(f)	
1322+36	0.018763	1.92×10^4	4.00×10^6			(f)	upper limit
1347+28	0.0724	6.33×10^4	1.80×10^7			(f)	
1357+28	0.0629	1.54×10^5	2.20×10^7			(f)	upper limit
1422+26	0.037553	9.73×10^4	2.80×10^7			(f)	
1441+26	0.0621	2.52×10^5	7.50×10^7			(f)	
1455+28	0.1411	4.38×10^5	1.30×10^7			(f)	upper limit
1521+28	0.0825	2.75×10^5	2.80×10^7			(f)	
1525+29	0.065155	2.65×10^4	1.20×10^7			(f)	
1528+29	0.083918	3.32×10^5	2.90×10^7			(f)	
1609+31	0.095096	3.89×10^4	1.00×10^7			(f)	
1613+27	0.06463	3.58×10^4	9.00×10^6			(f)	upper limit
1615+32	0.151019	2.00×10^5	4.10×10^7			(f)	
1621+38	0.030988	2.31×10^4	1.20×10^7			(f)	
1626+39	0.030354	5.98×10^4	5.70×10^7			(f)	KP model
1643+27	0.101845	2.32×10^5	2.00×10^7			(f)	
1658+30	0.034424	1.06×10^5	4.60×10^7			(f)	
1726+31	0.166148	2.44×10^5	2.30×10^7			(f)	
1827+32	0.065012	4.13×10^5	5.00×10^7			(f)	
2236+35	0.027366	2.72×10^4	1.70×10^7			(f)	
0109+492	0.067	7.64×10^5	5.50×10^7	0.031±0.001	0.023±0.001	(g)	
0813+758	0.2324	1.60×10^6	4.40×10^7	0.076±0.001	0.049±0.001	(g)	
1003+351	0.0989	3.96×10^6	4.50×10^7	0.120±0.001		(g)	
1209+745	0.107	8.33×10^5	6.20×10^7	0.026±0.001	0.019±0.001	(g)	
1312+698	0.106	9.03×10^5	2.80×10^7	0.073±0.001	0.038±0.001	(g)	
1543+845	0.201	1.46×10^6	7.30×10^7	0.038±0.001	0.034±0.001	(g)	
2043+749	0.104	1.11×10^6	3.70×10^7	0.047±0.001	0.049±0.001	(g)	
J 1343+3758	0.229	2.18×10^6	5.00×10^7	0.112±0.030	0.085±0.038	(h)	

Table 4.1: Source size, age, and advance velocity of FRII and CSOs.

Source	redshift	Size[1] [pc]	Age[2] [yr]	Va[3] [v/c]	Vb[3] [v/c]	ref.[4]	note[5]
			CSOs				
0035+227	0.096	28.3	5.67×10^2	0.081±0.039		(i)	
0108+388	0.699	21.0	4.17×10^2	0.082±0.005		(j)	
0710+439	0.518	87.7	9.32×10^2	0.153±0.01		(k)	
1031+567	0.4597	1.13×10^2	1.84×10^3	0.099±0.036		(l)	
1245+676	0.1071	12.3	1.90×10^2	0.106±0.006		(m)	
1843+356	0.763	20.3	1.80×10^2	0.184±0.018		(n)	
1943+546	0.263	1.25×10^2	1.31×10^3	0.156±0.023		(i)	
2021+614	0.227	19.2	3.68×10^2	0.085±0.012		(o)	
2352+495	0.238	1.39×10^2	3.00×10^3	0.075±0.018		(i)	
OQ 208	0.0766	9.20	2.24×10^2	0.067±0.02		(n)	
CTD 93	0.473	2.50×10^2	2.20×10^3	0.170±0.06		(p)	
3C 84	0.0176	9.30	33.0	0.430±0.06		(p)	

Note.— [1]Overall size of radio source. If the size is not written in original literature, we estimated the size from hotspot-to-hotspot by eye. [2]Synchrotron age for FRII sources while kinematic age for CSOs. Alexander et al. (1987) have not specified the age, we read off the age from figure 3 in their literature. [3]Va and Vb are advance velocities of the hotspot and the counter hot spot, respectively. Advance velocity is calculated as a half of the separation velocity for CSOs that have been detected only a hot spot advance relative to the other hot spot. For FRII sources, the advance velocity was estimated by the linear fit to the synchrotron age distribution. [4]References: (a) Alexander et al. 1987, (b) Carilli et al. 1991, (c) Liu et al. 1992, (d) Klein et al. 1995, (e) Mack et al. 1998, (f) Parma et al. 1999, (g) Schoenmakers et al. 2000, (h) Jamrozy et al. 2005, (i) Conway & Polatidis 2003, (j) Owsianik et al. 1998, (k) Owsianik & Conway 1998, (l) Taylor et al. 2000, (m) Marecki et al. 2003, (n) Stanghellini et al. 2002, (o) Tschager et al. 2000, (p) This thesis. [5]Sources noted KP model in column 8 are estimated their age by KP model. Other sources are estimted by JP model. "upper limit" denotes upper limit of source age.

4.3 Evolution of Physical Parameter of Hot Spot

Assuming that the minimum-energy assumption is valid in the radio lobe of FRII sources, we find that CSOs are at least three times younger than FRII sources. However, we still do not know whether CSOs evolve into FRII sources. In this section, we investigate the relation of CSOs, MSOs, and FRII sources from the physical parameters of hot spot.

We compiled various-sized radio galaxies and examined physical parameters of hot spot (Table 4.3). FRII sources ($l \gtrsim 10$ kpc, where l is linear size of radio source) in our sample are selected from FRII radio galaxies in 3CR catalogue (Hardcastle et al. 1998; Fernini et al. 1993; Bridle et al. 1994; Gilbert et al. 2004). We excluded QSOs from our sample because hot spot parameters are possible to be affected by relativistic effect. However, some QSOs having relatively symmetric radio lobes are not this case (e.g., 3C 175). MSOs ($1 \lesssim l \lesssim 10$ kpc) are selected from MSO sample in Dallacasa et al. (2002a and 2002b), CSS sources having double-lobe-like structure in Fanti et al. (1985) and Sanghera et al. (1995). CSOs are selected from CSO sample in Readhead et al. (1996), Taylor et al. (2000), Manness et al. (2004), Wang et al. 2003, Polatidis et al. 1995, and this thesis. From this data, we investigate how the physical parameter changes with the distance from the core, and compare the data with the dynamical evolution model of hot spot.

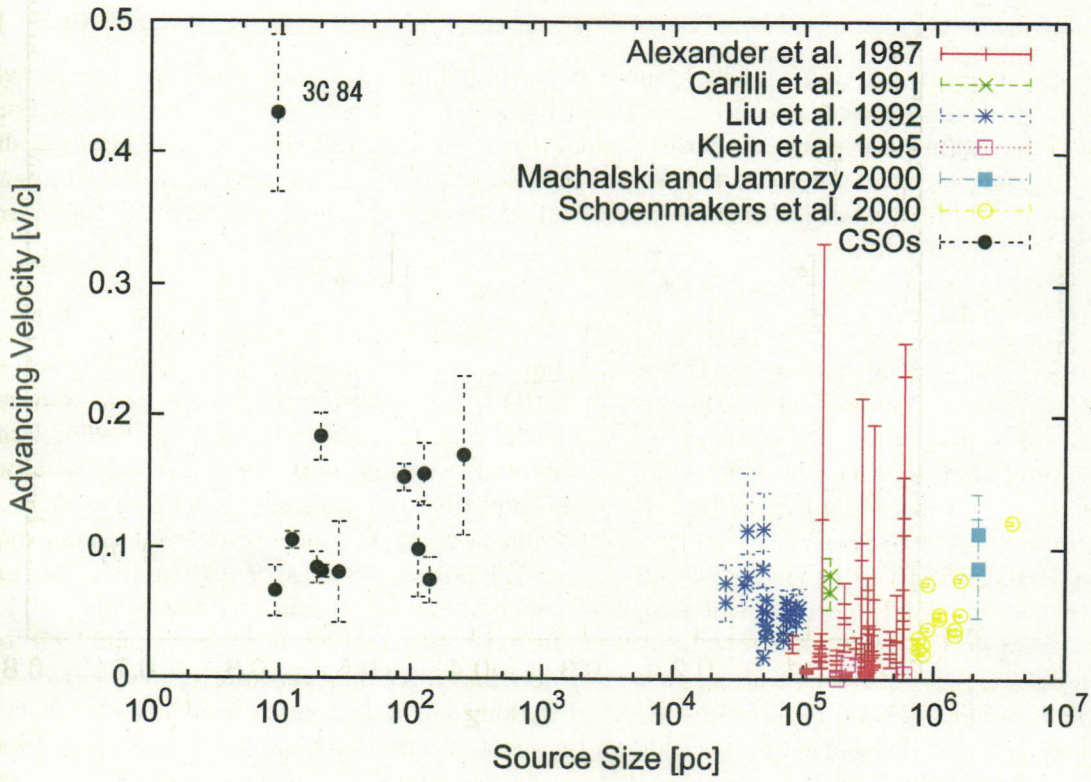

Figure 4.2: Advance velocities of CSOs and FRII sources. The sample of CSOs is same one shown in Table 4.1.

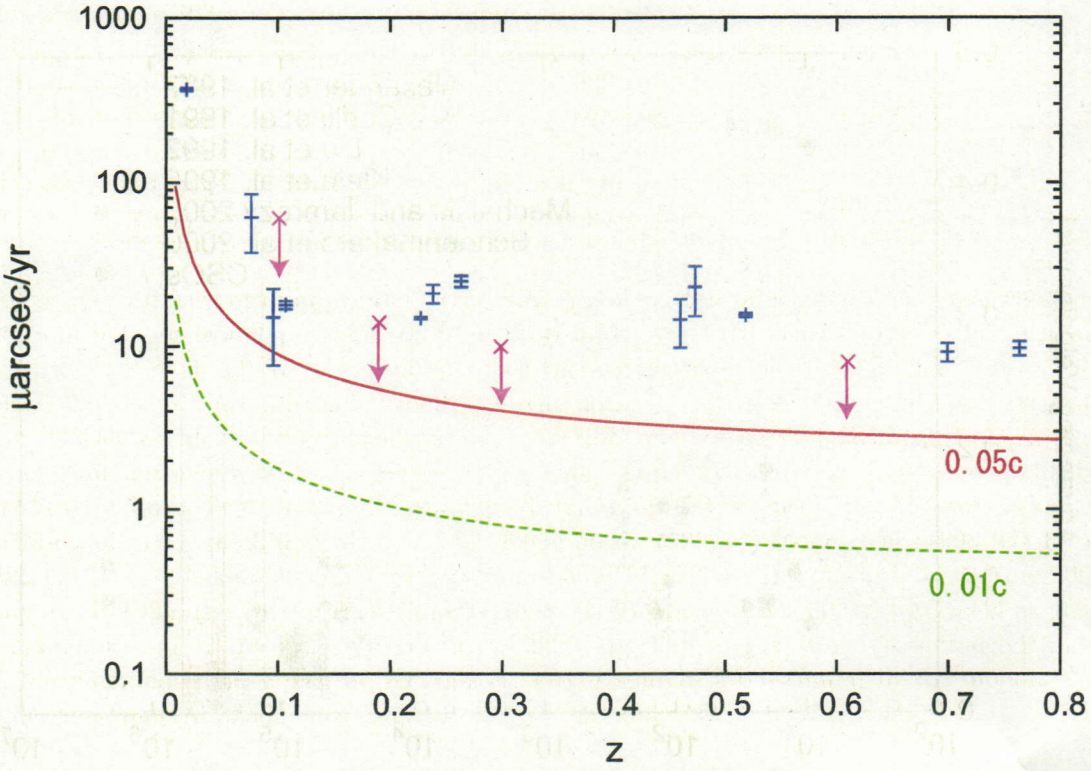

Figure 4.3: Apparent advance velocity of CSOs. Arrow indicates upper limit (Gugliucci et al. 2005; Taylor & Vermeulen 1997). The sample of CSOs is same one shown in Table 4.1, but information of apparent velocity was not available for some sources from references. Solid and dashed lines correspond to the velocity of $0.05c$ and $0.01c$, respectively.

Table 4.2: Best fits for the hot spot size and pressure.

Hot Spot Size		
	a	b
$l < 1$ kpc	1.04 ± 0.07	-0.91 ± 0.09
$l > 1$ kpc	0.42 ± 0.04	-0.6 ± 0.07
Hot Spot Pressure		
	a	b
0.01 kpc$\leq l \leq$ 1000 kpc	-1.44 ± 0.05	-6.07 ± 0.09

Note.—The parameters a and b are defined by $\log y = a \log x + b$.

4.3.1 Luminosity

Firstly, we investigate the luminosity of hot spot. Although we have only a little understanding of the mechanism of production of radio emission at the hot spot, the luminosity is basically considered to reflect the injection power from the jet into ambient medium. Thus the luminosity is a basic parameter to investigate energy scale of radio sources. Figure 4.4 shows the hot spot luminosity (L_{hs}) with respect to the distance from the core (l_{hs}). The luminosity L_{hs} is calculated as

$$L_{hs} = 4\pi d^2 \int_{\nu_{min}}^{\nu_{max}} S(\nu) d\nu, \tag{4.2}$$

where d is the distance to the source and ν_{min} and ν_{max} are the lower and upper cutoff frequencies. We assumed $\nu_{min} = 10$ MHz and $\nu_{max} = 100$ GHz. The absence of low-luminosity sources is clearly seen at $l_{hs} < 10$ kpc. However, as seen in followings, the absence of low-luminosity sources can be produced by the sample selection criteria. Figure 4.5 shows the flux density of hot spot with respect to l_{hs}. The lack of faint sources at $l_{hs} < 10$ kpc can be seen, as well as in Figure 4.4. We note that hot-spot parameters of CSOs and MSOs were obtained by VLBI observation whereas those of larger sources were obtained by VLA observations. Typical baseline sensitivity of VLBI observation is a few tens of Jy. This sensitivity limit presumably affects the apparent absence of faint hot spot in CSOs and MSOs. One could think that the hot spot of CSOs and MSOs are intrinsically brighter than that of FRII sources. However, faint GPS and CSS sources (e.g., Snellen et al. 1998; Tschager et al. 2003) that have not been studied their morphology by VLBI observation possibly contain CSOs and MSOs which have faint hot spots. High sensitivity VLBI observation for faint GPS and CSS samples is needed to derive conclusions. It is so far not clear whether there is the luminosity evolution of hot spot. However, we should notice that the luminosity of CSOs and MSOs are almost equivalent to that of FRII sources. This indicates that the jet power of CSOs and MSOs are favorably comparable with that of FRII sources.

4.3.2 Size and Pressure

Figure 4.6 and 4.7 show the hot spot size (r_{hs}) and pressure (P_{hs}) with respect to l_{hs}, together with the best linear fit on the log-log plane ($\log y = a \log x + b$). The linear fit for hot spot size is performed separately between $l_{hs} < 1$ kpc and $l_{hs} > 1$ kpc. The best fit parameters are listed in Table 4.2. In the calculation of the hot spot pressures, we assumed minimum-energy field (see Appendix A). The hot spot pressure P_{hs} shows a simple power-law relation with l_{hs}. The hot spot size r_{hs} also shows self-similar growth for the first 1 kpc and a flattening for large sources. This is almost consistent with Perucho & Marti (2003) and Jeyakumar & Saikia (2000), but a large number of sources in our sample allows us to see the tendency more clearly. Discussion on this trend is given in section 4.3.3.

4.3.3 Interpretations for Observational Trends of Hot Spot Size and Pressure

We now consider the interpretations of observational trends of hot spot size (r_{hs}) and pressure with respect to l_{hs}. In this section, we model a simple dynamical evolution of hot spot and mention that the model well reproduces the observational trends.

According to the basic model of radio source evolution by Scheuer (1974) and Blandford & Rees (1974), hot spot is interpreted as "working surface" that is produced by the interaction between the jet and ambient medium. Advance speed of the hot spot is determined by balancing the thrust of jet against external ram pressure. Under the ram-pressure equilibrium assumption, the dynamical equation along the hot spot advance is given by

$$P_{hs} = \rho_{ext} v_{hs}^2, \tag{4.3}$$

where ρ_{ext} is the density of external medium, v_{hs} is the advance velocity of hot spot. Because hot spot moves away from the core, these parameters can be defined as a function of l_{hs}. As we discussed in section 4.2, the advance velocity of hot spot does not differ significantly between CSOs and FRI I sources. We have so far no information about the advance velocity for MSOs, but we here assume v_{hs} is constant from CSOs to MSOs to FRII sources. Therefore v_{hs} does not depend on l_{hs}. Then the hot spot pressure only depends on the ambient density ρ_{ext}. The density profile of external medium is expected to decrease with l_{hs}. Therefore ρ_{ext} in terms of l_{hs} may be written as power-law function of

$$\rho_{ext} \propto l_{hs}^{-\alpha}. \tag{4.4}$$

Substituting this relation to equation 4.3, we obtain

$$P_{hs} \propto l_{hs}^{-\alpha}. \tag{4.5}$$

Thus the hot spot pressure is expected to decrease with radio source evolution. This model is indeed consistent with the observational trend.

Basic dynamical equation 4.3 is based on the 1-dimensional pressure balance, thus the variation of hot spot size can not be treated in this equation. However, according to the hydrodynamical simulations (e.g., Scheck et al. 2002), the hot spot size is expected to show self-similar growth with the radio lobe evolution due to the sideway escape of the post-shock flow. Observational trend of hot spot size also shows self-similar growth except the slope change at $l_{hs} \simeq 1$ kpc.

More physically reasonable model (e.g., Kawakatu & Kino 2006), which treats the dynamical evolution of hot spot with the aid of cocoon dynamics (Kino & Kawakatu 2005), also predicts power-law variation of hot spot size and pressure with the radio lobe evolution. In any case, important point is that the hot spot size and pressure of CSOs, MSOs, and FRII sources are on a track which is expected from the dynamical evolution model, except the slope change of hot spot size. Overall, observational trends of hot spot size and pressure imply a evolutional track from CSOs to MSOs to FRII sources.

4.3.4 Magnetic Field of Hot Spot

Figure 4.8 shows the magnetic field strength of hot spot (B_{hs}) against l_{hs}. The magnetic field strength is estimated under the minimum-energy assumption. Magnetic field strength shows good correlation with l_{hs}. This is natural consequence because we have already confirmed the good correlation between the equipartition pressure of the hot spot and l_{hs}. It should be noted that estimated magnetic field strongly depends on the observed hot spot size than luminosity ($B_{hs} \propto L_{hs}^{2/7} r_{hs}^{-6/7}$). Although the change of slope can be seen in $r_{hs} - l_{hs}$ plane (Figure 4.6), there is no apparent change of slope in $B_{hs} - l_{hs}$ plane (Figure 4.8). The absence of the slope-change in $B_{hs} - l_{hs}$ plane indicates that the magnetic field of hot spot is more fundamental parameter to investigate the evolution of radio source.

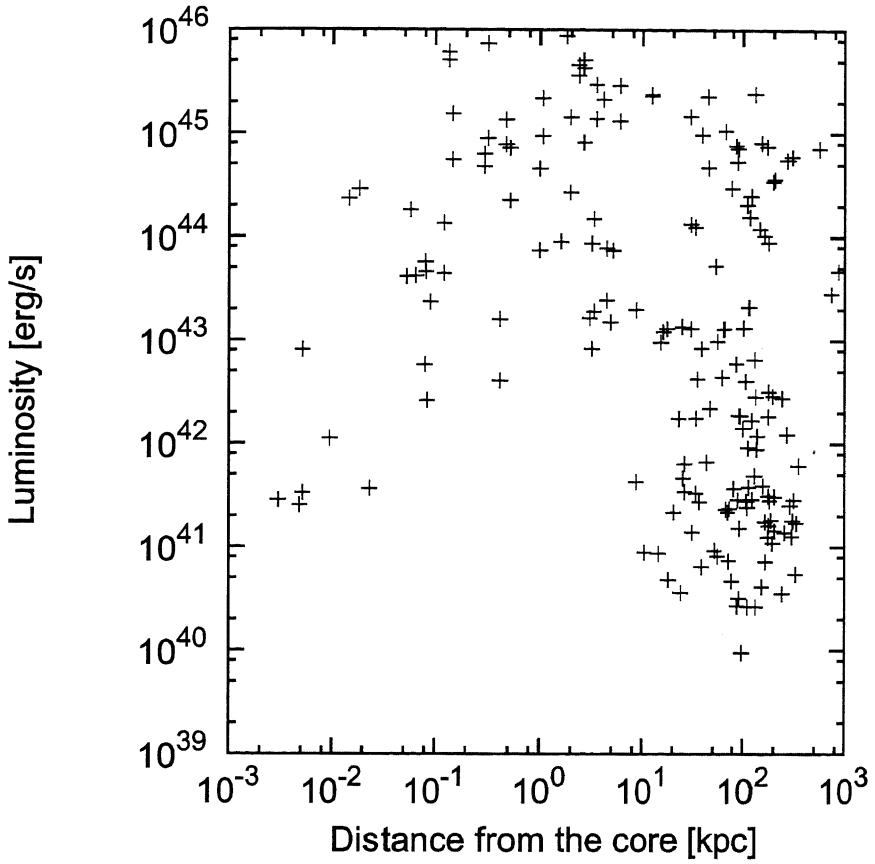

Figure 4.4: The relation of hot spot luminosity (L_{hs}) and hot spot distance from the core (l_{hs}).

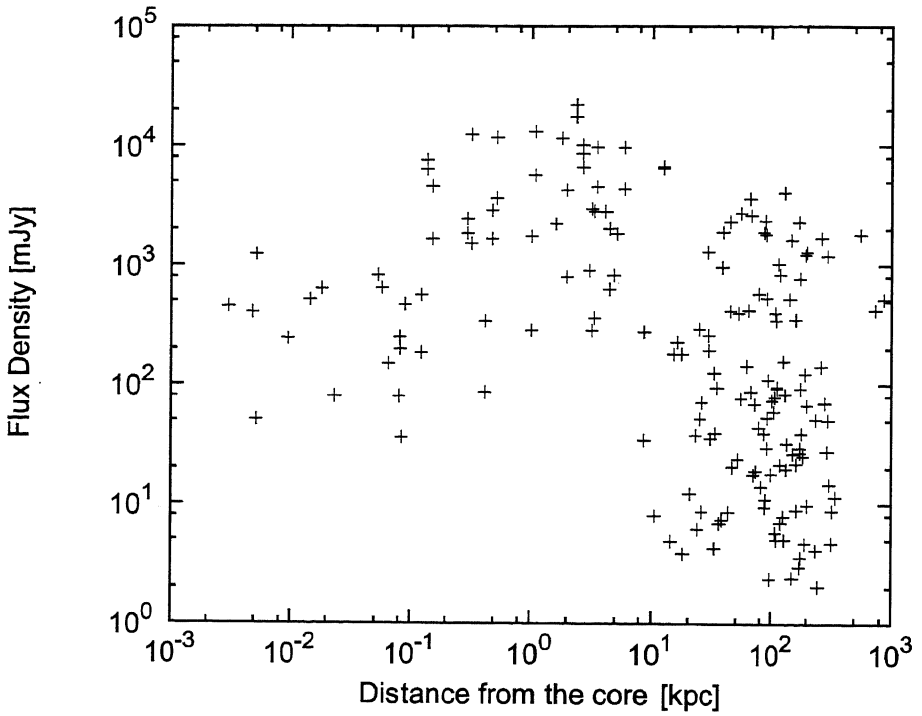

Figure 4.5: The relation of hot spot flux density and hot spot distance from the core (l_{hs}).

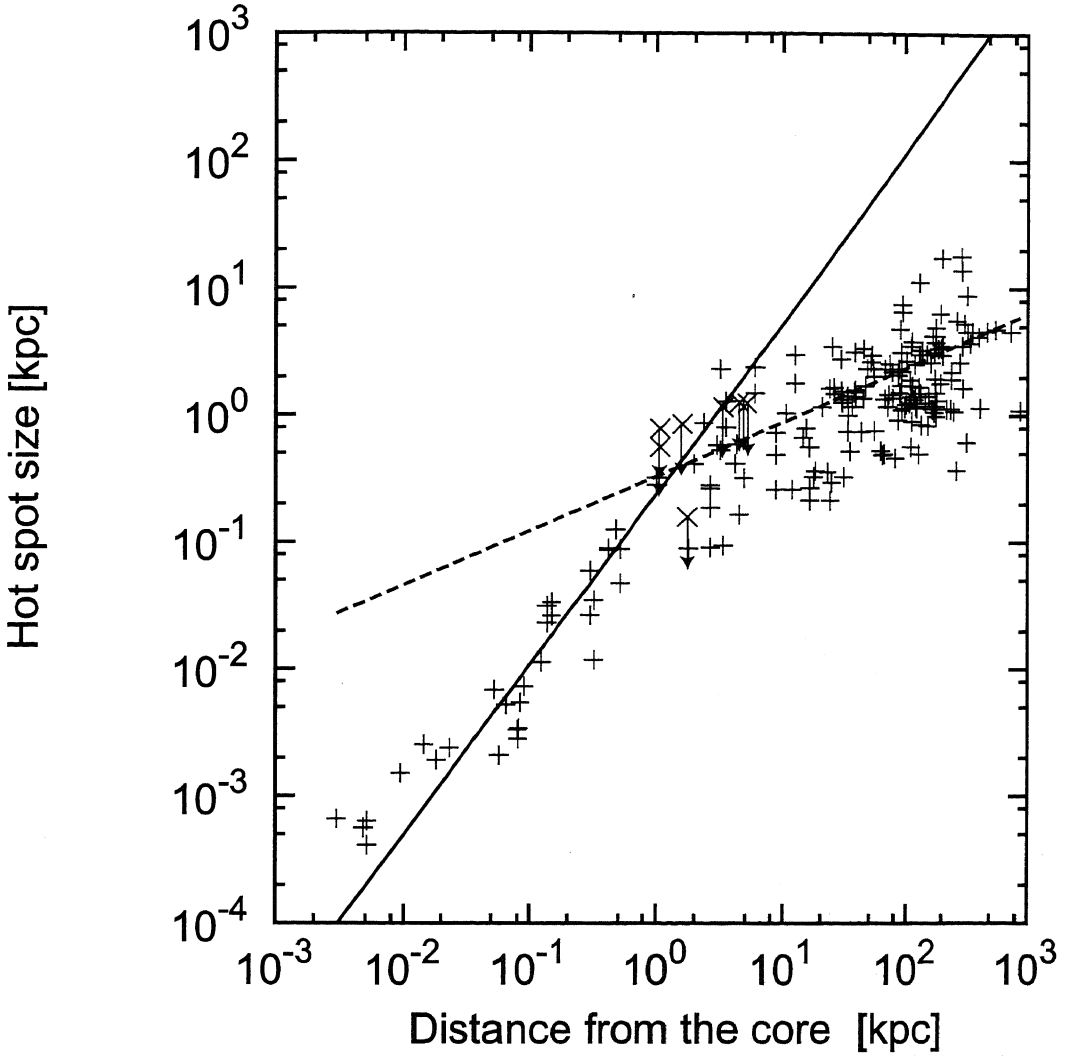

Figure 4.6: The relation of hot-spot size (r_{hs}) and hot-spot distance from the core (l_{hs}). Crosses with arrows indicate upper limit. Solid line corresponds to the best-fit for the sources whose distances of hot spots are in the range from 0.001 kpc to 1 kpc whereas broken line corresponds to that for the sources whose distance of hot spots are in the range from 1 kpc to 1000 kpc.

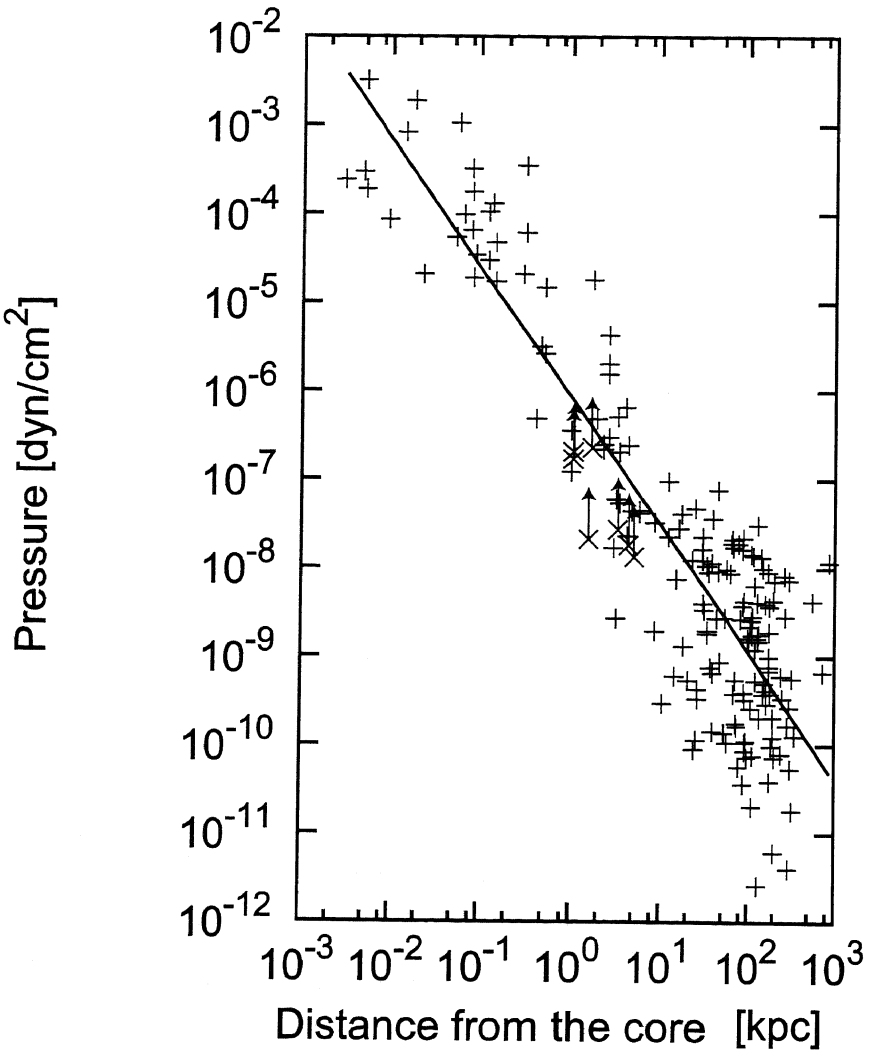

Figure 4.7: The relation of hot spot pressure and hot spot distance from the core.

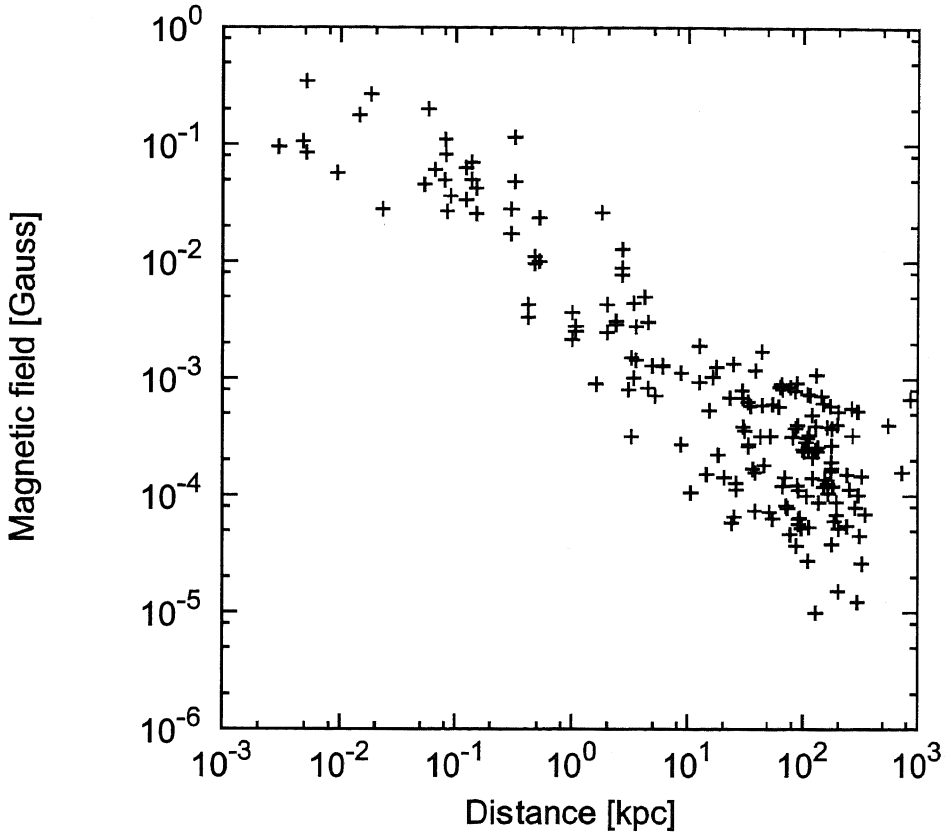

Figure 4.8: The relation of hot spot magnetic field and hot spot distance from the core. Magnetic field strength is estimated in minimum-energy assumption.

Table 4.3: Physical parameter of hot spots.

Cat.	IAU	z	Frq. [GHz]	Flux [mJy]	θ_{maj} [pc]	θ_{min} [pc]	L [erg/s]	B [G]	Ue [erg/cm^3]	Ub [erg/cm^3]	Ptot [dyn/cm^2]	Dist [kpc]	ref.	note
3C 9	0017+154	2.012	4.9	47.3	3.52×10^3	2.05×10^3	1.47×10^{45}	7.90×10^{-4}	2.46×10^{-10}	2.48×10^{-8}	1.65×10^{-8}	2.94×10^1		
				15.2	5.12×10^3	1.59×10^3	4.71×10^{44}	5.93×10^{-4}	1.38×10^{-10}	1.40×10^{-8}	9.31×10^{-9}	4.46×10^1	(c)	
3C 15	0034−014	0.073	8.35	5	1.96×10^3	1.30×10^3	3.64×10^{40}	5.85×10^{-5}	1.35×10^{-12}	1.36×10^{-10}	9.07×10^{-11}	2.37×10^1	(a)	
3C 19	0038+32	0.482	8.46		2.68×10^2	2.68×10^2						1.63×10^1	(j)	
	0039+373	1.006	1.67	229	2.78×10^1	2.55×10^1	4.81×10^{44}	2.81×10^{-2}	3.11×10^{-7}	3.14×10^{-5}	2.09×10^{-5}	2.96×10^{-1}		
				303	7.81×10^1	4.08×10^1	6.36×10^{44}	1.73×10^{-2}	1.18×10^{-7}	1.19×10^{-5}	7.93×10^{-6}	2.96×10^{-1}	(d)	
4C 39.02	0039+391	1.01	1.66	35	4.15×10^2	2.31×10^2	7.42×10^{43}	2.16×10^{-3}	1.83×10^{-9}	1.85×10^{-7}	1.24×10^{-7}	1.01		
				216	2.96×10^2	2.67×10^2	4.58×10^{44}	3.68×10^{-3}	5.34×10^{-9}	5.39×10^{-7}	3.60×10^{-7}	1.01	(e)	
3C 20	0040+517	0.174	8.44	260	5.57×10^2	4.24×10^2	1.29×10^{43}	8.51×10^{-4}	2.85×10^{-10}	2.88×10^{-8}	1.92×10^{-8}	6.39×10^1		
				89	5.84×10^2	4.77×10^2	4.43×10^{42}	5.78×10^{-4}	1.32×10^{-10}	1.33×10^{-8}	8.86×10^{-9}	6.18×10^1	(a)	
3C 22	0048+5055	0.937	5	260	2.35×10^3	1.82×10^3	7.67×10^{44}	7.88×10^{-4}	2.44×10^{-10}	2.47×10^{-8}	1.65×10^{-8}	8.57×10^1		
				361	2.76×10^3	1.88×10^3	1.06×10^{45}	8.11×10^{-4}	2.59×10^{-10}	2.62×10^{-8}	1.75×10^{-8}	6.69×10^1	(b)	
	0108+388	0.699	15.4	105	2.93	2.17	2.35×10^{44}	1.78×10^{-1}	1.24×10^{-5}	1.26×10^{-3}	8.37×10^{-4}	1.45×10^{-2}		
				130	2.6	1.25	2.91×10^{44}	2.68×10^{-1}	2.83×10^{-5}	2.86×10^{-3}	1.91×10^{-3}	1.81×10^{-2}	(k)	
3C 42	0125+287	0.395	8.4	146.3	4.26×10^3	1.69×10^3	5.26×10^{43}	3.23×10^{-4}	4.10×10^{-11}	4.14×10^{-9}	2.76×10^{-9}	5.25×10^1	(i)	a
3C 49	0127+23	1.459	4.99	780	1.19×10^2	5.95×10^1	8.78×10^{45}	2.62×10^{-2}	2.70×10^{-7}	2.72×10^{-5}	1.82×10^{-5}	1.79		
				190	5.95×10^2	2.38×10^2	2.14×10^{45}	5.00×10^{-3}	9.84×10^{-9}	9.93×10^{-7}	6.62×10^{-7}	4.17	(g)	
3C 46	0132+37	0.4373	8.47		4.20×10^3	4.20×10^3						4.04×10^2		
					4.20×10^3	3.17×10^4						2.93×10^2	(j)	
3C 47	0133+207	0.425	4.9	268	4.65×10^3	2.90×10^3	8.88×10^{43}	2.68×10^{-4}	2.84×10^{-11}	2.87×10^{-9}	1.91×10^{-9}	1.76×10^2		
3C 49	0138+136	0.621	1.66	1550	1.18×10^2	6.42×10^1	8.2×10^{44}	1.28×10^{-2}	6.43×10^{-8}	6.49×10^{-6}	4.33×10^{-6}	2.67		
				130	2.41×10^2	1.34×10^2	6.88×10^{43}	3.37×10^{-3}	4.48×10^{-9}	4.52×10^{-7}	3.02×10^{-7}	2.67	(f)	
3C 55	0154+28	0.7348	5	247	4.04×10^3	1.96×10^3	3.62×10^{44}	5.22×10^{-4}	1.07×10^{-10}	1.08×10^{-8}	7.22×10^{-9}	2.02×10^2		
				236	3.64×10^3	3.14×10^3	3.46×10^{44}	4.05×10^{-4}	6.47×10^{-11}	6.54×10^{-9}	4.36×10^{-9}	1.96×10^2	(b)	
3C 67	0221+27	0.31	1.66	900	1.95×10^3	5.84×10^2	7.83×10^{43}	8.29×10^{-4}	2.71×10^{-10}	2.73×10^{-8}	1.82×10^{-8}	4.48		
				280	2.34×10^2	9.74×10^1	2.44×10^{43}	3.03×10^{-3}	3.62×10^{-9}	3.65×10^{-7}	2.43×10^{-7}	4.48	(f)	
3C 68.1	0229+341	1.238	4.9	362	4.73×10^3	1.32×10^3	2.43×10^{45}	1.08×10^{-3}	4.59×10^{-10}	4.63×10^{-8}	3.09×10^{-8}	1.30×10^2	(c)	
	0255+460	1.21	1.66	396	5.62×10^2	2.63×10^2	1.44×10^{45}	4.29×10^{-3}	7.24×10^{-9}	7.31×10^{-7}	4.87×10^{-7}	1.97		
				74	5.21×10^2	3.05×10^2	2.7×10^{44}	2.49×10^{-3}	2.45×10^{-9}	2.47×10^{-7}	1.65×10^{-7}	1.97	(e)	
3C 79	0307+169	0.2559	8.44	4	7.27×10^2	2.77×10^2	4.92×10^{41}	3.95×10^{-4}	6.15×10^{-11}	6.21×10^{-9}	4.14×10^{-9}	1.27×10^2		
				15	1.84×10^3	1.18×10^3	1.85×10^{42}	1.94×10^{-4}	1.48×10^{-11}	1.49×10^{-9}	9.94×10^{-10}	1.75×10^2	(a)	
3C 84	0316+413	0.0183	21.81	383.7	7.91×10^{-1}	3.40×10^{-1}	2.56×10^{41}	1.06×10^{-1}	4.43×10^{-6}	4.48×10^{-4}	2.99×10^{-4}	4.79×10^{-3}		
				429.4	9.35×10^{-1}	3.98×10^{-1}	2.86×10^{41}	9.56×10^{-2}	3.60×10^{-6}	3.64×10^{-4}	2.42×10^{-4}	2.98×10^{-3}	(o)	
3C 98	0356+109	0.0306	8.35	40	2.40×10^3	1.99×10^3	4.73×10^{40}	4.66×10^{-5}	8.54×10^{-13}	8.63×10^{-11}	5.75×10^{-11}	7.74×10^1		
				27	2.29×10^3	1.17×10^3	3.19×10^{40}	5.72×10^{-5}	1.29×10^{-12}	1.30×10^{-10}	8.67×10^{-11}	9.09×10^1	(a)	
	0402+379	0.055	15.35	208	1.53	1.53	1.13×10^{42}	5.70×10^{-2}	1.28×10^{-6}	1.29×10^{-4}	8.60×10^{-5}	9.42×10^{-3}		
				68	2.41	2.41	3.69×10^{41}	2.80×10^{-2}	3.09×10^{-7}	3.12×10^{-5}	2.08×10^{-5}	2.30×10^{-2}	(m)	
3C 105	0404+035	0.089	8.35	3.2	2.63×10^3	1.24×10^3	3.57×10^{40}	5.50×10^{-5}	1.19×10^{-12}	1.20×10^{-10}	8.01×10^{-11}	2.40×10^2		
				110	4.34×10^2	3.10×10^2	1.23×10^{42}	5.58×10^{-4}	1.23×10^{-10}	1.24×10^{-8}	8.27×10^{-9}	2.65×10^2	(a)	
3C 109	0410+11	0.3056	8.26		4.25×10^3	4.25×10^3						1.67×10^2		
					4.25×10^3	4.25×10^3						1.77×10^2	(j)	
4C 14.11	0411+141	0.206	8.44	1.7	3.59×10^3	2.99×10^2	1.25×10^{41}	1.62×10^{-4}	1.03×10^{-11}	1.04×10^{-9}	6.96×10^{-10}	1.74×10^2		
				3.3	8.69×10^2	2.70×10^2	2.43×10^{41}	3.12×10^{-4}	3.83×10^{-11}	3.87×10^{-9}	2.58×10^{-9}	1.09×10^2	(a)	
3C 111	0415+379	0.0485	8.35	300	1.17×10^3	6.31×10^2	9.22×10^{41}	2.58×10^{-4}	2.62×10^{-11}	2.64×10^{-9}	1.76×10^{-9}	1.11×10^2		
				76	1.71×10^3	9.92×10^2	2.34×10^{41}	1.21×10^{-4}	5.73×10^{-12}	5.79×10^{-10}	3.86×10^{-10}	6.68×10^1	(a)	
3C 119	0429+415	0.408	1.66	4200	6.77×10^1	2.71×10^1	7.29×10^{44}	2.37×10^{-2}	2.21×10^{-7}	2.23×10^{-5}	1.49×10^{-5}	5.19×10^{-1}		
				1300	1.26×10^2	4.96×10^1	2.26×10^{44}	1.00×10^{-2}	3.96×10^{-8}	4.00×10^{-6}	2.67×10^{-6}	5.19×10^{-1}	(f)	
3C 123	0433+295	0.2177	8.44	21	4.67×10^2	2.49×10^2	1.76×10^{42}	6.86×10^{-4}	1.86×10^{-10}	1.87×10^{-8}	1.25×10^{-8}	2.27×10^1		
				162	3.42×10^2	2.49×10^2	1.36×10^{43}	1.34×10^{-3}	7.12×10^{-10}	7.19×10^{-8}	4.79×10^{-8}	2.46×10^1	(a)	
3C 132	0453+227	0.214	8.44	53	5.84×10^2	4.61×10^2	4.26×10^{42}	5.83×10^{-4}	1.34×10^{-10}	1.35×10^{-8}	9.01×10^{-9}	3.47×10^1		
				22	1.23×10^3	7.69×10^2	1.77×10^{42}	2.74×10^{-4}	2.95×10^{-11}	2.98×10^{-9}	1.99×10^{-9}	3.35×10^1	(a)	
3C 135	0511+008	0.1273	8.35	1.7	1.15×10^3	5.21×10^2	4.16×10^{40}	1.19×10^{-4}	5.62×10^{-12}	5.67×10^{-10}	3.78×10^{-10}	1.51×10^2		

Table 4.3: Physical parameter of hot spots.

Cat.	IAU	z	Frq. [GHz]	Flux [mJy]	θ_{maj} [pc]	θ_{min} [pc]	L [erg/s]	B [G]	Ue [erg/cm^3]	Ub [erg/cm^3]	Ptot [dyn/cm^2]	Dist [kpc]	ref.	note
				77	9.59×10^3	3.54×10^3	1.88×10^{42}	6.47×10^{-5}	1.65×10^{-12}	1.67×10^{-10}	1.11×10^{-10}	9.38×10^1	(a)	
3C 136.1	0512+248	0.064	8.35	56	2.32×10^4	1.16×10^4	3.09×10^{41}	1.52×10^{-5}	9.13×10^{-14}	9.22×10^{-12}	6.15×10^{-12}	2.01×10^2		
				23	1.39×10^4	1.39×10^4	1.27×10^{41}	1.23×10^{-5}	5.97×10^{-14}	6.03×10^{-12}	4.02×10^{-12}	2.96×10^2	(a)	
3C 153	0605+480	0.2771	8.44	133	6.92×10^2	2.91×10^2	1.98×10^{43}	1.12×10^{-3}	4.94×10^{-10}	4.99×10^{-8}	3.33×10^{-8}	8.74		
				87	4.01×10^2	2.55×10^2	1.3×10^{43}	1.25×10^{-3}	6.17×10^{-10}	6.23×10^{-8}	4.16×10^{-8}	1.75×10^1	(a)	
3C 171	0651+542	0.2384	8.06	120	8.93×10^2	2.32×10^2	1.22×10^{43}	1.03×10^{-3}	4.20×10^{-10}	4.24×10^{-8}	2.83×10^{-8}	1.62×10^1		
				95	9.59×10^2	6.28×10^2	9.64×10^{42}	5.35×10^{-4}	1.13×10^{-10}	1.14×10^{-8}	7.59×10^{-9}	1.52×10^1	(a)	
3C 172	0659+252	0.5191	8.46		1.13×10^3	1.13×10^3						2.18×10^2		
					1.13×10^3	1.13×10^3						2.36×10^2	(j)	
3C 173.1	0702+749	0.292	8.44	8.3	1.77×10^3	6.77×10^2	1.41×10^{42}	2.48×10^{-4}	2.43×10^{-11}	2.46×10^{-9}	1.64×10^{-9}	9.93×10^1		
				10	1.88×10^3	9.40×10^2	1.69×10^{42}	2.13×10^{-4}	1.79×10^{-11}	1.81×10^{-9}	1.21×10^{-9}	1.20×10^2	(a)	
4C 68.08	0707+68	1.139	1.6	1000	1.02×10^3	5.97×10^2	2.98×10^{45}	2.79×10^{-3}	3.06×10^{-9}	3.09×10^{-7}	2.06×10^{-7}	3.52		
				465	1.49×10^3	1.08×10^3	1.39×10^{45}	1.43×10^{-3}	8.10×10^{-10}	8.18×10^{-8}	5.46×10^{-8}	3.52	(g)	
3C 175	0710+118	0.768	4.9	63.5	3.23×10^3	1.98×10^3	1.04×10^{44}	3.87×10^{-4}	5.92×10^{-11}	5.97×10^{-9}	3.98×10^{-9}	1.60×10^2		
				152	2.89×10^3	2.15×10^3	2.5×10^{44}	4.90×10^{-4}	9.45×10^{-11}	9.54×10^{-9}	6.36×10^{-9}	1.19×10^2	(c)	
	0710+439	0.518	15.4	185	2.56	1.66	1.83×10^{44}	2.00×10^{-1}	1.58×10^{-5}	1.60×10^{-3}	1.06×10^{-3}	5.71×10^{-2}		
				43	6.52	4.04	4.24×10^{43}	6.08×10^{-2}	1.46×10^{-6}	1.47×10^{-4}	9.82×10^{-5}	6.49×10^{-2}	(k)	
3C 184.1	0734+805	0.1182	8.35	7	5.10×10^3	1.96×10^3	1.45×10^{41}	5.22×10^{-5}	1.07×10^{-12}	1.08×10^{-10}	7.23×10^{-11}	2.02×10^2		
				19	1.86×10^3	9.81×10^2	3.94×10^{41}	1.38×10^{-4}	7.46×10^{-12}	7.53×10^{-10}	5.02×10^{-10}	1.53×10^2	(a)	
3C 192	0802+243	0.0598	8.35	80	4.36×10^3	3.27×10^3	3.82×10^{41}	5.37×10^{-5}	1.14×10^{-12}	1.15×10^{-10}	7.66×10^{-11}	1.12×10^2		
				2	1.31×10^3	9.82×10^2	9.55×10^{39}	5.26×10^{-5}	1.09×10^{-12}	1.10×10^{-10}	7.33×10^{-11}	9.66×10^1	(a)	
3C 197.1	0818+472	0.1301	8.35	3.4	7.00×10^2	6.36×10^2	8.73×10^{40}	1.52×10^{-4}	9.05×10^{-12}	9.14×10^{-10}	6.10×10^{-10}	1.44×10^1		
				8.5	1.59×10^3	7.42×10^2	2.18×10^{41}	1.43×10^{-4}	8.02×10^{-12}	8.10×10^{-10}	5.40×10^{-10}	2.04×10^1	(a)	
4C 39.23	0822+394	1.21	1.67	424	3.17×10^1	2.09×10^1	1.55×10^{45}	4.23×10^{-2}	7.03×10^{-7}	7.10×10^{-5}	4.74×10^{-5}	1.50×10^{-1}		
				153	4.01×10^1	2.69×10^1	5.59×10^{44}	2.56×10^{-2}	2.58×10^{-7}	2.60×10^{-5}	1.74×10^{-5}	1.50×10^{-1}	(d)	
4C 14.27	0832+14	0.392	8.46		1.11×10^3	1.11×10^3						9.17×10^1	(j)	
3C 204	0833+654	1.112	4.9	61.4	1.49×10^3	1.25×10^3	2.98×10^{44}	8.47×10^{-4}	2.83×10^{-10}	2.86×10^{-8}	1.90×10^{-8}	7.75×10^1		
				42.2	1.49×10^3	1.31×10^3	2.05×10^{44}	7.41×10^{-4}	2.16×10^{-10}	2.19×10^{-8}	1.46×10^{-8}	1.09×10^2	(c)	
3C 208	0850+140	1.11	4.9	27.7	1.43×10^3	1.25×10^3	1.34×10^{44}	6.82×10^{-4}	1.83×10^{-10}	1.85×10^{-8}	1.23×10^{-8}	2.97×10^1		
				203	1.55×10^3	1.25×10^3	9.79×10^{44}	1.18×10^{-3}	5.46×10^{-10}	5.52×10^{-8}	3.68×10^{-8}	3.85×10^1	(c)	
3C 215	0903+169	0.411	4.9	7.3	2.04×10^3	1.36×10^3	2.22×10^{42}	1.83×10^{-4}	1.31×10^{-11}	1.33×10^{-9}	8.84×10^{-10}	4.61×10^1		
3C 219	0917+458	0.1744	4.87	2.9	2.63×10^3	9.56×10^2	1.1×10^{41}	8.79×10^{-5}	3.05×10^{-12}	3.08×10^{-10}	2.05×10^{-10}	1.93×10^2		
				76	8.50×10^3	4.25×10^3	2.89×10^{42}	6.82×10^{-5}	1.83×10^{-12}	1.85×10^{-10}	1.23×10^{-10}	1.94×10^2	(a)	
3C 223	0936+361	0.1368	8.35	10	7.72×10^3	2.87×10^3	2.87×10^{41}	4.54×10^{-5}	8.11×10^{-13}	8.19×10^{-11}	5.46×10^{-11}	3.09×10^2		
				6	1.32×10^4	4.41×10^3	1.72×10^{41}	2.63×10^{-5}	2.72×10^{-13}	2.75×10^{-11}	1.83×10^{-11}	3.24×10^2	(a)	
3C 223.1	0938+399	0.1075	8.35	14	3.63×10^3	1.45×10^3	2.36×10^{41}	7.85×10^{-5}	2.43×10^{-12}	2.45×10^{-10}	1.63×10^{-10}	7.32×10^1		
				13	1.63×10^3	7.26×10^2	2.19×10^{41}	1.43×10^{-4}	8.11×10^{-12}	8.19×10^{-10}	5.46×10^{-10}	6.99×10^1	(a)	
3C 225	0939+140	0.582	4.86		2.62×10^2	2.62×10^2						1.18×10^1		
					2.62×10^2	2.62×10^2						8.72	(j)	
3C 227	0945+076	0.0861	8.35	17	1.35×10^3	9.03×10^2	1.77×10^{41}	1.26×10^{-4}	6.22×10^{-12}	6.29×10^{-10}	4.19×10^{-10}	1.63×10^2		
				7	1.50×10^3	7.52×10^2	7.27×10^{40}	1.05×10^{-4}	4.35×10^{-12}	4.39×10^{-10}	2.93×10^{-10}	1.64×10^2	(a)	
3C 228	0947+145	0.5524	8.47		1.16×10^3	1.16×10^3						1.23×10^2		
3C 234	0958+290	0.1848	8.44	55.8	1.41×10^3	5.54×10^2	3.19×10^{42}	3.75×10^{-4}	5.54×10^{-11}	5.60×10^{-9}	3.73×10^{-9}	1.77×10^2		
				50	2.02×10^3	9.70×10^2	2.86×10^{42}	2.38×10^{-4}	2.24×10^{-11}	2.26×10^{-9}	1.51×10^{-9}	1.31×10^2	(a)	
3C 237	1005+07	0.877	1.6	3340	1.16×10^3	5.81×10^2	4.59×10^{45}	3.08×10^{-3}	3.75×10^{-9}	3.78×10^{-7}	2.52×10^{-7}	2.35		
				2650	1.16×10^3	5.81×10^2	3.64×10^{45}	2.89×10^{-3}	3.28×10^{-9}	3.31×10^{-7}	2.21×10^{-7}	2.35	(h)	
3C 241	1019+22	1.617	1.66	480	3.54×10^2	2.06×10^2	4.3×10^{45}	7.68×10^{-3}	2.33×10^{-8}	2.35×10^{-6}	1.57×10^{-6}	2.65		
				570	3.54×10^2	1.77×10^2	5.11×10^{45}	8.81×10^{-3}	3.06×10^{-8}	3.09×10^{-6}	2.06×10^{-6}	2.65	(f)	
3C 244.1	1030+585	0.428	8.4	355	1.48×10^3	1.20×10^3	1.57×10^{44}	7.25×10^{-4}	2.07×10^{-10}	2.09×10^{-8}	1.39×10^{-8}	1.15×10^2		
				13.5	9.23×10^2	9.23×10^2	5.96×10^{42}	3.79×10^{-4}	5.64×10^{-11}	5.70×10^{-9}	3.80×10^{-9}	8.60×10^1	(i)	a
	1031+567	0.4597	15.4	80	3.29	2.34	5.76×10^{43}	1.10×10^{-1}	4.80×10^{-6}	4.85×10^{-4}	3.23×10^{-4}	8.05×10^{-2}		
				64	3.43	3.43	4.61×10^{43}	8.21×10^{-2}	2.66×10^{-6}	2.68×10^{-4}	1.79×10^{-4}	8.14×10^{-2}	(l)	

Table 4.3: Physical parameter of hot spots.

Cat.	IAU	z	Frq. [GHz]	Flux [mJy]	θ_{maj} [pc]	θ_{min} [pc]	L [erg/s]	B [G]	Ue [erg/cm^3]	Ub [erg/cm^3]	Ptot [dyn/cm^2]	Dist [kpc]	ref.	note
3C 249.1	1100+772	0.311	4.9	188	5.35×10^3	3.82×10^3	2.83×10^{43}	1.59×10^{-4}	9.93×10^{-12}	1.00×10^{-9}	6.69×10^{-10}	7.34×10^2		
				86.3	1.52×10^3	1.01×10^3	1.3×10^{43}	3.88×10^{-4}	5.94×10^{-11}	6.00×10^{-9}	4.00×10^{-9}	2.99×10^1	(c)	
3C 263	1137+660	0.646	4.9	20.8	1.84×10^3	1.57×10^3	2.11×10^{43}	3.29×10^{-4}	4.27×10^{-11}	4.31×10^{-9}	2.87×10^{-9}	1.13×10^2		
				528	1.62×10^3	1.41×10^3	5.35×10^{44}	9.15×10^{-4}	3.30×10^{-10}	3.33×10^{-8}	2.22×10^{-8}	8.80×10^1	(c)	
3C 265	1142+31	0.811	5	286	6.99×10^3	4.18×10^3	5.55×10^{44}	3.27×10^{-4}	4.21×10^{-11}	4.25×10^{-9}	2.83×10^{-9}	2.68×10^2		
				387	3.95×10^3	2.35×10^3	7.51×10^{44}	5.83×10^{-4}	1.34×10^{-10}	1.35×10^{-8}	9.02×10^{-9}	1.72×10^2	(b)	
3C 266	1143+50	1.275	1.6	550	2.99×10^3	5.98×10^2	2.31×10^{45}	1.90×10^{-3}	1.42×10^{-9}	1.44×10^{-7}	9.59×10^{-8}	1.24×10^1		
				570	4.19×10^3	1.80×10^3	2.39×10^{45}	9.31×10^{-4}	3.42×10^{-10}	3.45×10^{-8}	2.30×10^{-8}	1.24×10^1	(h)	
	1159+394	2.37	1.67	198	2.84×10^1	1.80×10^1	6.13×10^{45}	7.04×10^{-2}	1.95×10^{-6}	1.97×10^{-4}	1.32×10^{-4}	1.36×10^{-1}		
				165	3.66×10^1	2.62×10^1	5.11×10^{45}	5.02×10^{-2}	9.93×10^{-7}	1.0×10^{-4}	6.68×10^{-5}	1.36×10^{-1}	(d)	
3C 268.3	1203+645	0.371	1.66	140	1.29×10^2	6.02×10^1	1.91×10^{43}	4.41×10^{-3}	7.65×10^{-9}	7.72×10^{-7}	5.15×10^{-7}	3.35		
				1100	1.72×10^3	6.02×10^2	1.5×10^{44}	1.02×10^{-3}	4.07×10^{-10}	4.11×10^{-8}	2.74×10^{-8}	3.35	(f)	
	1225+442	0.3478	1.67	138	1.11×10^2	6.27×10^1	1.6×10^{43}	4.28×10^{-3}	7.21×10^{-9}	7.29×10^{-7}	4.86×10^{-7}	4.16×10^{-1}		
				35	1.35×10^2	4.40×10^1	4.07×10^{42}	3.35×10^{-3}	4.41×10^{-9}	4.45×10^{-7}	2.97×10^{-7}	4.16×10^{-1}	(d)	
3C 274.1	1232+216	0.422	8.47		4.59×10^3	4.59×10^3						3.58×10^2		
					4.59×10^3	4.59×10^3						3.27×10^2	(j)	
4C 49.25	1244+49	0.206	1.6	515	6.89×10^2	4.79×10^2	1.65×10^{43}	8.01×10^{-4}	2.53×10^{-10}	2.55×10^{-8}	1.70×10^{-8}	3.02		
				470	3.74×10^2	2.70×10^2	1.51×10^{43}	1.29×10^{-3}	6.55×10^{-10}	6.62×10^{-8}	4.41×10^{-8}	4.87	(g)	
3C 277.1	1250+56	0.321	1.6	800	1.71×10^3	7.95×10^2	7.45×10^{43}	7.11×10^{-4}	1.99×10^{-10}	2.01×10^{-8}	1.34×10^{-8}	5.17		
				970	9.14×10^2	7.95×10^2	9.03×10^{43}	8.99×10^{-4}	3.18×10^{-10}	3.21×10^{-8}	2.14×10^{-8}	1.59	(g)	
3C 284	1308+277	0.2394	8.06	6	4.98×10^3	2.49×10^3	6.15×10^{41}	6.94×10^{-5}	1.90×10^{-12}	1.91×10^{-10}	1.28×10^{-10}	3.45×10^2		
				27	2.52×10^3	1.89×10^3	2.77×10^{42}	1.51×10^{-4}	9.04×10^{-12}	9.13×10^{-10}	6.09×10^{-10}	2.40×10^2	(a)	
	1314+453	1.544	1.67	175	1.58×10^2	9.24×10^1	1.36×10^{45}	1.10×10^{-2}	4.78×10^{-8}	4.82×10^{-6}	3.22×10^{-6}	4.74×10^{-1}		
				101	1.66×10^2	8.65×10^1	7.85×10^{44}	9.64×10^{-3}	3.66×10^{-8}	3.70×10^{-6}	2.47×10^{-6}	4.74×10^{-1}	(d)	
3C 285	1319+428	0.0794	4.86	4	4.21×10^3	2.81×10^3	2.66×10^{40}	2.77×10^{-5}	3.02×10^{-13}	3.05×10^{-11}	2.04×10^{-11}	1.11×10^2		
				4	1.26×10^4	9.82×10^3	2.66×10^{40}	9.89×10^{-6}	3.86×10^{-14}	3.89×10^{-12}	2.60×10^{-12}	1.30×10^2	(a)	
4C 38.37	1343+386	1.844	1.67	541	3.58×10^1	3.41×10^1	7.39×10^{45}	4.82×10^{-2}	4.71×10^{54}	9.26×10^{-5}	6.17×10^{-5}	3.18×10^{-1}		
				66	2.02×10^1	3.47	9.02×10^{44}	1.15×10^{-1}	5.21×10^{-6}	5.26×10^{-4}	3.51×10^{-4}	3.18×10^{-1}	(d)	
OQ 208	1404+286	0.077	8.4	990.5	5.33×10^{-1}	2.93×10^{-1}	8.12×10^{42}	3.47×10^{-1}	4.76×10^{-5}	4.80×10^{-3}	3.20×10^{-3}	5.15×10^{-3}		
				41	6.42×10^{-1}	6.42×10^{-1}	3.36×10^{41}	8.47×10^{-2}	2.83×10^{-6}	2.85×10^{-4}	1.90×10^{-4}	5.15×10^{-3}	(n)	
3C 299	1419+419	0.367	4.86		2.14×10^2	2.14×10^2						1.64×10^1		
					2.14×10^2	2.14×10^2						2.39×10^1	(j)	
3C 300	1420+198	0.272	8.06	1	1.08×10^3	1.08×10^3	1.39×10^{41}	1.13×10^{-4}	5.04×10^{-12}	5.09×10^{-10}	3.39×10^{-10}	2.51×10^2		
				29	1.58×10^3	9.36×10^2	4.04×10^{42}	2.88×10^{-4}	3.27×10^{-11}	3.30×10^{-9}	2.20×10^{-9}	1.05×10^2	(a)	
3C 303	1441+522	0.141	1.48	650	3.84×10^3	2.49×10^3	8.41×10^{42}	1.58×10^{-4}	9.80×10^{-12}	9.90×10^{-10}	6.60×10^{-10}	3.82×10^1		
				5	2.03×10^3	1.13×10^3	6.47×10^{40}	7.39×10^{-5}	2.15×10^{-12}	2.17×10^{-10}	1.45×10^{-10}	3.82×10^1	(a)	
3C 303.1	1443+77	0.267	1.6	1460	7.12×10^2	3.56×10^2	8.66×10^{43}	1.51×10^{-3}	8.98×10^{-10}	9.07×10^{-8}	6.05×10^{-8}	3.2		
				140	3.91×10^3	7.12×10^2	8.31×10^{42}	3.20×10^{-4}	4.02×10^{-11}	4.06×10^{-9}	2.71×10^{-9}	3.2	(h)	
3C 305.1	1447+77	1.132	1.6	450	1.79×10^3	1.19×10^3	1.32×10^{45}	1.26×10^{-3}	6.29×10^{-10}	6.35×10^{-8}	4.23×10^{-8}	5.97		
				1000	3.58×10^3	1.19×10^3	2.92×10^{45}	1.30×10^{-3}	6.68×10^{-10}	6.75×10^{-8}	4.50×10^{-8}	5.97	(h)	
3C 319	1522+546	0.192	8.44	19	3.99×10^3	2.56×10^3	1.19×10^{42}	8.76×10^{-5}	3.02×10^{-12}	3.06×10^{-10}	2.04×10^{-10}	1.36×10^2	(a)	
3C 327	1559+021	0.1039	8.44	3.5	7.06×10^2	5.29×10^2	5.5×10^{40}	1.47×10^{-4}	8.53×10^{-12}	8.62×10^{-10}	5.75×10^{-10}	3.21×10^2		
				20	1.76×10^3	6.18×10^2	3.14×10^{41}	1.71×10^{-4}	1.15×10^{-11}	1.16×10^{-9}	7.73×10^{-10}	1.75×10^2	(a)	
CTD 93	1607+268	0.473	15.29	176.2	9.27	5.7	1.36×10^{44}	6.31×10^{-2}	1.57×10^{-6}	1.58×10^{-4}	1.06×10^{-4}	1.22×10^{-1}		
				57.6	1.50×10^1	7.73	4.45×10^{43}	3.36×10^{-2}	4.44×10^{-7}	4.49×10^{-5}	2.99×10^{-5}	1.22×10^{-1}	(o)	
3C 330	1609+660	0.55	8.4	140	1.38×10^3	1.13×10^3	1.2×10^{44}	7.08×10^{-4}	1.98×10^{-10}	2.00×10^{-8}	1.33×10^{-8}	1.44×10^2	(i)	
3C 334	1618+177	0.555	4.9	19.7	3.91×10^3	1.49×10^3	1.32×10^{43}	2.39×10^{-4}	2.25×10^{-11}	2.27×10^{-9}	1.51×10^{-9}	1.01×10^2	(c)	
3C 336	1622+238	0.927	4.9	254	6.04×10^3	3.58×10^3	7.18×10^{44}	4.01×10^{-4}	6.35×10^{-11}	6.41×10^{-9}	4.27×10^{-9}	5.58×10^2		
				254	6.04×10^3	3.58×10^3	7.18×10^{44}	4.01×10^{-4}	6.35×10^{-11}	6.41×10^{-9}	4.27×10^{-9}	8.95×10^1	(c)	
3C 341	1626+27	0.448	8.47		1.06×10^3	1.06×10^3						1.70×10^2	(j)	
3C 343.1	1637+624	0.75	1.66	2460	9.58×10^2	6.20×10^2	2.2×10^{45}	2.55×10^{-3}	2.55×10^{-9}	2.58×10^{-7}	1.72×10^{-7}	1.07		
				1060	7.32×10^2	3.94×10^2	9.49×10^{44}	2.80×10^{-3}	3.09×10^{-9}	3.12×10^{-7}	2.08×10^{-7}	1.07	(f)	

Table 4.3: Physical parameter of hot spots.

Cat.	IAU	z	Frq. [GHz]	Flux [mJy]	θ_{maj} [pc]	θ_{min} [pc]	L [erg/s]	B [G]	Ue [erg/cm^3]	Ub [erg/cm^3]	Ptot [dyn/cm^2]	Dist [kpc]	ref.	note
3C 349	1658+471	0.205	8.44	4	1.49×10^3	8.95×10^2	2.91×10^{41}	1.42×10^{-4}	7.91×10^{-12}	7.99×10^{-10}	5.33×10^{-10}	1.20×10^2		
				90	1.94×10^3	1.40×10^3	6.55×10^{42}	2.48×10^{-4}	2.41×10^{-11}	2.44×10^{-9}	1.63×10^{-9}	1.28×10^2	(a)	
3C 351	1704+608	0.371	4.9	201	1.42×10^3	7.74×10^2	4.71×10^{43}	6.68×10^{-4}	1.76×10^{-10}	1.78×10^{-8}	1.18×10^{-8}	8.64×10^2	(c)	
3C 353	1717+009	0.0304	8.44	70	2.62×10^3	1.46×10^3	8.21×10^{40}	6.36×10^{-5}	1.59×10^{-12}	1.61×10^{-10}	1.07×10^{-10}	5.50×10^1		
				63	1.86×10^3	1.05×10^3	7.39×10^{40}	8.21×10^{-5}	2.65×10^{-12}	2.68×10^{-10}	1.79×10^{-10}	7.17×10^1	(a)	
3C 356	1723+510	1.079	5	134	4.82×10^3	2.26×10^3	6×10^{44}	5.28×10^{-4}	1.10×10^{-10}	1.11×10^{-8}	7.39×10^{-9}	2.98×10^2		
				182	3.81×10^3	2.26×10^3	8.15×10^{44}	6.16×10^{-4}	1.50×10^{-10}	1.51×10^{-8}	1.01×10^{-8}	1.49×10^2	(b)	
3C 381	1832+474	0.1605	8.35	9	4.99×10^2	4.24×10^2	3.71×10^{41}	3.18×10^{-4}	3.98×10^{-11}	4.02×10^{-9}	2.68×10^{-9}	8.11×10^1		
				7	2.00×10^3	9.99×10^2	2.88×10^{41}	1.22×10^{-4}	5.88×10^{-12}	5.94×10^{-10}	3.96×10^{-10}	8.86×10^1	(a)	
3C 382	1833+326	0.0578	4.87	45	2.33×10^3	2.12×10^3	1.53×10^{41}	6.35×10^{-5}	1.59×10^{-12}	1.60×10^{-10}	1.07×10^{-10}	9.15×10^1		
				8	2.43×10^3	2.22×10^3	2.71×10^{40}	3.72×10^{-5}	5.46×10^{-13}	5.51×10^{-11}	3.67×10^{-11}	8.72×10^1	(a)	
3C 388	1842+455	0.0908	8.35	40	4.41×10^3	2.52×10^3	4.66×10^{41}	6.59×10^{-5}	1.71×10^{-12}	1.73×10^{-10}	1.15×10^{-10}	2.50×10^1		
				55	1.89×10^3	1.42×10^3	6.41×10^{41}	1.28×10^{-4}	6.42×10^{-12}	6.48×10^{-10}	4.32×10^{-10}	2.58×10^1	(a)	
3C 390.3	1845+797	0.0561	8.44	67	2.57×10^3	1.24×10^3	2.81×10^{41}	9.98×10^{-5}	3.93×10^{-12}	3.97×10^{-10}	2.64×10^{-10}	1.07×10^2		
				450	4.22×10^3	2.06×10^3	1.89×10^{42}	1.12×10^{-4}	4.90×10^{-12}	4.95×10^{-10}	3.30×10^{-10}	9.10×10^1	(a)	
3C 401	1939+605	0.201	8.35	5	1.47×10^3	1.47×10^3	3.46×10^{41}	1.12×10^{-4}	4.98×10^{-12}	5.03×10^{-10}	3.36×10^{-10}	2.59×10^1		
				4	1.77×10^3	5.89×10^2	2.76×10^{41}	1.69×10^{-4}	1.13×10^{-11}	1.14×10^{-9}	7.58×10^{-10}	3.62×10^1	(a)	
	1943+546	0.263	4.99	232.4	7.8	6.81	2.35×10^{43}	3.62×10^{-2}	5.17×10^{-7}	5.22×10^{-5}	3.48×10^{-5}	8.96×10^{-2}		
				408.99	4.31×10^3	9.70×10^2	4.13×10^{43}	4.54×10^{-2}	8.12×10^{-7}	8.20×10^{-5}	5.47×10^{-5}	5.27×10^{-2}	(p)	
3C 403	1949+023	0.059	8.44	30	4.31×10^2	2.26×10^2	1.4×10^{41}	3.60×10^{-4}	5.09×10^{-11}	5.14×10^{-9}	3.43×10^{-9}	3.07×10^1		
				20	4.31×10^3	9.70×10^2	9.33×10^{40}	7.22×10^{-5}	2.05×10^{-12}	2.07×10^{-10}	1.38×10^{-10}	5.15×10^1	(a)	
3C 405	1957+405	0.0565	8.35	3060	6.32×10^2	3.63×10^2	1.3×10^{43}	8.98×10^{-4}	3.17×10^{-10}	3.21×10^{-8}	2.14×10^{-8}	6.55×10^1		
				2320	1.04×10^3	4.87×10^2	9.82×10^{42}	6.09×10^{-4}	1.46×10^{-10}	1.47×10^{-8}	9.82×10^{-9}	5.50×10^1	(a)	
3C 424	2045+068	0.127	4.53	2.7	4.16×10^2	3.12×10^2	4.84×10^{40}	2.23×10^{-4}	1.96×10^{-11}	1.98×10^{-9}	1.32×10^{-9}	1.81×10^1		
				24	1.04×10^3	4.16×10^2	4.3×10^{41}	2.72×10^{-4}	2.92×10^{-11}	2.95×10^{-9}	1.96×10^{-9}	8.74	(a)	
3C 427.1	2104+763	0.572	8.46		2.34×10^3	2.34×10^3						4.81×10^1		
					2.34×10^3	2.34×10^3						5.41×10^1	(j)	
3C 432	2120+168	1.805	4.9	5.7	1.51×10^3	1.33×10^3	1.25×10^{44}	6.35×10^{-4}	1.59×10^{-10}	1.60×10^{-8}	1.07×10^{-8}	3.31×10^1		
				105	1.80×10^3	9.29×10^2	2.29×10^{45}	1.71×10^{-3}	1.15×10^{-9}	1.16×10^{-7}	7.74×10^{-8}	4.42×10^1	(c)	
3C 433	2121+248	0.1016	8.35	6	1.13×10^3	9.53×10^2	8.93×10^{40}	1.06×10^{-4}	4.41×10^{-12}	4.45×10^{-10}	2.97×10^{-10}	1.06×10^1	(a)	
3C 436	2141+279	0.2145	8.44	2	6.78×10^3	3.08×10^3	1.62×10^{41}	3.84×10^{-5}	5.80×10^{-13}	5.86×10^{-11}	3.91×10^{-11}	1.77×10^2		
				11	1.05×10^3	6.47×10^2	8.9×10^{41}	2.60×10^{-4}	2.66×10^{-11}	2.69×10^{-9}	1.79×10^{-9}	1.34×10^2	(a)	
3C 438	2153+377	0.29	8.44	4	1.12×10^3	3.74×10^2	6.66×10^{41}	3.20×10^{-4}	4.05×10^{-11}	4.09×10^{-9}	2.72×10^{-9}	4.27×10^1		
				2	1.12×10^3	3.74×10^2	3.33×10^{41}	2.63×10^{-4}	2.72×10^{-11}	2.75×10^{-9}	1.83×10^{-9}	3.33×10^1	(a)	
3C 445	2221−021	0.0562	8.4	43	2.27×10^3	1.03×10^3	1.81×10^{41}	1.01×10^{-4}	4.03×10^{-12}	4.07×10^{-10}	2.71×10^{-10}	3.00×10^2		
				60	3.82×10^3	1.44×10^3	2.52×10^{41}	7.91×10^{-5}	2.47×10^{-12}	2.49×10^{-10}	1.66×10^{-10}	2.84×10^2	(a)	
3C 452	2243+394	0.0811	8.35	20	5.00×10^3	1.71×10^3	1.83×10^{41}	6.06×10^{-5}	1.45×10^{-12}	1.46×10^{-10}	9.73×10^{-11}	1.86×10^2		
				31	1.43×10^3	1.20×10^3	2.83×10^{41}	1.20×10^{-4}	5.71×10^{-12}	5.77×10^{-10}	3.84×10^{-10}	1.80×10^2	(a)	
3C 457	2309+184	0.428	8.46		4.62×10^3	4.62×10^3						4.78×10^2		
					1.15×10^3	1.15×10^3						4.14×10^2	(j)	
	2352+495	0.237	15.4	42	3.95	2.73	5.81×10^{42}	4.98×10^{-2}	9.75×10^{-7}	9.85×10^{-5}	6.57×10^{-5}	7.95×10^{-2}		
				19	6.79	4.14	2.63×10^{42}	2.68×10^{-2}	2.83×10^{-7}	2.85×10^{-5}	1.90×10^{-5}	8.34×10^{-2}	(k)	

Note.—Cat.:Catalogue Name. IAU:IAU name. z:redshift. Frq.:Observation frequency. θ_{maj}:Major axis of the hot spot. θ_{min}:Minor axis of the hot spot. L:Luminosity of hot spot. B:Equipartition magnetic field of hot spot. U_e:Electron energy density of hot spot in equipartition condition (k=100, k:energy ratio of electron and magnetic field). U_b:Magnetic field energy density of hot spot in equipartition condition (k=100). P:Equipartition pressure of hot spot. Dist:Hot spot distance from the core. If the core is not detected, we estimated a half of radio source extent as the distance. ref.:(a)Hardcastle et al. 1998; (b)Fernini et al. 1993; (c)Bridle et al. 1994; (d)Dallacasa et al. 2002a; (e)Dallacasa et al. 2002b; (f)Fanti et al. 1985; (g)Sanghera et al. 1995; (h)Spencer et al. 1989; (i)Fernini et al. 2002; (j)Gilbert et al. 2004; (k)Readhead et al. 1996; (l)Taylor et al. 2000; (m)Manness et al. 2003; Wang et al. 2003; (o)This thesis; (p)Polatidis et al. 1995 note:(a)Hot spot distance is not listed in original literature, so we estimated by eyes from the map in reference. (b)Hot spot size is unresolved. The sizes listed in columns 6 and 7 are upper limits.

Chapter 5

Concluding Remarks

5.1 Summaries

Here we summarize the conclusion of this thesis.

Detection of the hot spot motion and a high-frequency steepening due to synchrotron aging in CTD 93

VLBA observations over 8.5 yr confirmed the evidence of an increase in the separation between the hot spot and the counter hot spot. The separation velocity of hot spot along the source axis is 0.34±0.11c. Assuming that two hot spots are moving apart from the core at equal speeds, the advance velocity is 0.17±0.06c. The resultant kinematic age, which is obtained by dividing the total extent of radio source by the separation rate, is 2200±700 yr. Our multifrequency VLBI observation revealed that the break frequency due to synchrotron aging decreases with the distance from the hot spot, which is consistent with the basic scenario of radio lobe evolution. Linear fit to the synchrotron age distribution across the lobe yields the advance velocity of $0.232 \pm 0.005c$ assuming the minimum-energy field. Extrapolating to the age of the center of the source, resultant age is 1720±40 yr.

Solid evidence for the hot spot motion and detailed distribution of break frequency in innermost radio lobe of 3C 84

Since 3C 84 is one of the nearest CSOs, we successfully revealed a significant hot spot advance, and illustrated detailed distribution of break frequency. We confirmed the expansion of both southern and northern counter lobes and significant hot spot motion by VLBA observations over 4.5 yr. The advance velocity of hot spot is 0.43±0.06c, which results in a kinematic age of 33±5 yr in 2000. The break frequency decreases with the distance from the hot spot. The lowest break frequency of 2.4±1.3 GHz is found near the core, yielding the synchrotron age of 24^{+14}_{-5} yr in 1995, assuming the minimum-energy field.

Agreement of Kinematic Age and Synchrotron Age

We proved that CTD 93 and 3C 84 are young radio sources from both kinematic- and synchrotron-aging studies. This is strong evidence for the hypothesis that CSOs are young radio sources. Also our measurements of kinematic age and synchrotron age for these two sources show good agreements between them. This is the first case to show the relation between the kinematic age and synchrotron age. The agreement between kinematic age and synchrotron age implies the validity of the minimum-energy assumptions in synchrotron-aging analyses.

Advance Speed of Hot Spot

By compiling FRII sources whose ages are estimated by the synchrotron-aging study, we found an averaged hot-spot advance velocity of $\sim 0.05c$. This shows no significant difference with an averaged advance velocity of CSOs of $\sim 0.1c$. If we allow the hypothesis that CSOs evolve into FRII sources, this coincidence implies that the advance velocity is independent of the linear size of radio source. Although it is not so far clear why the advance velocity is independent of the linear size, this result will be helpful to establish more refined model of radio lobe evolution.

Supporting Evidence for Evolutional Sequence CSOs-MSOs-FRII from Dynamical Point of View

We presented how the physical condition of the hot spot varies with the size of radio source by compiling a large number of samples among CSOs, MSOs, and FRII sources. The hot spot luminosity of CSOs and MSOs are almost equivalent to that of FRII sources. This indicates that jet power of CSOs and MSOs are favorably comparable to that of FRII sources. The hot spot pressure shows a simple power-law decrease with increasing the linear size of radio source. The hot spot radius shows a self-similar growth with increasing the linear size up to $\sim$1 kpc, and becomes a slower growth for larger linear size. Although these power-law changes are previously reported, a large number of sources in our sample allows us to see the tendencies more clearly. These power-law tendencies are expected from the dynamical evolution models of radio source. This is a supporting evidence for evolutional sequence from CSOs to MSOs to FRII sources.

5.2 Future Works

5.2.1 Both Kinematic- and Synchrotron-Aging Studies for MSOs and FRII

We revealed the relation between kinematic age and synchrotron age only for two CSOs. Further studies not only for a large number of CSOs but also for MSOs and FRII are needed to investigate whether the relation is universal. However, kinematic-aging study for MSOs and FRII is technically challenging. Phase referencing VLBI observations can make it possible to measure hot spot advance of these sources.

5.2.2 Further Confirmation of Validity of Synchrotron-Aging Analysis

For simplicity, we have assumed a constant magnetic field (magnetic field does no vary with time) in synchrotron-aging analysis. On the other hand, as shown in Chapter 4, the magnetic field of hot spot decreases with increasing the linear size of radio source. This signals that the magnetic field is not constant with radio source evolution. One might expect that observed break frequency distribution across the radio lobe is caused by the time variation of magnetic field. Also magnetic field decreasing with time will lead overestimate of the synchrotron age ($t \propto B^{-1.5}$). This effect is more serious for larger sources. Therefore, the advance speeds of hot spot for FRII sources, which are estimated from synchrotron age, might be faster than the value estimated in Chapter 4. However, we have no reliable model for time variation of magnetic field in radio lobes. It is so far difficult to estimate synchrotron age taking into account the time variation of magnetic field. Observations of time variation of break frequency distribution could decouple purely synchrotron-aging effect from the time variation of magnetic field. Innermost radio source of 3C 84 is the best target to investigate the time variation of break frequency distribution. We are planning new observations to solve this issue.

5.2.3 Do CSOs live long enough to grow into FRII sources?

Overall results are consistent with an interpretation that CSOs and MSOs are major subclasses of powerful extragalactic radio sources, and support the evolutional sequence from CSOs to MSOs to FRII sources. However, we note that there is still room for further investigation whether CSOs will live long enough to grow into FRII sources. Although all CSOs seem to be potentially possible to evolve large sources from our study of physical quantities of the hot spot, some CSOs clearly keep decreasing their total flux for a long time (e.g., 3C 84, OQ 208). This indicates that whether CSOs will evolve into large sources only depends on the continuance of outflow from central engine. Furthermore, it may depend on whether the mass accretion onto the SMBH is continuance or not. Observations probe to accretion region using X-ray telescope and direct imaging of the generation of the jet using higher resolution VLBI such as VSOP-2 are needed to answer this question.

Acknowledgments

This thesis would not have been possible without supports of many scientists and engineers.

Firstly, I would like to acknowledge Prof. Makoto Inoue and Prof. Noriyuki Kawaguchi, my supervisors, for giving me the opportunities to join the space VLBI project. Their continuing support and encouragement have been instrumental in the progress I have made in my work to date. I gratefully appreciate Prof. Yutaka Uchida, my supervisor in master course, for inspiring me to advance the road to being an astronomer. Dr. Seiji Kameno taught me the foundation of radio astronomy and observation technique of interferometer. Dr. Keiichi Asada and Dr. Akihiro Doi gave me the basic idea of this thesis and have spared much time to discuss the research topics. I thank Dr. Nozomu Kawakatsu for useful comments from theoretical point of view.

Many thanks for members of VLBI group in National Astronomical Observatory of Japan (NAOJ), Institute of Space and Astronautical Science/Japan Aerospace Exploration Agency (ISAS/JAXA), especially Prof. Hisashi Hirabayashi, Prof. Hideyuki Kobayashi, Prof. Masato Tsuboi, Dr. Yasuhiro Murata, Dr. Tomofumi Umemoto, Dr. Makoto Miyoshi, Dr. Phil Edwards, Dr. Yoshiharu Asaki, Dr. Yoshiaki Hagiwara, Dr. Mareki Honma, Dr. Tomoya Hirota, Dr. Nanako Mochiduki, Dr. Yusuke Kono, Dr. Tomoaki Oyama, Dr. Ryuichi Kamohara, Dr. Tomoharu Kurayama, Mr. Hiroshi Suda. I appreciate staff of The Graduate University for Advanced Studies (SOKENDAI) for kind assistance and useful discussions, especially Prof. Nobuo Arimoto, Prof. Takashi Sakurai, Prof. Tetsuya Watanabe, Dr. Tadayuki Kodama. My thanks go as well to Dr. Takahiro Sasaki, Dr. Toshihiro Kasuga, Mr. Kenichi Umezu, Mr. Tomoyuki Kudo, Ms. Satoko Takahashi, Ms. Hitomi Yamanoi, Mr. Nobuaki Saito, for friendly association and stimulation.

The VLBA is operated by the US National Radio Astronomy Observatory, a facility of the National Science Foundation (NSF) operated under the cooperative agreement by Associated Universities, Inc. We have also made use of data from University of Michigan Radio Astronomy Observatory, which has been supported by the University of Michigan and the NSF.

References

[1] Asada, K., Kameno, S., Shen, Z.-Q., Horiuchi, S., Gabuzda, D. C., & Inoue, M. 2006, PASJ, 58, 261

[2] Asada, K., Kameno, S., Inoue, M., Shen, Z.-Q., Horiuchi, S., & Gabuzda, D. C. 2000, Astrophysical Phenomena Revealed by Space VLBI, Proceedings of the VSOP Symposium, held at the Institute of Space and astronautical Science, Sagamihara, Kanagawa, Japan, January 19 - 21, 2000, Eds.: H. Hirabayashi, P.G. Edwards, and D.W. Murphy, Published by the Institute of Space and Astronautical Science, p. 51-54., 51

[3] Alexander, P., & Leahy, J. P. 1987, MNRAS, 225, 1

[4] Bell, A. R. 1978, MNRAS, 182, 147

[5] Begelman, M. C., & Cioffi, D. F. 1989, ApJL, 345, L21

[6] Blandford, R. D., Netzer, H., Woltjer, L., Courvoisier, T. J.-L., & Mayor, M. 1990, Saas-Fee Advanced Course 20. Lecture Notes 1990. Swiss Society for Astrophysics and Astronomy, XII, 280 pp. 97 figs.. Springer-Verlag Berlin Heidelberg New York

[7] Blandford, R. D., & Konigl, A. 1979, ApJ, 232, 34

[8] Blandford, R. D., & Ostriker, J. P. 1978, ApJL, 221, L29

[9] Blandford, R. D., & Rees, M. J. 1974, MNRAS, 169, 395

[10] Ballard, K. R., & Heavens, A. F. 1991, MNRAS, 251, 438

[11] Bicknell, G. V., Dopita, M. A., & O'Dea, C. P. O. 1997, ApJ, 485, 112

[12] Boehringer, H., Voges, W., Fabian, A. C., Edge, A. C., & Neumann, D. M. 1993, MNRAS, 264, L25

[13] van Breugel, W., Miley, G., & Heckman, T. 1984, AJ, 89, 5

[14] Bridle, A. H., Hough, D. H., Lonsdale, C. J., Burns, J. O., & Laing, R. A. 1994, AJ, 108, 766

[15] Burbidge, G. R. 1959, ApJ, 129, 849

[16] Burch, S. F. 1977a, MNRAS, 180, 623

[17] Burch, S. F. 1977b, MNRAS, 181, 599

[18] Carilli, C. L., Perley, R. A., Dreher, J. W., & Leahy, J. P. 1991, ApJ, 383, 554

[19] Churazov, E., Forman, W., Jones, C., Boehringer, H. 2000, A&A, 356, 788

[20] Churazov, E., Bruggen, M., Kaiser, C. R., Bohringer, H., & Forman, W. 2001, ApJ, 554, 261

[21] Cox, C. I., Gull, S. F., & Scheuer, P. A. G. 1991, MNRAS, 252, 558

[22] Croston, J. H., Hardcastle, M. J., Harris, D. E., Belsole, E., Birkinshaw, M., & Worrall, D. M. 2005, ApJ, 626, 733

[23] Dallacasa, D., Tinti, S., Fanti, C., Fanti, R., Gregorini, L., Stanghellini, C., & Vigotti, M. 2002a, A&A, 389, 115

[24] Dallacasa, D., Fanti, C., Giacintucci, S., Stanghellini, C., Fanti, R., Gregorini, L., & Vigotti, M. 2002b, A&A, 389, 126

[25] Dhawan, V., Kellerman, K. I., & Romney, J. D. 1998, ApJL, 498, L111

[26] De Young, D. S. 1993, ApJ, 402, 95

[27] Fabian, A. C., et al. 2000, MNRAS, 318, L65

[28] Fabian, A. C., Sanders, J. S., Crawford, C. S., Conselice, C. J., Gallagher, J. S., & Wyse, R. F. G. 2003, MNRAS, 344, L48

[29] Fabian, A. C., Celotti, A., Blundell, K. M., Kassim, N. E., & Perley, R. A. 2002, MNRAS, 331, 369

[30] Fanti, C., Fanti, R., Parma, P., Schilizzi, R. T., & van Breugel, W. J. M. 1985, A&A, 143, 292

[31] Fanti, R., Fanti, C., Schilizzi, R. T., Spencer, R. E., Nan Rendong, Parma, P., van Breugel, W. J. M., & Venturi, T. 1990, A&A, 231, 333

[32] Feretti, L., Giovannini, G., Gregorini, L., Spazzoli, O., & Gioia, I. M. 1990, A&A, 233, 325

[33] Feretti, L., Perola, G. C., & Fanti, R. 1992, A&A, 265, 9

[34] Ford, H. C., et al. 1994, ApJL, 435, L27

[35] Fernini, I., Burns, J. O., Bridle, A. H., & Perley, R. A. 1993, AJ, 105, 1690

[36] Fermi, E. 1949, Physical Review, 75, 1169

[37] Fermi, E. 1954, ApJ, 119, 1

[38] Gilbert, G. M., Riley, J. M., Hardcastle, M. J., Croston, J. H., Pooley, G. G., & Alexander, P. 2004, MNRAS, 351, 845

[39] Ghez, A. M., Becklin, E., Duchjne, G., Hornstein, S., Morris, M., Salim, S., & Tanner, A. 2003, Astronomische Nachrichten Supplement, 324, 527

[40] Gugliucci, N. E., Taylor, G. B., Peck, A. B., & Giroletti, M. 2005, ApJ, 622, 136

[41] Hardcastle, M. J., Alexander, P., Pooley, G. G., & Riley, J. M. 1998, MNRAS, 296, 445

[42] Harms, R. J., et al. 1994, ApJL, 435, L35

[43] Heavens, A. F., & Drury, L. O. 1988, MNRAS, 235, 997

[44] Holt, S. S., Neff, S. G., & Urry, C. M. 1992, American Institute of Physics Conference Series, 254

[45] Isobe, N., Makishima, K., Tashiro, M., & Hong, S. 2005, ApJ, 632, 781

[46] Ishwara-Chandra, C. H., Saikia, D. J., McCarthy, P. J., & van Breugel, W. J. M. 2001, MNRAS, 323, 460

[47] Jaffe, W. J., & Perola, G. C. 1973, A&A, 26, 423

[48] Jamrozy, M., Machalski, J., Mack, K.-H., & Klein, U. 2005, A&A, 433, 467

[49] Jeyakumar, S., & Saikia, D. J. 2000, MNRAS, 311, 397

[50] Kardashev, N. S. 1962, Soviet Astronomy, 6, 317

[51] Kameno, S., Inoue, M., Wajima, K., Sawada-Satoh, S., & Shen, Z.-Q. 2003,PASA, 20, 213

[52] Kameno, S., Sawada-Satoh, S., Inoue, M., Shen, Z.-Q., & Wajima, K. 2001, PASJ, 53, 169

[53] Kataoka, J., & Stawarz, Ł. 2005, ApJ, 622, 797

[54] Kawakatu, N., & Kino, M. 2006, MNRAS, 370, 1513

[55] Klein, U., Mack, K.-H., Gregorini, L., & Parma, P. 1995, A&A, 303, 427

[56] Kraus, J. D., Scheer, D. J., Dixon, R. S., Fitch, L. T., & Andrew, B. H., 1968, ApJ, 152, L35

[57] Kronberg, P. P., Wielebinski, R., & Graham, D. A. 1986, A&A, 169, 63

[58] Laing, R. A., Parma, P., de Ruiter, H. R., & Fanti, R. 1999, MNRAS, 306, 513

[59] Leahy, J. P., Muxlow, T. W. B., & Stephens, P. W. 1989, MNRAS, 239, 401

[60] Liu, R., Pooley, G., & Riley, J. M. 1992, MNRAS, 257, 545

[61] Lynden-Bell, D. 1969, Nature, 223, 690

[62] Maness, H. L., Taylor, G. B., Zavala, R. T., Peck, A. B., & Pollack, L. K. 2004, ApJ, 602, 123

[63] Mantovani, F., Saikia, D. J., Bondi, M., Junor, W., Salter, C. J., & Ricci, R. 2002, A&A, 389, L15

[64] Marecki, A., Barthel, P. D., Polatidis, A., & Owsianik, I. 2003, PASA, 20, 16

[65] Marr, J. M., Taylor, G. B., & Crawford, F., III 2001, ApJ, 550, 160

[66] Mack, K.-H., Klein, U., O'Dea, C. P., Willis, A. G., & Saripalli, L. 1998, A&A, 329, 431

[67] McNamara, B. R., Nulsen, P. E. J., Wise, M. W., Rafferty, D. A., Carilli, C., Sarazin, C. L., & Blanton, E. L. 2005, Nature, 433, 45

[68] Meisenheimer, K., Roser, H.-J., Hiltner, P. R., Yates, M. G., Longair, M. S., Chini, R., & Perley, R. A. 1989, A&A, 219, 63

[69] Miley, G. 1980, ARA&A, 18, 165

[70] Miyoshi, M., Moran, J., Herrnstein, J., Greenhill, L., Nakai, N., Diamond, P., & Inoue, M. 1995, Nature, 373, 127

[71] Moffet, A. T. 1975, Galaxies and the Universe, 211

[72] Morrison, P., Olbert, S., & Rossi, B. 1954, Physical Review , 94, 440

[73] Murgia, M. 2003, PASA, 20, 19

[74] Nagai, H., Inoue, M., Asada, K., Kameno, S., & Doi, A. 2006, ApJ, 648, 148

[75] O'Dea, C. P., Baum, S. A., & Stanghellini, C. 1991, ApJ, 380, 66

[76] O'Dea, C. P. 1998, PASP, 110, 493

[77] O'Dea, C. P., & Baum, S. A. 1997, AJ, 113, 148

[78] Owsianik, I., & Conway, J. E. 1998, A&A, 337, 69

[79] Owsianik, I., Conway, J. E., & Polatidis, A. G. 1998, A&A, 336, L37

[80] Owsianik, I., Conway, J. E., & Polatidis, A. G. 1999, NewAR, 43, 669

[81] Pacholczyk, A. G. 1970, Series of Books in Astronomy and Astrophysics, San Francisco: Freeman, 1970

[82] Parma, P., Murgia, M., Morganti, R., Capetti, A., de Ruiter, H. R., & Fanti, R. 1999, A&A, 344, 7

[83] Pearson, T. J., Shepherd, M. C., Taylor, G. B., & Myers, S. T. 1994, Bulletin of the American Astronomical Society, 26, 1318

[84] Pedlar, A., Ghataure, H. S., Davies, R. D., Harrison, B. A., Perley, R., Crane, P. C., & Unger, S. W. 1990, MNRAS, 246, 477

[85] Pérez-Torres, M.-A., & De Breuck, C. 2005, MNRAS, 363, L41

[86] Perucho, M., & Martí, J. M. 2003, PASA, 20, 94

[87] Phillips, R. B., & Mutel, R. L. 1980, ApJ, 236, 89

[88] Phillips, R. B., & Mutel, R. L. 1982, A&A, 106, 21

[89] Phillips, R. B., & Shaffer, D. B. 1983, ApJ, 271, 32

[90] Polatidis, A. G., & Conway, J. E. 2003, PASA, 20, 69

[91] Readhead, A. C. S., Taylor, G. B., Pearson, T. J., & Wilkinson, P. N. 1996, ApJ, 460, 634

[92] Saikia, D. J., Jeyakumar, S., Wiita, P. J., Sanghera, H. S., & Spencer, R. E. 1995, MNRAS, 276, 1215

[93] Saikia, D. J., Thomasson, P., Spencer, R. E., Mantovani, F., Salter, C. J., & Jeyakumar, S. 2002, A&A, 391, 149

[94] Sanghera, H. S., Saikia, D. J., Luedke, E., Spencer, R. E., Foulsham, P. A., Akujor, C. E., & Tzioumis, A. K. 1995, A&A, 295, 629

[95] Scheck, L., Aloy, M. A., Martí, J. M., Gómez, J. L., Muller, E. 2002, MNRAS, 331, 615

[96] Scheuer, P. A. G. 1984, Advances in Space Research, 4, 337

[97] Scheuer, P. A. G. 1974, MNRAS, 166, 513

[98] Schoenmakers, A. P., Mack, K.-H., Lara, L., Roettgering, H. J. A., de Bruyn, A. G., van der Laan, H., & Giovannini, G. 1998, A&A, 336, 455

[99] Shaffer, D. B., Kellermann, K. I., & Cornwell, T. J. 1999, ApJ, 515, 558

[100] Shakura, N. I., & Sunyaev, R. A. 1973, A&A, 24, 337

[101] Silver, C. S., Taylor, G. B., & Vermeulen, R. C. 1998, ApJ, 502, 229

[102] Smith, E. P., Heckman, T. M., Bothun, G. D., Romanishin, W., & Balick, B. 1986, ApJ, 306, 64

[103] Snellen, I. A. G., Schilizzi, R. T., Miley, G. K., de Bruyn, A. G., Bremer, M. N., Rottgering, H. J. A. 2000, MNRAS, 319, 445

[104] Snellen, I. A. G., Schilizzi, R. T., de Bruyn, A. G., Miley, G. K., Rengelink, R. B., Roettgering, H. J., & Bremer, M. N. 1998, A&A, 131, 435

[105] Stanghellini, C., Liu, X., Dallacasa, D., & Bondi, M. 2002, NewAR, 46, 287

[106] Stanghellini, C., O'Dea, C. P., Dallacasa, D., Baum, S. A., Fanti, R., & Fanti, C. 1998, A&AS, 131, 303

[107] Strauss, M. A., Yahil, A., Davis, M., Huchra, J. P., & Fisher, K. 1992, ApJ, 397, 395

[108] Sudou, H., Taniguchi, Y., Ohyama, Y., Kameno, S., Sawada-Satoh, S., Inoue, M., Kaburaki, O., & Sasao, T. 2000, PASJ, 52, 989

[109] Tanaka, Y., et al. 1995, Nature, 375, 659

[110] Taylor, G. B., Readhead, A. C. S., & Pearson, T. J. 1996, ApJ, 463, 95

[111] Taylor, G. B., Marr, J. M., Pearson, T. J., & Readhead, A. C. S. 2000, ApJ, 541, 112

[112] Taylor, G. B., Gugliucci, N. E., Fabian, A. C., Sanders, J. S., Gentile, G., & Allen, S. W. 2006, MNRAS, 368, 1500

[113] Taylor, G. B., Marr, J. M., Pearson, T. J., & Readhead, A. C. S. 2000, ApJ, 541, 112

[114] Tschager, W., Schilizzi, R., Röttgering, H., Snellen, I., Miley, G., & Perley, R. 2003, PASA, 20, 75

[115] Tribble, P. C. 1993, MNRAS, 261, 57

[116] Urry, C. M., & Padovani, P. 1995, PASP, 107, 803

[117] Walker, R. C., Dhawan, V., Romney, J. D., Kellermann, K. I., & Vermeulen, R. C. 2000, ApJ, 530, 233

[118] Wang, W.-H., Hong, X.-Y., & An, T. 2003, Chinese Journal of Astronomy and Astrophysics, 3, 505

[119] Wentzel, D. G. 1963, ApJ, 137, 135

[120] Wentzel, D. G. 1964, ApJ, 140, 1013

[121] Williams, A. G., & Gull, S. F. 1985, Nature, 313, 34

[122] Williams, A. G., & Gull, S. F. 1984, Nature, 310, 33

[123] Wilkinson, P. N., Polatidis, A. G., Readhead, A. C. S., Xu, W., & Pearson, T. J. 1994, ApJL, 432, L87

[124] Wilson, A. S., & Colbert, E. J. M. 1995, ApJ, 438, 62

[125] Winter, A. J. B., et al. 1980, MNRAS, 192, 931

Appendix A

Minimum-Energy Condition (Equipartition Condition)

In minimum total energy stored in synchrotron-emitting source, the magnetic field can be estimated in following way.

Assuming the power-law energy distribution ($N(E) = N_0 E^{-\gamma}$) of relativistic electrons in the source, total energy storing the electrons E_e is

$$\begin{aligned} E_e &= \int_{E_{min}}^{E_{max}} N(E) E dE \\ &= \int_{E_{min}}^{E_{max}} N_0 E^{1-\gamma} dE \\ &= N_0 \frac{E_{max}^{2-\gamma} - E_{min}^{2-\gamma}}{2-\gamma}. \end{aligned} \tag{A.1}$$

Performing above integration, we exclude the case of $\gamma = 2$.

On the other hand, the luminosity of the synchrotron radiation L is

$$\begin{aligned} L &= \int_{E_{min}}^{E_{max}} \frac{dE}{dt} N(E) dE \\ &= \int_{E_{min}}^{E_{max}} c_2 B^2 \sin\theta^2 E^2 N_0 E^{-\gamma} dE \\ &= N_0 c_2 B^2 \sin^2\theta \frac{E_{max}^{3-\gamma} - E_{min}^{3-\gamma}}{3-\gamma}, \end{aligned} \tag{A.2}$$

where $c_2 = 2e^4/3m^4c^7 = 2.37 \times 10^{-3}$ in CGS unit, B is the magnetic field strength, θ is a pitch angle between an electron and magnetic field. Dividing A.1 from A.2, we can eliminate N_0, and obtain

$$\frac{E_e}{L} = \frac{3-\gamma}{2-\gamma} \frac{1}{c_2 B^2 \sin^2\theta} \frac{E_{max}^{2-\gamma} - E_{min}^{2-\gamma}}{E_{max}^{3-\gamma} - E_{min}^{3-\gamma}} \tag{A.3}$$

An electron having the energy E emits the most radiation around its critical frequency, thus the relation of critical frequency and energy is given by $\nu = c_1 B \sin\theta E^2$, where $c_1 = 3e/4\pi m^3 c^5 = 6.27 \times 10^{18}$. Using this relation, equation A.3 is given by

$$\frac{E_e}{L} = \frac{3-\gamma}{2-\gamma} \frac{c_1^{1/2}}{c_2} (B\sin\theta)^{-3/2} \frac{\nu_{max}^{(2-\gamma)/2} - \nu_{min}^{(2-\gamma)/2}}{\nu_{max}^{(3-\gamma)/2} - \nu_{min}^{(3-\gamma)/2}}. \tag{A.4}$$

We can replace the energy spectral index γ by the emission spectral index using the relation $\gamma = 2\alpha+1$, then we have

$$\frac{E_e}{L} = \frac{2-2\alpha}{1-\alpha}\frac{c_1^{1/2}}{c_2}B^{-3/2}\frac{\nu_{max}^{(1-2\alpha)/2} - \nu_{min}^{(1-2\alpha)/2}}{\nu_{max}^{1-\alpha} - \nu_{min}^{1-\alpha}}. \tag{A.5}$$

In above equation, we replaced $B\sin\theta$ by B.

Here we define the total energy E_{total} within a source as

$$E_{total} = E_e + E_p + E_B, \tag{A.6}$$

where E_p is the total energy of proton (and/or other heavy particles) and E_B is the energy of magnetic field. We will suppose the proton energy is k times the electron energy. The parameter k depends on the acceleration mechanism. If the source is constituted purely positron-electron plasma, $k = 1$. In case of electron-proton plasma, k is up to 2000. According to measurements of the local galactic cosmic rays near the sun, k$\sim$100.

The energy of magnetic field within a radio source of radius r is

$$E_B = \frac{B^2}{8\pi} f \frac{4\pi r^3}{3}, \tag{A.7}$$

where f is the filling factor of the magnetic field and relativistic particles. Then we have

$$E_{total} = (1+k)\frac{2-2\alpha}{1-\alpha}\frac{c_1^{1/2}}{c_2}B^{-3/2}\frac{\nu_{max}^{(1-2\alpha)/2} - \nu_{min}^{(1-2\alpha)/2}}{\nu_{max}^{1-\alpha} - \nu_{min}^{1-\alpha}}L + \frac{B^2}{8\pi} f \frac{4\pi r^3}{3} \tag{A.8}$$

The total energy attains its minimum when the energy of magnetic field is equal to the total particle energy. This condition is called " minimum-energy condition " or " equipartition condition ". In this condition, the magnetic field strength is estimated to

$$B = \left(6\frac{1+k}{f}\frac{2-2\alpha}{1-\alpha}\frac{c_1^{1/2}}{c_2}\frac{\nu_{max}^{(1-2\alpha)/2} - \nu_{min}^{(1-2\alpha)/2}}{\nu_{max}^{1-\alpha} - \nu_{min}^{1-\alpha}}\frac{L}{r^3}\right)^{\frac{2}{7}}. \tag{A.9}$$

In case of $\alpha = 0.5$ ($\gamma = 2.0$), we have

$$B = \left(3\frac{1+k}{f}\frac{c_1^{1/2}}{c_2}\log\frac{\nu_{max}/\nu_{min}}{\nu_{max}^{1/2} - \nu_{min}^{1/2}}\right)^{2/7}. \tag{A.10}$$

The energy density u_{total} is

$$u_{total} = E_{total}\frac{3}{4\pi r^3}, \tag{A.11}$$

and equipartition pressure is estimated to

$$p = \frac{1}{3}u_{total}. \tag{A.12}$$

Appendix B

Synchrotron-Self Absorption ~ Relation of the Source Size and Peak Frequnecy ~

In this chapter, we will derive equation 1.8.

The transfer equation of synchrotron radiation with synchrotron-self absorption is

$$\frac{S_{\nu_m}}{\theta_x \theta_y} = \frac{\epsilon}{\kappa}(1 - \exp(-\tau)), \tag{B.1}$$

where S_{ν_m} is the source flux density, θ_x is major axis of the source, θ_y is minor axis of the source, ϵ is the emission coefficient, κ is the absorption coefficient, and τ is the optical depth. The emission and absorption coefficients are written by

$$\epsilon = \frac{1}{2} c_5(\gamma) N_0 (B \sin\theta)^{\frac{\gamma+1}{2}} \left(\frac{\nu}{2c_1}\right)^{\frac{1-\gamma}{2}} \left(1 + \frac{\gamma+1}{\gamma+2/3}\right) \tag{B.2}$$

$$\kappa = c_6(\gamma) N_0 (B \sin\theta)^{\frac{\gamma+2}{2}} \left(\frac{\nu}{2c_1}\right)^{-\frac{\gamma+4}{2}} \left(1 + \frac{\gamma+2}{\gamma+10/3}\right), \tag{B.3}$$

where γ and N_0 are power-law index and electron density, respectively, which are defined by $N(E) = N_0 E^{-\gamma}$. The function c_5 and c_6 are

$$c_5(\gamma) = \frac{1}{4} c_3 \left(\frac{\gamma+7/3}{\gamma+1}\right) \Gamma\left(\frac{3\gamma-1}{12}\right) \Gamma\left(\frac{3\gamma+7}{12}\right) \tag{B.4}$$

$$c_6(\gamma) = \frac{1}{32} \left(\frac{c}{c_1}\right)^2 c_3 \left(\gamma + \frac{10}{3}\right) \Gamma\left(\frac{3\gamma+2}{12}\right) \Gamma\left(\frac{3\gamma+10}{12}\right), \tag{B.5}$$

where c is speed of light and $c_3 = \sqrt{3}e^3/4\pi mc^2 = 1.87 \times 10^{-23}$ in CGS unit.

Equation B.1 attains its peak where $\tau(\nu) \sim 1$. We define ν_m at where $\tau(\nu_m) = 1$. Then equation B.1 is

$$\begin{aligned} \frac{S_{\nu_m}}{\theta_x \theta_y} &= \frac{1}{2}\frac{c_5}{c_6} (B \sin\theta)^{-\frac{1}{2}} \left(\frac{\nu}{2c_1}\right)^{\frac{5}{2}} \frac{1 + (\gamma+1)/(\gamma+7/3)}{1 + (\gamma+2)/(\gamma+10/3)} (1 - \exp(-1)) \\ &\propto B^{-\frac{1}{2}} \nu^{\frac{5}{2}}. \end{aligned} \tag{B.6}$$

Assuming $\theta_x = \theta_y = \theta$, above equation is given by

$$\theta \propto S_{\nu_m}^{\frac{1}{2}} B^{\frac{1}{4}} \nu_m^{-\frac{5}{4}}. \tag{B.7}$$

Equation B.7 can be applicable to the frame rest to the source. Now we rewrite above equation in observer frame. Flux density S_{ν_m} and frequency ν_m have the relation

$$S_{\nu_m}^{rest} = (1+z)^3 S^{obs} \tag{B.8}$$

$$\nu^{rest} = (1+z)\nu^{obs}, \tag{B.9}$$

where the subscript "rest" and "obs" means rest frame and observer frame, respectively. Applying above equations to equation B.7, we have

$$\theta \propto (1+z)^{\frac{1}{4}} (S_{\nu_m}^{obs})^{\frac{1}{2}} B^{\frac{1}{4}} (\nu_m^{obs})^{-\frac{5}{4}}. \tag{B.10}$$

Appendix C

Koromogorov-Smirnov Test (KS-Test)

The KS-test is used for comparing two sets of measurement of the same quantity under the null hypothesis that the two sets of measurements come from the same distribution. The KS-test statistics D is defined as the largest difference between the two cumulative distributions ($S_{N_1}(x)$ and $S_{N_2}(x)$),

$$D = max|S_{N_1}(x) - S_{N_2}(x)|. \tag{C.1}$$

The probability that D is larger than observed value is given by

$$Q = 2\sum_{j=1}^{\infty}(-1)^{j-1}\exp -2j^2\lambda^2, \tag{C.2}$$

where

$$\lambda = \sqrt{N_1N_2/(N_1+N_2)}D. \tag{C.3}$$